Title

25th Anniversary Article: Semiconductor Nanowires – Synthesis, Characterization, and Applications

Journal

Advanced Materials, 26(14)

ISSN

0935-9648

Authors

Dasgupta, Neil P
Sun, Jianwei
Liu, Chong
et al.

Publication Date

2014-04-01

DOI

10.1002/adma.201305929

Review Article

Semiconductor Nanowires: Synthesis, Characterization, and Applications

*Neil P. Dasgupta, Jianwei Sun, Chong Liu, Sarah Brittman, Sean C. Andrews, Jongwoo Lim, Hanwei Gao, Ruoxue Yan, and Peidong Yang**

Dr. N. P. Dasgupta[1], Dr. J. Sun[1,2], C. Liu[1,2], S. Brittman[1,2], Dr. S. C. Andrews[1,2], J. Lim[1,2], Dr. H. Gao[1,2], Dr. R. Yan[1,2], Prof. P. Yang[1,2,3,4]

[1]Department of Chemistry
University of California, Berkeley
Berkeley, CA 94720, USA
email:p_yang@berkeley.edu

[2]Materials Science Division
Lawrence Berkeley National Laboratory
Berkeley, CA 94720, USA

[3]Department of Materials Science and Engineering
University of California, Berkeley
Berkeley, CA 94720, USA

[4]Kavli Energy Nanosciences Institute
Berkeley, CA 94720, USA

Current Address:

Prof. N. P. Dasgupta
Department of Mechanical Engineering
University of Michigan
Ann Arbor, MI 48109, USA

Prof. H. Gao
Department of Physics
Florida State University
Tallahassee, FL 32306

Prof. R. Yan
Department of Chemical & Environmental Engineering
University of California, Riverside
Riverside, CA 92521

Keywords: Nanostructure, Nanowires, Synthesis, Electronics, Photonics, Energy, Thermoelectric, Photovoltaic, Photoelectrochemistry, Energy Storage, NEMS, Bio-Nano Interface

Table of Contents

Abstract

Semiconductor nanowires (NWs) have been studied extensively for over two decades for their novel electronic, photonic, thermal, electrochemical and mechanical properties. This comprehensive review article summarizes major advances in the synthesis, characterization, and application of these materials in the past decade. Developments in the understanding of the fundamental principles of "bottom-up" growth mechanisms are presented, with an emphasis on rational control of the morphology, stoichiometry, and crystal structure of the materials. This is followed by a discussion of the application of nanowires in i) electronic, ii) sensor, iii) photonic, iv) thermoelectric, v) photovoltaic, vi) photoelectrochemical, vii) battery, viii) mechanical, and ix) biological applications. Throughout the discussion, a detailed explanation of the unique properties associated with the one-dimensional nanowire geometry will be presented, and the benefits of these properties for the various applications will be highlighted. We conclude with a brief perspective on future research directions, and remaining barriers which must be overcome for the successful commercial application of these technologies.

1. Introduction

One dimensional nanostructures, such as wires, tubes, belts, and rods, have been extensively studied for the past two decades due to their interesting and unique electronic, optical, thermal, mechanical and magnetic properties. 10 years ago, our group co-authored a review article in *Advanced Materials* on the synthesis, characterization, and applications of these materials[1]. In the early stage of this research field, novel synthetic routes and fundamental characterization were heavily emphasized due to the emergence of this new field of nanoscience. The ability to fabricate high-quality single-crystalline materials with control of diameter, length, composition, and phase enabled breakthroughs in the incorporation of these materials into useful devices. Early applications emphasized electronic and optical devices, which provided further insight and stimulus to gain a deeper understanding of the basic material properties of these structures.

In the past decade, a tremendous amount of progress has been made in the field of one-dimensional nanostructures. In this comprehensive review, we focus on the development of semiconductor nanowires in electronic, photonic, mechanical, biological, and energy-conversion applications in the past 10 years. Among the various classes of one-dimensional nanostructures, semiconductor nanowires possess several unique characteristics. Their ability to be integrated into electronic devices, novel sub-wavelength optical phenomena, their large tolerance for mechanical deformations, their ability to interface with other microscopic and nanoscopic systems in nature, the decoupling of length scales associated different physical phenomena in the radial and axial directions, and their high surface-to-volume ratio, have led to an explosion of applications utilizing these structures.

We begin by reviewing advances in synthetic routes and the fundamental understanding of growth mechanisms for semiconductor nanowires in the past decade. In particular, bottom-up synthetic routes using both gas-phase and solution-phase chemistry have enabled a variety of new material systems and morphologies to be obtained with improved control of the crystalline and chemical properties. We subsequently discuss semiconductor nanowires for electronic, sensing, and photonic applications, and their potential integration into more complex electronic and optoelectronic systems. This is followed by a detailed discussion of various energy conversion and storage applications, which has become an increasingly important topic over the past decade due to rising concerns of non-renewable energy resources, environmental degradation, and socio-political conflicts involving the energy sector. Next, a discussion of mechanical properties and applications is presented, and finally, biological applications at the nanowire-cell interface are discussed.

This 10 year update from our previous *Advanced Materials* Review reflects the dramatic increase in nanowire research and publications over the past decade. The transition from initial proof-of-concept experiments into the development of integrated nanosystems reflects a pathway towards commercial applications. The conclusion of the article presents a perspective on the implications of these results for future research directions, and the remaining barriers for commercialization and adaptation of these technologies to benefit human society.

2. Synthesis of Nanowires

Over the past decade, the general strategies for achieving one-dimensional nanowire growth outlined in our 2003 review article have not changed substantially. A tremendous amount of research effort has been devoted to understanding nanowire growth at the atomic level and to precisely controlling the nanowire dimension, crystal structure, composition, growth pattern, and structural/compositional complexity. In this section, we review important new techniques and concepts that emerged during the past 10 years with a focus on "bottom-up" synthesis of semiconductor nanowires.

2.1 Metal-Nanoparticle-Mediated Methods

2.1.1 Synthesis in gas phase: vapor-liquid-solid (VLS) and vapor-solid-solid (VSS) methods

The VLS crystal growth method is undoubtedly the most widely adopted approach to grow semiconductor nanowires because of its great flexibility. However, many fundamental aspects of VLS growth have remained unclear. During the past decade, various *in situ* techniques, particularly *in situ* electron microscopy, have been employed to quantitatively probe the fundamental VLS processes during nanowire growth. As a result, many new concepts have been developed, which have considerably enriched our understanding of VLS growth. In parallel with the *in situ* studies, *ex situ* experiments have enabled VLS growth of semiconductor nanowires with improved control. Importantly, a new VSS growth mode has been established, which opens exciting new avenues for nanowire growth.

VLS growth kinetics: VLS nanowire growth involves three distinct stages: alloying, nucleation and growth. Because the kinetics are very rapid under conventional growth conditions, it is difficult to probe the events at different stages of VLS growth. Recently, Ross, Stach and coworkers systematically investigated the growth kinetics of a classic Au/Si VLS system based on real time observation of growth experiments within an ultrahigh-vacuum transmission electron microscope (UHV-TEM) equipped with a heated specimen holder and a capillary precursor delivery system.[2] The pressure of the Si precursor, disilane, was on the order of μtorr, lower than that of conventional growth. Therefore, the kinetics were intentionally slowed down for easier real-time imaging. During the initial alloying stage, a thin AuSi liquid shell was observed around the solid Au core almost immediately after the introduction of the Si precursor. The volume of the solid core decreased in a roughly linear fashion until its diameter reached ~15 nm, below which the core shrinkage was very rapid, indicating that the Au(*s*)/AuSi(*l*) two phase system became unstable at small Au volumes.[2a]

When the alloying process was complete, continued supply of the Si precursor eventually resulted in nucleation. It was observed that the Si nucleus suddenly appeared at the edge of the liquid droplet and rapidly grew for a few seconds, followed by growth at a significantly reduced rate.[2b] These results illustrated two concepts: (i) the nucleation is heterogeneous, consistent with the surface crystallization observed using X-ray measurements.[3] (ii) the heterogeneous nucleation requires a higher supersaturation level than the Si precipitation to the existing nucleus.

Once the nucleation event begins, the excess Si in the liquid droplet rapidly precipitates, resulting in an initial jump in nucleus size and a decrease in the supersaturation level. When the supersaturation reaches the lower level required for the Si precipitation to the existing nucleus, a slower growth process occurs with a rate determined by the Si flux from the droplet.

At the steady-state nanowire growth stage, real-time TEM observations showed that the AuSi(*l*)/Si (111) interface advanced by a 0.3 nm step, corresponding to the distance between two adjacent Si(111) planes.[2c] Therefore, the VLS nanowire growth proceeds in a layer-by-layer fashion. A long incubation period (>10 s) was observed between two layer-growth events, indicating that the local Si concentration fluctuates at the liquid/solid interface. However, the addition of one Si(111) layer was too fast to be measured even at a low Si_2H_6 pressure of 2×10^{-6} Torr. Traditionally, it was believed that layer nucleation would occur at the triple junction where the flat nanowire growth front and the nanowire side facets meet. Accordingly, semiconductors would deposit on the growth front by step flow starting from the triple junction. Recently, *in situ* TEM studies of the nanowire growth interface have shown that the major atomically flat nanowire growth front and the nanowire side facets do not meet at the triple junction, but are instead connected by other facets.[4] During the layer-by-layer nanowire growth, the connecting facets dynamically oscillate in size due to growth and dissolution of semiconductor material. Interestingly, for the self-catalyzed VLS growth of sapphire (α-Al_2O_3) nanowires, the oscillation of the connecting facets provides an oxygen transport channel by incorporation from the triple junction, which is different from the typical VLS mass transport mediated through the liquid phase.[4c]

Foreign-metal-catalyst loss channels: In the conventional VLS growth model, the foreign metal catalyst in the nano-droplet is considered to be stable during growth. Therefore, the diameter and length of the nanowires can be independently controlled by the size of the droplet and the growth time. However, metal loss channels exist during nanowire growth, which was revealed in the case of Au-catalyzed Si nanowire growth under well-controlled growth conditions in a UHV electron microscope.[5] First, Ostwald ripening of the AuSi catalyst droplets on the nanowire tips was observed *in situ* in a UHV-TEM, indicating that Au can diffuse from one catalyst droplet to another. Second, selected-area electron diffraction measurements in a low-energy electron microscope (LEEM) confirmed that both the Si nanowire surface and the bare Si substrate surface (not covered by nanowires) were covered by one monolayer of Au atoms. These results conclusively suggest a considerable surface-mediated loss of Au atoms from the AuSi droplets. It was also found that the Au migration is sensitive to the nanowire growth environment. For example, low-level oxygen that was intentionally introduced to the UHV-TEM could effectively suppress the Au migration because of the formation of a partly oxidized nanowire surface.[6]

Another loss channel that has long been assumed is the incorporation of foreign metal elements into the nanowire lattice. For the classic Au/Si VLS system, this is a serious concern because Au is detrimental to the electronic properties of the Si nanowires. Detection of trace amounts of Au atoms in Si nanowires was achieved only recently by using high-angle annular dark-field scanning transmission electron microscopy (HAADF-STEM),[7] directly confirming the lattice-incorporation loss channel. In a separate study of Al-catalyzed Si nanowire growth, atomic-level mapping of individual Si nanowires using highly focused laser-assisted atom-probe tomography showed that the concentration of Al impurity atoms in the Si nanowires exceeded the equilibrium solid solubility by orders of magnitude.[8] Based on these results, it seems reasonable to believe that loss of foreign metal catalyst to the nanowire lattice may be general for any foreign-metal-nanoparticle-mediated nanowire growth.

Control of crystal structure: Since the chemical and physical properties of nanowires can be greatly influenced by their crystal structure, it is highly desirable to achieve precise control of crystallographic properties such as growth direction, phase, and defect levels. Various rational approaches have been demonstrated to achieve growth of nanowires with controlled crystallographic growth direction. Based on thermodynamic arguments, nanowires should grow along the direction that minimizes the total free energy of the system. For the VLS growth mechanism, the total free energy includes both the solid/liquid interfacial energy and the nanowire surface energy, which are dependent on the nanowire diameter and surface properties. For example, in the study of Au-catalyzed Si nanowires, it was found that the smallest-diameter (< ~10 nm) nanowires almost exclusively grow along the <110> direction, and larger-diameter wires can grow along either the <111> or the <112> direction depending on the growth conditions, such as temperature and pressure.[9] However, the origin of the transition from the <111> to the <112> growth direction remained unclear for a long time. Recently, *in-situ* spectroscopic measurements of Au-catalyzed Si nanowires grown in a UHV chamber equipped with a FT-IR spectrometer strongly suggested that covalently bonded surface hydrogen atoms, which are generated during the catalytic decomposition of the disilane precursor, are responsible for the commonly observed growth direction transition.[10]

By using an iterative growth approach, Lieber and coworkers reported the rational growth of two-dimensional zigzag semiconductor nanowires with controlled lengths of the straight arms and positions of the joints (**Figure 1**a-d).[11] For the Au-catalyzed zigzag Si nanowires, crystallographic analysis showed that the arms coherently grow along the normally observed

<112> direction, but the joints grow along the <110> direction, which is thermodynamically unfavorable in the diameter regime investigated. The joint formation is a result of purging and re-introducing the silane precursor. During the purge step, growth of the straight arm will cease when the supersaturation level of the AuSi droplets is significantly reduced. Although the previous supersaturation can be re-established after re-introduction of the Si precursor, the growth interruption can kinetically result in a preferential heterogeneous nucleation at the {110} edges of the three-phase boundary, and a subsequent growth along the unusual <110> direction. However, this kinetic growth mode is unsustainable. When the joint with a quasi-triangular structure is completed, the growth direction tends to change back to <112>, which is thermodynamically favorable at the synthetic conditions.

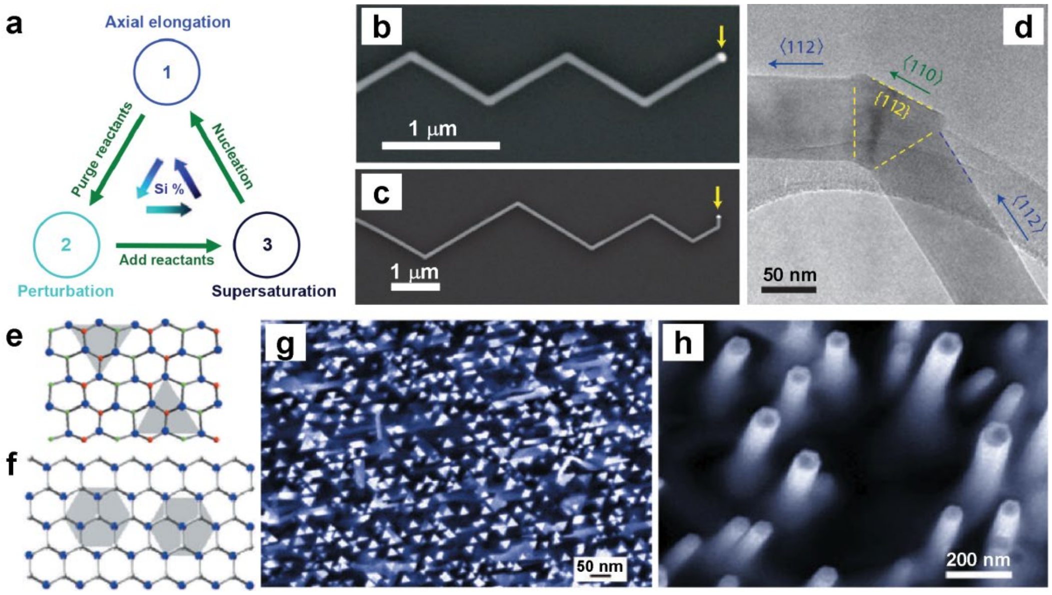

Figure 1. Rational control of nanowire growth direction. a) Cycle used for control of kinked nanowire morphology, indicating the use of purging and adding reactants to control the Si concentration in the catalyst particle (shown by the color gradient in the inner blue arrows). b) SEM image of a kinked nanowire with equal length segments. c) SEM image of a kinked nanowire with decreasing length segments. d) TEM image of a kinked nanowire, showing the crystallographic direction of each segment. Reproduced with permission.[11] Copyright 2009, Nature Publishing Group. e) Schematic of the γ-LiAlO$_2$ (100) plane and the f) MgO (111) plane, with the corresponding epitaxial match to GaN crystal planes shown in the shaded grey boxes. g) Top-view SEM image of GaN nanowires grown on (100) γ-LiAlO$_2$ substrates with triangular

cross sections and h) grown on (111) MgO substrates with hexagonal cross sections, illustrating rational control of nanowire growth direction by substrate control. Reproduced with permission.[12] Copyright 2004, Nature Publishing Group.

For the VLS growth of GaN nanowires, Yang and coworkers demonstrated deterministic control of the crystallographic nanowire growth direction based on the heteroepitaxial relationship between the single-crystal substrates and GaN (Figure 1e-h).[12] In this approach, a suitable substrate should have symmetry and lattice constants that closely match those of GaN. For example, the oxygen sublattice in the γ-$LiAlO_2$ (100) plane has two-fold symmetry, which matches the two-fold symmetry of the wurtzite GaN (100) plane. The lattice constants a = 5.17 Å and c = 6.28 Å of γ-$LiAlO_2$ match the lattice constants c = 5.19 Å and two times a = 3.19 Å of GaN. When a γ-$LiAlO_2$(100) substrate was used, wurtzite GaN nanowires preferentially grow along the $[1\bar{1}0]$ direction. In contrast, the MgO (111) plane has three-fold symmetry, which matches the three-fold symmetry of the wurtzite GaN (001) plane. The interatomic separation of the atoms in the MgO (111) plane is 2.98 Å, which matches the lattice constant a = 3.19 Å of GaN. When the MgO(111) substrate was used, wurtzite GaN nanowires preferentially grow along the [001] direction.

III-V nanowires often exhibit randomly distributed zinc-blende/wurtzite polytypism, twin defects, and stacking faults. This represents a challenge to grow phase pure nanowires with minimized or controlled defect levels. In the Au-catalyzed growth of InAs nanowires, the nanowire diameter and growth temperature were identified as two important parameters to control the phase purity and defect density.[13] At a relatively high temperature of 460 °C, a crystal phase transition from pure wurtzite to randomly mixed wurtzite/zinc blende to pure zinc blende was observed with increasing diameter in the range of 24-110 nm. Because thinner wires have larger surface-to-volume ratio, a possible explanation of the formation of wurtzite phase in thin nanowires is that the side walls of the wurtzite wires have lower surface energy than the zinc-blende wires. Although the largest-diameter (110 nm) wires adopted a pure zinc-blende crystal structure, a periodic twin-plane superlattice along the <111>B growth direction was observed. For the medium-diameter wires, the defect density was high, but could be significantly reduced at a lower growth temperature of 420 °C. This temperature-dependent suppression of defect density has also been reported for VLS-grown GaAs nanowires.[14]

In another study of Au-catalyzed InP nanowire growth, an impurity dopant was used to control the crystal phase and defects.[15] Three growth modes were established depending on the pressure of diethylzinc, which is the precursor of the Zn dopant. At low diethylzinc pressure ($<4.6 \times 10^{-5}$ mbar), the wurtzite growth mode is dominant. A transition to the zinc-blende growth mode was achieved at higher diethylzinc pressure, because the zinc dopant has been shown to decrease the activation barrier for the two-dimensional nucleation of zinc-blende InP at the liquid/solid interface. Within the zinc-blende growth regime, when the diethylzinc pressure further exceeded a threshold value (4.6×10^{-4} mbar), a twinning superlattice growth mode was observed.

The above-described approaches to grow phase pure III-V nanowires have their own limitations because either the nanowire diameter window is too restricted or the dopant can significantly alter the nanowire properties. Recently, Joyce and coworkers demonstrated that phase pure zinc-blende and wurtzite InAs nanowires in a wide diameter range could be synthesized by simply adjusting the growth temperature and III/V ratio.[16] As a general trend, syntheses conducted at low and high temperature and III/VI ratio can afford zinc-blende and wurtzite wires, respectively. This success in achieving phase purity was attributed to changes in nanowire surface energy at different growth conditions.

Control of position and orientation: Precise control of nanowire position and orientation relative to the substrate surface is very important for device fabrication. This is generally achieved by using various lithographic techniques[17] or a template-directed method[18] to produce well defined patterns of catalyst nanoparticles on epitaxial substrates. Conventional VLS growth typically affords vertical nanowire arrays on substrates with the lowest-free-energy surface, such as the (111) surface of group IV semiconductors and the (111)B surface of III-V semiconductors. However, VLS growth of horizontal nanowires should also be possible when substrates with other surfaces are used. For example, Au-catalyzed growth of horizontally aligned GaAs nanowires on GaAs(100) substrates was reported.[19] The wires grew along the <110> direction and exhibited the homoepitaxial relationship with the substrate. The nanowire self-alignment is likely driven by minimization of interfacial energy and strain along a specific lattice direction of the substrate.

Recently, Joselevich and coworkers demonstrated that Ni-catalyzed VLS growth of millimeter-long horizontal GaN nanowires could be achieved on different planes of sapphire substrates that have a heteroepitaxial relationship with the nanowires.[20] Other than the commonly reported epitaxial growth methods, a graphoepitaxial growth of nanowires with deterministic cross sections along surface nanosteps and nanogrooves was also demonstrated, which is driven by maximization of the interfacial area between the substrate surface features and the nanowires.

For substrates that do not have an epitaxial relationship with the nanowires, nanochannels containing catalyst nanoparticles can be used as a template to physically guide the nanowire growth orientation. For example, electrically-contacted horizontal Si nanowire arrays were fabricated on Si substrates with surface oxide layer by using parallel nanochannels with an Au nanoparticle in the middle of each channel.[21]

Lithographic techniques can independently control both the size and the pitch of catalyst nanoparticles, enabling a quantitative study of how the growth behavior of vertical nanowire arrays can be influenced by these parameters. In the VLS growth of ordered vertical GaP nanowire arrays catalyzed by lithographically patterned Au nanoparticles, Bakkers and coworkers discovered a previously unknown nanowire growth regime.[22] For this VLS system, the precursor molecules that decompose both directly on the catalyst nanoparticle surface and within one *surface-diffusion length* of the nanowire growth front will contribute to the nanowire growth. Importantly, part of the surface-adsorbed precursor species on one nanowire surface can desorb and diffuse in the gas phase to neighboring nanowires within one *gas-phase diffusion length* to further promote their growth. Experiments conducted at 500 °C showed that, when the pitch of the catalyst nanoparticles is large enough (>3 μm), the nanowire growth is isolated event and the growth rate is low and independent of wire diameter. Therefore, this growth regime is called an *independent regime*. Surprisingly, the wire growth rate increases at smaller pitches, in contrary to the known VLS growth models. This growth rate enhancement can be attributed to the fact that wires in close proximity can interact with each other through gas-phase diffusion of precursor species. As such, this new growth regime is called a *synergetic regime*. However, the growth rate does not increase monotonically within this regime. In the pitch range of 3-0.7 μm, the wire growth rate increases with decreasing pitch for all wire diameters investigated and the growth rate is higher for larger-diameter wires at fixed pitches. These effects are due to the increased catalyst surface fraction, which results in an increased local concentration of precursor species and their enhanced diffusion. In contrast, for smaller pitches <0.7 μm, the wire growth rate starts to decrease with decreasing pitch (but is still higher than in the independent regime) and the growth rate is higher for smaller-diameter wires. These effects are caused by limited supply of precursor species at a high nanowire density. Thus, this regime is called a *materials competition regime*.

Nanowires with complex structures: The great flexibility of VLS methods has been further demonstrated by rational synthesis of nanowires with complex structures. For example, hierarchical branched nanowires with homo- and/or hetero-junctions can be grown by depositing catalyst nanoparticles on the backbone of the nanowires grown in the previous VLS step.[23] Additionally, controlled axial modulation of composition can be readily achieved by switching the semiconductor or impurity precursors during nanowire growth.[24]

For the axial heterojunction nanowires, formation of a compositionally abrupt junction is critical to achieve optimal device performance. However, a reservoir effect caused by the solubility of the first semiconductor in the catalyst droplets will generally result in diffuse junctions. This is particularly problematic for Au-catalyzed VLS growth of Si/Ge heterojunction nanowires because of the substantial solubility of both Si and Ge in Au. To alleviate this problem, a rational approach is to lower the solubility of the first semiconductor in the catalyst droplets. This approach has been recently demonstrated by engineering the catalyst composition through *in situ* catalyst alloying.[25] It was shown that the eutectic solubility of Si and Ge in Au_xGa_{1-x} alloy can be systematically decreased relative to that of Si and Ge in Au. As a result, the width of the diffuse transition region can be significantly reduced down to ~10 nm. However, it is still challenging to achieve an atomically abrupt junction by the VLS methods.

Continuous nanowire production: The traditional VLS nanowire growth process is based on batch production because the catalyst nanoparticles need to be deposited on supporting substrates. However, for industrial-scale applications of nanowire-based devices, the batch production of nanowires may not be efficient. Very recently, Samuelson and coworkers demonstrated a new continuous gas-phase production mode to grow Au-catalyzed GaAs nanowires on a large scale.[26] In this method, spherical Au nanoparticles with uniform sizes are produced in the gas phase by thermal annealing of size-sorted Au aerosol particles. Nanowire growth is initiated by mixing the Au nanoparticles with the gaseous semiconductor precursors in a tube furnace heated to the growth temperature. The time for nanowire growth is determined by the carrier gas flow rate. Interestingly, it was observed that the nanowire growth rate of this continuous growth can be at least one-order-of-magnitude higher than that of the traditional substrate-based growth.

Transition between VLS and VSS growth mode: Bulk equilibrium phase diagrams provide a useful first-order picture to understand the VLS nanowire growth. In general, the growth temperature should exceed the eutectic temperature to keep the catalyst nanoparticles in a liquid phase. However, many experiments conducted below the eutectic temperature still afforded nanowires. Thus, the physical state of the catalyst nanoparticles was under debate.

In the *in situ* growth of Au-catalyzed Ge nanowires conducted in a UHV-TEM, Ross and coworkers observed strong evidence that the VLS nanowire growth mode can be maintained when the temperature is decreased to a value that is ~100 °C lower than the bulk Au-Ge eutectic temperature of 361 °C.[27] This significant drop of VLS growth temperature cannot be understood by nanoscale size effects. It was proposed that the Ge supersaturation required for the nanowire growth can kinetically inhibit nucleation of solid Au in a certain temperature range below the eutectic temperature. However, when the temperature is sufficiently low (255 °C in this case), the AuGe droplets with smoothly curved surfaces eventually solidify rapidly to become faceted catalyst nanoparticles and the wires continue to grow in a VSS growth mode, which was previously proposed by others.[28] Interestingly, when the temperature is increased back to the original VLS growth temperature below the eutectic temperature, the VSS growth mode can still be maintained until the temperature reaches a value that is well above the eutectic temperature. Therefore, both VLS and VSS growth mode can operate at the same temperature, depending on the thermal history (**Figure 2**a-d).

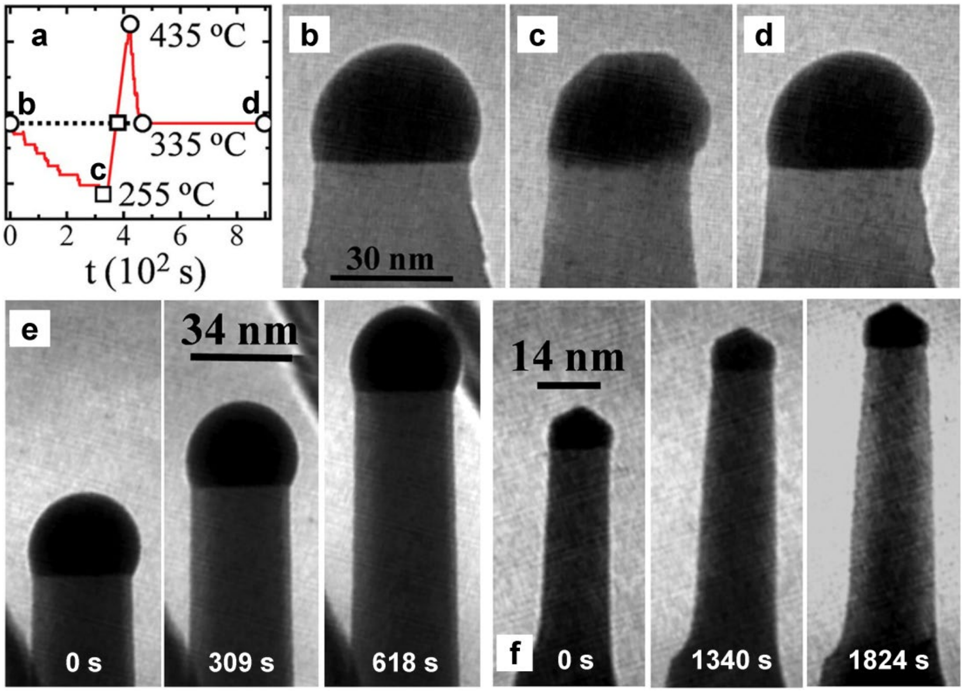

Figure 2. Au nanoparticle-mediated growth of Ge nanowires below the eutectic temperature. a) The growth temperature profile and the catalyst state. The nanowire growth was initiated by first heating to above the eutectic temperature (361°C) and then cooling to 335°C (point b), at which point the catalyst still remained in the liquid state represented by the open circle. When the temperature was further reduced to 255°C (point c) the liquid catalyst particle transformed into the solid state represented by the open square. Upon heating, the catalyst did not transform back into a liquid state until 435°C, after which point the temperature was returned to 335°C (point d). During this process, the Ge_2H_6 pressure was kept constant at 1.6×10^{-6} Torr. The bright-field TEM images acquired at point b, c, and d, are shown in (b)-(d), respectively. e) A series of TEM images during the VLS growth of a single Ge nanowire at 340°C and 4.6×10^{-6} Torr Ge_2H_6, showing a growth rate of 9.9×10^{-2} nm/s. f) A series of TEM images during the VSS growth of a single Ge nanowire at the same temperature and Ge_2H_6 pressure as in (e), showing a growth rate of 1.3×10^{-2} nm/s. Reproduced with permission.[27] Copyright 2007, American Association for the Advancement of Science.

Fundamentals and advantages of VSS growth mode: In the bulk metal-semiconductor phase diagrams, stable compounds often exist. During the alloying stage, the solid state reaction between the metal and the semiconductor can yield crystalline faceted compound nanoparticles that serve as the catalyst nanoparticles.[29] This is quite different from the VLS alloying process. However, the nucleation of VSS-grown nanowires was also found to be heterogeneous, similar to the case of VLS growth.[30] For solid catalyst nanoparticles with various facets, the initial nucleation site remains unclear so far. During the nanowire growth stage, ledge (or step) nucleation and lateral flow at the catalyst/nanowire interface was observed in different VSS systems.[2c, 29] It was found that the ledge nucleation always occurs at the nanowire edges. The nanowire growth by ledge nucleation and flow should also be expected for the VLS growth mode, although it has not been directly observed due to its much faster kinetics. Real-time TEM studies of the VSS and VLS nanowire growth modes with the same synthetic conditions showed that the wire growth rate achieved in the VSS mode is about one-order-of-magnitude lower than that in the VLS mode (Figure 2e-f).[27] This is likely due to the low solubility and/or diffusivity of the semiconductor elements in the solid catalyst nanoparticles.

Compared to VLS, the VSS growth mode exhibits some advantages. First, for metals that form very high eutectic temperatures with the semiconductors, the VSS nanowire growth temperature can be substantially lower than the eutectic temperature, enabling fabrication of nanowire-based devices compatible with standard industrial processes. For example, Cu_3Si-mediated VSS growth of Si nanowires can be achieved at temperatures as low as 400 °C, which is CMOS-compatible.[31] Second, the solubility of the semiconductor in the solid catalyst nanoparticle can be significantly reduced, enabling growth of axial heterojunction nanowires with abrupt interface. For example, Si/Ge heterojunction nanowires with compositionally abrupt interface have been synthesized via the VSS growth mode.[2c, 30]

2.1.2 Synthesis in solution phase: solution-liquid-solid (SLS), supercritical fluid-liquid-solid (SFLS) and supercritical fluid-solid-solid (SFSS) methods

The SLS approach, analogous to the VLS approach, is widely adopted to grow colloidal semiconductor nanowires. It offers several advantages over VLS growth, including systematic control of nanowire mean diameters down to the quantum-confinement regime, control of surface passivation, nanowire solubility, and large-scale production. Some synthetic concepts developed in the VLS growth can be readily adopted for the SLS nanowire growth. For example, the SLS syntheses have afforded homo- and hetero-branched nanowires and nanowires having axial heterojunctions.[32] However, it seems challenging for the SLS method to achieve the degree of flexible control over nanowire crystal structure and growth orientation discussed in the VLS section.

The SFLS nanowire growth is conducted in organic solvents under supercritical conditions. As such, the growth temperature can be much higher than that of the SLS growth, enabling use of transition metal nanoparticles as the seeds for nanowire growth and discovery of a new SFSS growth mode. Here we highlight the most important achievements of SLS growth and the evidence of SFSS growth.

Diameter-controlled quantum wires. The solution-based SLS nanowire growth temperatures (<~350 °C) are generally much lower than the VLS growth temperatures. In addition, the surface of the SLS grown nanowires is typically protected by surfactant molecules during nanowire growth. Therefore, the radial growth of colloidal nanowires can be effectively suppressed. As a result, control of the nanowire mean diameter and the diameter distribution can be easily achieved by using nearly monodisperse metal catalyst nanoparticles, such as Bi and In nanoparticles. Because colloidal metal nanoparticles having small diameters down to a few nanometers are accessible,[33] SLS growth of diameter-controlled quantum wires with narrow diameter distributions has been achieved, enabling a systematic study of the shape-dependent quantum confinement effects.[34]

Surfactant-free SLS approach: Traditional SLS growth of colloidal nanowires typically requires the use of organic surfactants or surface capping ligands to stabilize both the catalyst nanoparticles and the nanowires. However, covalently bound surface organic molecules are undesired for certain applications such as photo-assisted surface reactions in aqueous solutions, because the organic surface layer can prevent efficient charge transfer between the nanowires and the solution species. To completely avoid this problem, a surfactant-free SLS approach was recently demonstrated for the growth of colloidal GaP nanowires.[35] This new SLS synthesis only uses three chemicals: triethylgallium and tris(trimethylsilyl)phosphine as the semiconductor precursors and squalane (a branched alkane with high boiling point) as the solvent. The nanowires grow via a self-seeded SLS process: triethylgallium first thermally decomposes *in situ* to generate Ga nanodroplets, which then subsequently catalyze the growth of GaP nanowires.

Flow-based SLS method: The great flexibility of the VLS methods described above is associated with the facile introduction and switching of semiconductor precursors and removal of by-products in a controllable way, which is generally lacking in conventional flask-based SLS methods. As such, detailed mechanistic studies of the SLS nanowire growth have been precluded. Very recently, a new flow-based SLS method using microfluidic reactors was reported (**Figure 3**), which allows for quantitative analysis of the SLS nanowire growth kinetics by precisely controlling synthetic parameters such as precursor flow rate, growth temperature, and time[36]. It was demonstrated for the first time that the SLS growth of CdSe and ZnSe nanowires involves both Gibbs-Thomson and diffusion-limited growth, which provides new insights into the poorly-understood fundamental steps in the SLS process. In addition, compared to the flask-based SLS method, the flow-based SLS method has the advantage of facile growth of colloidal semiconductor nanowires with controlled axial heterojunctions.

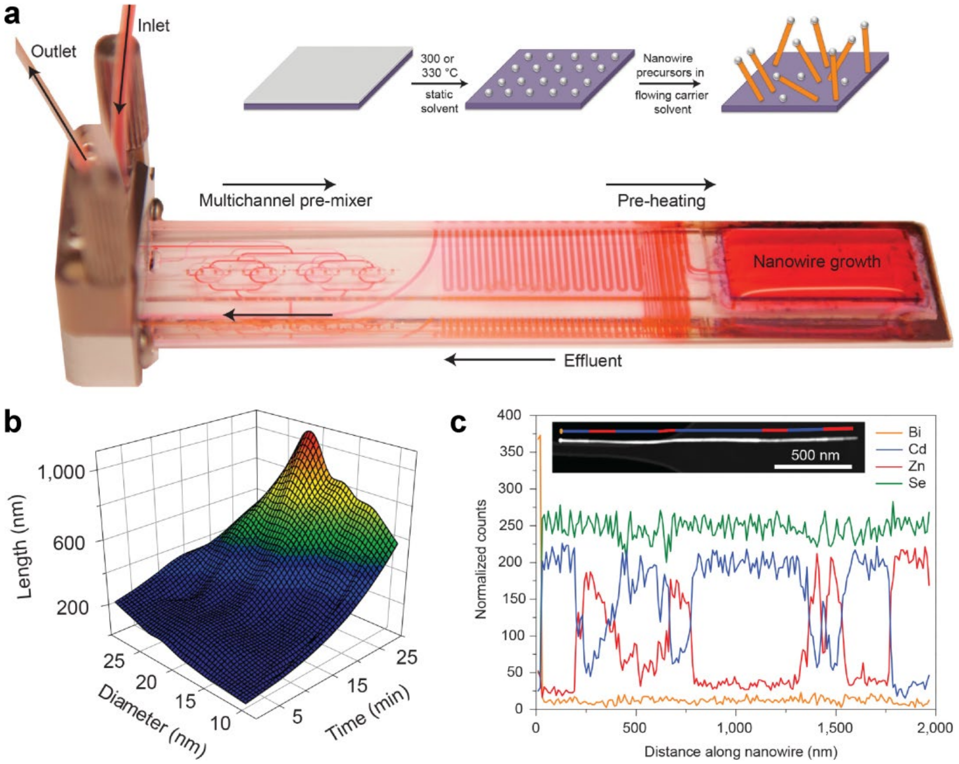

Figure 3. Flow-based SLS growth of colloidal nanowires. a) A custom-made microfluidic chip visualized by filling with red Rhodamine 6G dye. The inset schematically shows the flow-based SLS nanowire growth from catalyst-covered substrates held in a flowing carrier solvent. b) Three-dimensional length-diameter-time plot for CdSe nanowire growth at 300°C using 5-nm-thick Bi films. This plot carries information about the SLS nanowire growth kinetics. c) Energy dispersive X-ray (EDX) line-scan profile of a segmented CdSe-ZnSe nanowire with multiple axial heterojunctions synthesized by the flow-based SLS method. The inset shows the high-angle annular dark-field scanning transmission electron microscopy (HAADF-STEM) image of the nanowire. Reproduced with permission.[36] Copyright 2013, Nature Publishing Group.

SFSS growth mode: The use of a pressurized supercritical fluid can extend the solution-phase nanowire growth temperature up to ~650 °C, which is still relatively low compared to the accessible temperatures of the vapor-phase nanowire growth. When various transition metal nanoparticles were employed to grow Si and Ge nanowires in supercritical toluene at a temperature range of 450-500 °C, it was found that nanowires still grow even at a temperature more than 300 °C below the bulk metal-semiconductor eutectic temperature.[37] Although a reduction of eutectic temperature is expected due to the small sizes (~5 nm) of the metal nanoparticles, a reduction of more than 300 °C is very unlikely for the sizes investigated. Therefore, the nanowire growth appears to proceed via a SFSS growth mode.

2.2 Direct Deposition Methods

One serious concern about the metal-nanoparticle-mediated methods is foreign metal contamination,[7] which may significantly alter the nanowire properties in an uncontrolled way. Although self-catalyzed approaches do not exhibit this problem, they are not generally applicable to many important semiconductors. During the past decade, various direct deposition methods that do not involve metal nanoparticles during nanowire growth have been developed, which is attractive for many applications.

2.2.1 Selective-area epitaxy (SAE) method

The initial concept of selective-area epitaxial deposition of semiconductors on single-crystalline substrates emerged in 1960s.[38] Owing to recent advances of lithographic techniques, this old concept has been adopted to epitaxially grow vertical nanowire arrays with well controlled wire diameter and pitch. In this process, a large epitaxial substrate is first coated with a dielectric mask layer, in which nanosized openings are created using lithographic techniques and etching. Under well-controlled reaction conditions, semiconductor nanowires will grow only from the exposed epitaxial substrate in a layer-by-layer mode. For the initial growth within the opening, the mask wall confines the lateral dimension of the nanowires. Above the mask, continued one-dimensional wire growth and suppressed lateral overgrowth can only be achieved at appropriate conditions that favor the fast growth of the nanowire top facet and the significantly slow growth of the side facets.[39]

2.2.2 Seed-induced nanowire growth

Direct growth of oriented nanowires on arbitrary substrates is often desirable. This can be achieved by promoting nanowire growth on the substrate from a layer of polycrystalline seeds with the same composition as the wires. If the seed crystals are properly aligned, vertical nanowire arrays can be obtained. For randomly oriented seed crystals, the initially produced short wires/rods can be randomly oriented relative to the substrate surface. However, when the wires grow longer at higher wire density, only those wires with their orientation close to the substrate surface normal will sustainably grow because wires with their orientation significantly deviating from the substrate surface normal will be restricted by neighboring wires. As a result, dense quasi-vertical nanowire arrays can also be obtained. For example, Yang and coworkers reported solution-phase-grown ZnO nanowire arrays on substrates coated with either textured or randomly oriented ZnO nanoparticle seeds.[40] The solution-grown ZnO nanowires generally adopt the wurtzite crystal structure and grow along the *c* axis with a (0002) top facet and $(10\bar{1}0)$ side facets. At pH =11 basic conditions, it was found that the top facet is negatively charged and the side facets are positively charged, enabling control of the nanowire dimension based on facet-selective electrostatic interaction.[41]

The crystalline oxide layers of commercially available metal-oxide-coated substrates often exhibit nanoscale domains with distinct facets, which can be directly used to grow nanowire arrays with their lattice parameters matching those of the oxide layer. For example, oriented rutile TiO_2 nanowire arrays can be grown on transparent conductive fluorine-doped-tin-oxide

(FTO)-coated glass substrates by a hydrothermal or solvothermal method because of the small lattice mismatch (~2 %) between rutile TiO_2 and FTO, which also has the rutile structure.[42]

2.2.3 Screw-dislocation-driven nanowire growth

Defects exist in all crystals. The role of screw dislocation defects in promoting one dimensional growth of nanowires was recently demonstrated in detailed TEM studies of pine-tree-like nanostructures of Pb chalcogenides synthesized by chemical vapor deposition methods.[43] Continuous dislocation lines found at the centers of the nanowire trunks strongly indicate a screw-dislocation-driven nanowire growth mechanism. The screw dislocation along the wire axis induces torsional deformation, known as Eshelby twist, of the nanowire trunk. As a result, chiral nanowire branches can be formed, visualizing the Eshelby twist (**Figure 4**). However, the nanowire braches are grown via the VLS mechanism.

The screw-dislocation-driven nanowire growth mechanism has also been demonstrated in the solution-phase synthesis of colloidal nanowires.[44] In addition, vertical ZnO nanowire arrays can be directly grown from heteroepitaxial GaN substrates with intentionally created surface screw dislocations.[45] These results indicate that this wire growth mechanism may be generally useful.

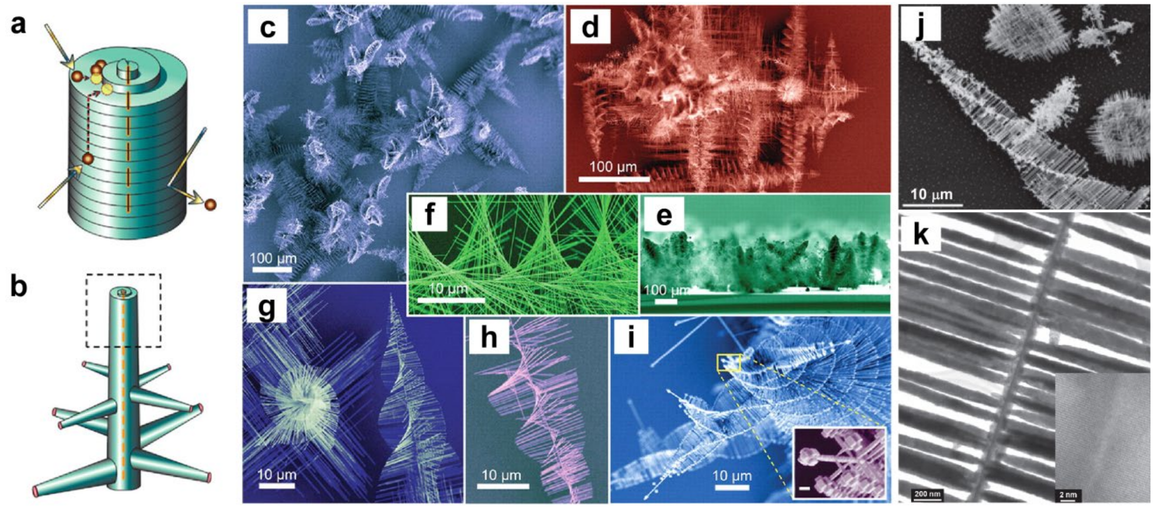

Figure 4. Screw-dislocation-driven growth of nanowires. a) Schematic model showing one-dimensional crystal growth promoted by a screw dislocation spiral. b) Schematic model showing

growth of pine-tree-like nanostructures achieved by a combination of fast screw-dislocation-driven growth of a nanowire trunk and slow VLS growth of nanowire branches. c-i) SEM images of PbS pine-tree-like nanostructures at different magnification and orientation. Helical rotation of the nanowire branches caused by the Eshelby twist of the screw dislocation in the nanowire trunk is highlighted in the high-magnification SEM images (f)-(h). Reproduced with permission.[43a] Copyright 2008, American Academy for the Advancement of Science. j) SEM image of branched PbSe NWs, showing both a chiral branched wire. k) TEM image of chiral branched PbSe NW showing screw dislocation along the axis of the central NW (high resolution image of dislocation shown in inset). Reproduced with permission.[43b] Copyright 2008, Nature Publishing Group.

2.3 Template-Directed Methods

2.3.1 Soft-template-based methods

Ultrathin metal nanowires: In general, it is synthetically challenging to prepare ultrathin nanowires with uniform diameters <~5 nm. Recently, different research groups reported synthesis of ultrathin Au nanowires using an aurophilic coordinating surfactant oleylamine, which can bind to Au^I to form one dimensional polymer-like [(oleylamine)AuCl] complex chains.[46] Importantly, the complex chains can further form micelles with one-dimensional Au^I-containing channels through self-assembly driven by van der Waals interaction between the surfactant molecules. Upon reduction, ultrathin Au nanowires having diameters as small as 1.6 nm can be produced inside the micelle channel, which efficiently limits the lateral growth of Au. By extending this synthetic concept, atomically thin Pd wires have been synthesized.[47]

Single-crystalline nanowires from biotemplates: Because the dimension of many biological objects matches that of nanowires, biotemplates are natural choices for nanowire preparation. This method typically involves two steps: (1) nucleation and growth of nanoparticles on the template surface, and (2) removal of the template by means of annealing. However, single-crystalline nanowires are rarely produced due to the lack of orientation control of the nanoparticles. Belcher and coworkers reported an attractive approach based on genetically-modified filamentous virus to synthesize single-crystalline metal-sulfide nanowires.[48] In their study, the capsid of M13 bacteriophage (<10 nm in diameter, ~1 μm in length) was modified with specific nucleating peptides, which guide oriented nucleation and growth of densely packed metal-sulfide nanocrystals on the template surface. Upon high-temperature annealing, the viral template can be completely removed and the oriented nanocrystals merge together to form single-crystalline nanowires.

2.3.2 Hard-template-based methods

Cation exchange against existing nanowires: Solid state reactions via exchange of atoms in a crystalline lattice are generally very slow at ambient conditions because of the high activation barriers for atom or ion diffusion in the lattice. As such, high temperatures are typically required for effective chemical transformations. However, a seminal study by Alivisatos and coworkers shows that cation exchange reactions in ionic nanocrystals can occur at room temperature with surprisingly fast reaction rates.[49] This method was soon adopted to achieve complete chemical transformations of ionic nanowires. For example, it was demonstrated that single-crystalline CdSe nanowires can be produced from single-crystalline Ag_2Se nanowires by cation exchange reaction between Cd^{2+} and Ag^{+}.[50] Interestingly, partial cation exchange reactions under well-controlled conditions have resulted in nanowire superlattices and core/shell nanowires with abrupt interfaces.[51]

Arbitrarily long nanowires by electrospinning: The electrospinning technique emerged about a century ago and was recognized as a powerful method for fabrication of polymer wires in 1990s.[52] Basically, this method uses electric force to overcome the surface tension of a surface charged droplet of polymer solution. As a result, a thin polymer jet is ejected from the droplet to a counter electrode. During this process, the solvent evaporates and solid polymer nanowires precipitate on the counter electrode. Because the jet ejection can be continuous, the produced polymer wires can have arbitrary length.

During the past decade, the electrospinning method for making polymer wires has been rapidly developed, in combination with sol-gel chemistry, to fabricate continuous inorganic/polymer hybrid nanowires.[53] Upon removal of the organic polymer, inorganic nanowires, which are typically polycrystalline, can be produced.

Hierarchical nanowires from templates with complex structures: Porous templates with one-dimensional channels are often used to produce nanowires. One of the most commonly used porous templates is anodized aluminum oxide (AAO) with cylindrical nanochannels. By applying multistep anodization at well-controlled anodizing voltage for each step, hierarchically branched AAO temples with multiple generations of branched channels can be produced and subsequently used to fabricate nanowires with controlled multilevel branching structures by electrochemical deposition.[54]

Mesoporous silica, such as SBA-15 with hexagonal array of nanopores, has also been widely used as template for nanowire production. Interestingly, when the synthesis of SBA-15 is conducted inside physically confined AAO channels, a variety of complex mesostructured silica with chiral mesopores can be obtained due to confined assembly of inorganic-organic composite structures.[55] The silica mesostructures with chiral nanochannels are unique templates for fabricating nanowires with morphologies that cannot be achieved by other methods.

2.4 Oriented-Attachment Method

Since the seminal report of spontaneous formation of single-crystalline nanowires by oriented attachment of zero-dimensional nanocrystals,[56] continued research efforts during the past decade based on this approach have resulted in nanowires with controlled morphology and dimensions.

2.4.1 Shape-dependent oriented attachment

Although PbSe with rock salt crystal structure has a highly symmetric cubic lattice, Talapin, Murray, and coworkers demonstrated that oriented attachment of PbSe nanocrystals can still occur, but strongly depends on the shape of the nanocrystals, which can be tuned by adjusting the synthetic conditions.[57] When the PbSe nanocrystals are perfectly symmetric, such as PbSe cubes, oriented attachment does not occur due to the lack of a permanent dipole moment. In contrast, quasi-spherical nanocrystals enclosed by six {100} facets and eight {111} facets tend to form straight nanowires via oriented attachment along the <100> or <110>direction depending on the stabilizing surfactants. Because the arrangement of the Pb- or Se-terminated {111} facets can be non-centrosymmetric, permanent dipole moments along the <100> and <110> directions do exist and drive the oriented attachment of quasi-spherical nanocrystals along those two directions. At different synthetic conditions, either octahedral PbSe nanocrystals enclosed by eight {111} facets or branched star-shape PbSe nanocrystals with {100} end facets are produced. Interestingly, zigzag or radially branched PbSe nanowires can be correspondingly obtained by oriented attachment of these nanocrystals either by sharing the {111} facets or along the <100> direction.

2.4.2 Ultrathin semiconductor nanowires

Because nearly monodisperse nanocrystals having small diameters <~5 nm can now be routinely synthesized for many semiconductors, the oriented attachment method is arguably the most attractive method to produce ultrathin semiconductor nanowires with controlled diameters. For example, ultrathin single-crystalline CdSe nanowires (or quantum wires) having uniform diameter as small as 1.5 nm have been synthesized by the oriented attachment of magic-sized CdSe clusters or their aggregates in the presence of primary amines with long hydrocarbon chains.[58]

2.4.3 Nanowire length control by oriented attachment of nanorods.

It is challenging to control the length of nanowires obtained by oriented attachment of zero-dimensional nanocrystals due to the uncontrolled attachment kinetics. On the other hand, it is difficult to achieve end-to-end oriented attachment of quasi-one-dimensional nanorods because of the unfavorable steric barrier. Recently, Ryan and coworkers demonstrated that nearly monodisperse wurtzite CdS or Ag_2S nanorods with (001) end facets can be spontaneously elongated by length multiplication to produce single-crystalline nanowires.[59] The critical step for this success is a washing step using octylamine, which can selectively de-passivate the (001) end facets and initiate the oriented attachment reaction in an end-to-end fashion.

3. Nanowire Electronics

Nanowires can serve as the most basic component of integrated circuitry: the field effect transistor (FET). The need for more powerful electronic systems necessitates the use of nanoscale device components, which can be enabled by the controllable dimensions of various nanowire materials. Various nanowire materials and FET geometries have been utilized to take advantage of the benefits of single-crystalline materials in the nanometer size regime. Typical nanowire diameters provide axial cross sections from 30,000 nm^2 down to 20 nm^2, allowing for the active regions to be tailored to specific device needs. Shortening the active channel by chemically controlling the placement of contacts also provides an avenue for high density device attainment. However, when accompanied by large aspect ratios, nanowires can still interface with top-down fabrication processes such as standard photolithography techniques, allowing for utilization of the naturally conductive pathway along the unconstrained dimension. Moreover, semiconductor nanowire materials retain the ability of their bulk counterparts to be controllably doped, a critical degree of freedom needed for practical device applications.

3.1 Si Nanowire Electronics

Due to its rich history of use in the microelectronics industry, no material has been investigated for device applications more than silicon. This makes silicon nanowires (SiNWs) ideal for fundamental research, while retaining compatibility with current Si-based electronic processing techniques for eventual integration. Early SiNW FETs demonstrated the ability to control carrier type and density via a back-gated geometry (**Figure 5**a,b), albeit with relatively poor mobility and low transconductance.[60] Since nanowires have relatively large surface-to-volume ratios, defects trapped at the Si/SiO_x surface have profound effects on the device performance by compensating applied gate voltages and increasing the trapping and scattering of mobile charge carriers.[61] The application of certain surface treatments, including hydrogen-termination[62], atomic layer deposition[63], and organic coatings[64], greatly lowers the density of these defects, thereby increasing the FET response of the active SiNW channel (Figure 5c).[65] Such passivation techniques are commonly employed in Si-based device manufacturing, but become increasingly important to preserve the desired electrical properties as the surface-to-volume ratio increases in nanowires with decreasing dimensions. Using these passivation techniques, SiNWs less than 7 nanometers in diameter maintained pristine Si surfaces for several days.[66] Typical regression of the surface to an oxidized state (as observed in planar Si) can limit the effectiveness of such surface treatments, but nanowires in this ultra-small size regime exhibit increased resistance to such oxidation.[67]

In addition to passivating the nanowire surface, contact control and optimization is paramount for maximum device performance. Due to their low contact resistances and relatively low formation temperatures, silicide-Si junctions have been utilized by both conventional silicon technologies[68] as well as SiNW devices for source drain contacts. Thermal formation of Ti[69], Ni[70], or Pt[71] silicide via rapid thermal annealing (RTA) after metallization of the contacts can provide Ohmic behavior, as well as lowered contact resistances when compared to the as-deposited contacts. For example, measured two-terminal resistances of p-type SiNWs using Ti metal contacts exhibit over 2.5 orders of magnitude reduction after thermal annealing (Figure 5d).[64a] Care must be taken when attempting to form these silicide contacts, however, as the silicide phase formed depends on the crystallographic direction of the SiNW[72] and is not necessarily the same as what would form in the bulk under similar conditions.[73] While the use of these contacts can increase performance, adverse effects on measured dependences due to the contacts can still be present when only a 2-terminal measurement is performed. It was shown that Ni-contacts on n-type SiNWs exhibited an erroneous mobility dependency on dopant concentration, even with thermal treatment to reduce contact resistance.[74] Only after the contact resistance is taken into consideration can the material-dependent relation be determined, illustrating the importance of using 4-point contact schemes when feasible (Figure 5f).

Device miniaturization requires not only contact resistance optimization but precise control over the positioning as well. This can be achieved by defining contact areas via lithography, provided the nanowires are not shorter than the resolution of the utilized technique. However, much shorter channel lengths can be achieved by thermally driving the axial diffusion of the Si/silicide interface away from the original deposition area or by using other nanowires as deposition masks.[75] The interfaces created in this method can be atomically sharp and allow for nanometer-scale definition of the active channel (Figure 5g,h).

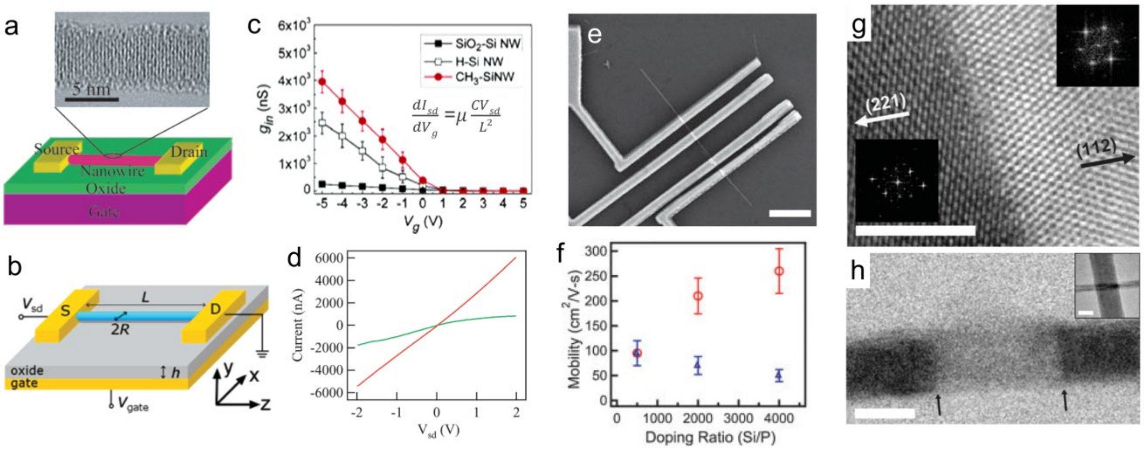

Figure 5. Nanowire field effect transistors. a) Schematic of a typical 2-terminal back-gated nanowire field effect transistor with (top) a HRTEM image of a 5 nm diameter SiNW. Panels (a) and (d) Reproduced with Permission.[64a] Copyright 2003, American Chemical Society. b) Schematic of the various geometric considerations for NWFETs. Reproduced with permission.[76] Copyright 2007, American Chemical Society. c) Change in measured mobility in a SiNW with various surface treatments. Inset equation is used to calculate the mobility, where I_{sd}, V_g, m, C, V_{sd}, and L are the source-drain current, gate voltage, mobility, gate capacitance, source-drain voltage, and channel length, respectively. Reproduced with permission.[64b] Copyright 2006, American Chemical Society. d) Difference in resistance from before (green line) and after (red line) thermal annealing. Reproduced with permission. e) SEM image of a 4-terminal electrical device of a SiNW, scale bar of 1 mm. Reproduced with permission.[77] Copyright 2009, Nature Publishing Group. f) Mobility as function of doping without consideration of contact resistance (blue triangles) and with consideration (red circles). Reproduced with permission.[74] Copyright 2004, Wiley-VCH. Images illustrating the Si/$SiNi_x$ interface at high resolution with the corresponding FFT patterns of each phase (g) and nanoscale control of channel length (h) by masking with another SiNW (inset). Reproduced with permission.[75] Copyright 2004, Nature Publishing Group. Scale bars for (g), (h), and inset are 5, 10, and 20 nm, respectively.

3.2 Nanowire Field Effect Transistor (NWFET) Geometries

The most commonly used NWFET geometry is back-gated (Figure 5b), as this requires relatively little effort during fabrication. It involves creating source-drain electrodes on a highly doped Si substrate coated with thermally grown SiO_2 to acting as the metallic gate and gate dielectric, respectively. The system capacitance can be measured, but it is typically calculated by the cylinder-plane model. The assumptions of this model include, but are not limited to, the following: the active channel is metallically conductive; the dielectric layer thickness is much shorter than the nanowire length; the nanowire has a circular cross section; and the nanowire is completely incorporated in the dielectric.[78] While measures can be taken to satisfy some of these requirements, the last one is necessarily not satisfied by the back-gated geometry, where the nanowire lies exclusively on top of the dielectric. This missing dielectric material can cause the analytical equation to only give the upper limit of the gate capacitance (**Figure 6**a), causing an underestimation of the nanowire mobility (equation in Figure 5c) .[79] However, corrections to the analytical capacitance formulas for both the finite length and non-metallic conductivity of nanowires were produced by solving the three-dimensional Poisson's equation numerically, thereby allowing for more accurate measurements using the back-gated geometry.[76] Similarly, the effect of non-circular nanowire cross-sections have also been modeled.[80]

Alternatively, there exist a number of NWFET geometries that hold greater promise for industrial and scientific applications, although they typically require more complicated fabrication processes. The top gated NWFET (Figure 6b) requires a gate dielectric to be grown or deposited on the nanowire surface, followed by deposition of the gate metal. This more closely mirrors the ideal embedded dielectric structure, allowing for more accurate calculation of the gate coupling (Figure 6a). Without such an imbedded structure, nanowire mobilities can be severely underestimated if the actual system capacitance is not known. This also provides a large capacitance per unit area, lowering the necessary operating gate voltages. This device structure has been used to measure the energy spacing between 1D subbands in Ge/Si core/shell nanowires responsible for observed ballistic transport.[81] The same core/shell system and top-gated device structure was also shown to produce NWFETs with excellent mobility and transconductance values when a high-k dielectric was used.[82]

Both back- and top-gated geometries involve nanowires lying in the plane of a substrate, a direction not necessarily ideal for electronic integration since most growth techniques produce nanowires in various orientations away from the surface plane. Therefore, geometries with vertical nanowire channels have been developed. Figure 6c shows a schematic of a single vertical nanowire FET, where the gate is placed at the end of the channel over the drain.[83] This allows the gate bias to not only modulate the charge carrier density but to also add to the acceleration of electrons at the drain. In an approach more closely related to standard FET geometries, the benefits of the top-gated geometry can be extended to vertically aligned nanowires, wherein the gate metal and dielectric completely surround the nanowire (Figure 6d,e). This can be achieved by conformal deposition of various dielectric materials around the vertical nanowire channel using chemical vapor deposition.[84] However, if the material can be controllably oxidized (as in the case for Si), thermal conversion of the surface into a gate dielectric provides the ability to achieve channel diameters much smaller than can be grown[85] (considering survival after processing), while also benefiting from a lower density of charge-trapping states near the core/shell interface[86] compared to a deposited oxide.[87]

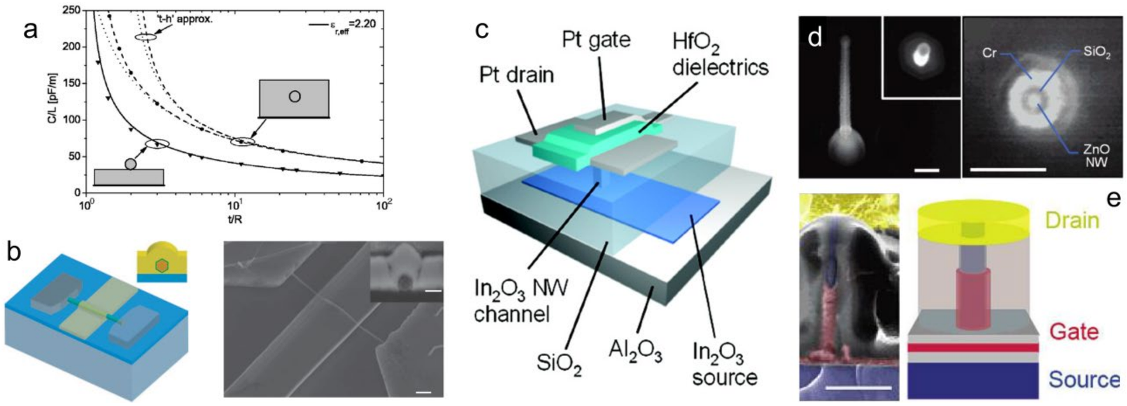

Figure 6. NWFET geometries. a) Gate capacitances per unit length with SiO_2 gate dielectrics in the back-gated geometry as function of t/R, where t and R are the distance between the gate and center of the nanowire and the radius of the nanowire, respectively. Reproduced with permission.[79] Copyright 2006, American Institute of Physics. b) Schematic (left) and SEM image with scale bar of 1 mm (right) of a top-gated NWFET. The inset is a cross-section of the device structure with a scale bar of 100 nm. Reproduced with permission.[88] Copyright 2009, Nature Publishing Group. c) Schematic representation of a vertically-integrated In_2O_3 NWFET, with the gate electrode over the drain electrode. Reproduced with permission.[83] Copyright 2004, American Chemical Society. d) SEM images (scale bar is 200 nm for each) of a vertical NW cladded with oxide and metal along the length (left) and through the cross-section (right). Reproduced with permission.[84b] Copyright 2004, American Chemical Society. e) SEM image of a vertically integrated surround-gate NWFET and corresponding pictorial diagram (scale bar is 500 nm). The false coloring is for added clarity of position for the various device components. Reproduced with permission.[86] Copyright 2006, American Chemical Society.

3.3 Dopant Distribution and Effectiveness

Early work on controlling the carrier type and concentration of SiNWs allowed for the creation of various devices, but a deeper understanding of the dopant effectiveness and distribution in SiNWs has been gained since that time. For example, charge depletion as a result of surface states (even on passivized surfaces) can limit the effective channel diameter, creating the need to distinguish between the physical radius and electronic radius, the latter of which more accurately defines the charge-carrying cross-sectional area (**Figure 7**a). Furthermore, dielectric mismatch between a nanowire and the surroundings can also cause changes in electrical behavior by increasing the ionization energies for dopants near the nanowire surface.[89] This effectively deactivates the dopants near the surface of the active channel not covered by the gate stack.[77] However, given an adequate doping density and surface treatments, SiNWs as small as ~1 nanometer in diameter can overcome this effect to exhibit bulk-like resistivities.[90] While this effect was demonstrated in SiNWs, it is universal to all semiconducting nanowires.

Additionally, it has been shown that most synthetic techniques do not produce SiNWs with uniform dopant distributions, as is assumed in the calculations of dopant concentrations in a nanowire FET. Through capacitance-voltage measurements, the radial dopant profile in post-annealed SiNWs was found to not be constant, as expected from the finite time and temperature used in the dopant diffusion process (Figure 7c).[88] However, even when SiNWs are doped during growth, the distribution of dopants is not necessarily uniform. Boron dopants have been found to form a concentration gradient along the length of VLS-grown SiNWs, with the lower amount of boron always occurring on the catalyst end.[91] A similar result was obtained by using atom probe tomography to directly measure the dopant concentrations in arbitrary regions of individual Ge nanowires (Figure 7d).[92] These non-uniformities can possibly be attributed to unintentional surface doping and dopant diffusion occurring during synthesis, which can be suppressed and overcome to produce doping concentration variations that are over 2 orders of magnitude reduced (Figure 7e,f).[93] While these studies were performed on Si and Ge nanowires, assumptions made on dopant distributions in any nanowire material need to be considered with additional care.

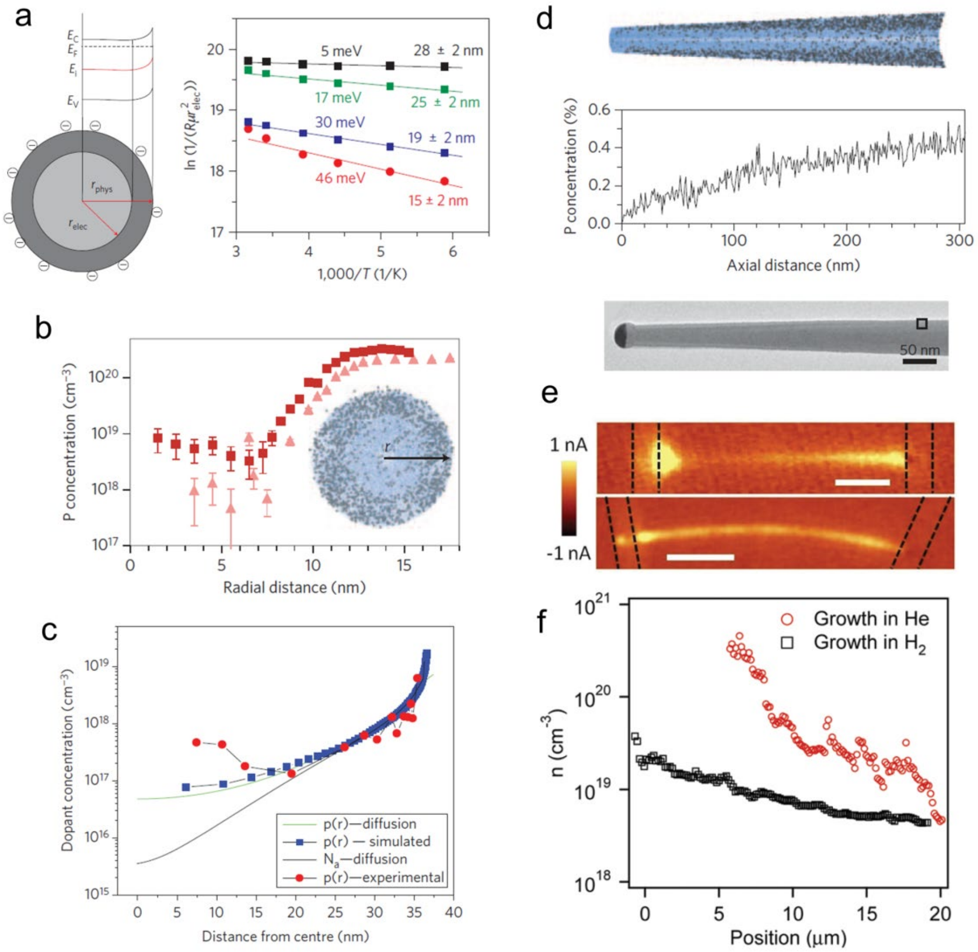

Figure 7. Dopant effectiveness and distribution. a) Pictorial representation of the effect surface states have on depletion at the surface of a nanowire, including corresponding band diagram (left). Arrhenius plot for nanowires of various diameters, showing that dopants in smaller nanowires have higher ionization energies (right). Reproduced with permission.[77] Copyright 2009, Nature Publishing Group. b,c) Radial distribution of dopants in Ge and Si nanowires as measured by atom-probe tomography (APT) and electrical C-V methods, respectively. The difference in dopant profiles approaching the surface is likely due to the different doping techniques used (during growth versus post-growth annealing). d) Dopant profile along the axis of a Ge nanowire (TEM image below) as measured by APT. Panels (b)-(d) reproduced with permission.[88, 92] Copyright 2009, Nature Publishing Group. e) Photocurrent maps comparing SiNWs grown in He (top) and H_2 (bottom) conditions illustrating the results of dopant inhomogeneity from one end to the other (f). Reproduced with permission.[93] Copyright 2011, American Chemical Society.

3.4 Germanium, Metal Oxide, and III/V Nanowire FETs

Many other III/V, sulfide, and oxide materials have been explored using various device geometries. As opposed to using these materials to optimize device performance, many studies use the device characteristics to gain information about carrier concentrations and mobilities of the nanowire material acting as the active channel. This mode of operation can be used as a powerful means of quantitative comparison between synthetic techniques of similar materials, assuming careful and knowledgeable device operation and data analysis.

Germanium nanowires (GeNWs) hold many chemical similarities to SiNWs, leading to a similar ability to control the carrier type and concentration.[94] However, there do exist some important differences. In particular, the stability of the oxide makes them very sensitive to oxidation and corrosion. Therefore, surface passivation techniques have been studied and developed specifically for GeNWs so that electrical stability can be achieved even in oxidative conditions.[95] With these considerations in mind, both back- and top-gated GeNW FET geometries have exhibited excellent device performance.[96]

III/V materials have also been incorporated into various FET geometries with the goal of either high device performance or material characterization. Early work on nanowire electronics involved InP nanowires that were assembled to provide larger-scale electronic devices from the bottom up.[97] Since that time, nanowire devices using high-mobility materials have exhibited similar properties to their bulk counterparts. Top-gated InAs nanowires exhibited mobilities as high as 6580 $cm^2V^{-1}s^{-1}$ without the assistance of passivation,[98] although passivation has been shown to improve the sub-threshold slope.[99] Surface properties such as roughness can still contribute to charge scattering in small (< 20 nm) diameter nanowires.[100] Gallium nitride nanowire FETs can exhibit electron mobilities ranging from 65 $cm^2V^{-1}s^{-1}$ for low-temperature MOCVD synthesis[101] to 650 $cm^2V^{-1}s^{-1}$ for high-temperature laser-assisted growth,[102] without consideration of contact resistance. The carrier type can be switched to holes via sufficient doping with magnesium, as demonstrated in thin film devices, but hole mobilities are lower (~12 $cm^2V^{-1}s^{-1}$).[103]

Several metal oxides, including ZnO, In_2O_3, and SnO_2, have also been studied using nanoscale devices. ZnO NWs are perhaps the most studied among the oxides, and their conductivity can range from insulating to highly conductive without the use of external dopants. Intrinsic defects such as oxygen vacancies and zinc interstitials act as donors, causing as-made samples to be more electrically conductive than the band gap alone would suggest.[104] Depending on the synthetic conditions, ZnO nanowire FETs typically yield electron mobilities and carrier concentrations anywhere between 5-25 $cm^2V^{-1}s^{-1}$ and 10^{16}-10^{18} cm^{-3}, respectively,[105] although much higher mobility values have been reported when device conditions are optimized.[106] Group III elements, such as Ga,[107] In,[108] and Al,[109] have all been used to increase the electron concentration when substituted for Zn. On the other hand, many studies have focused on inducing hole conduction with the goal of creating homojunction optoelectronic devices. P-type conduction has been reported in ZnO nanowires by directly creating acceptor states using Li,[110] P,[111] and N[112] as a substitutional dopant for Zn and/or O. Indirect doping, using Sb to create structural features that induce extra rows of oxygen atoms that act as acceptor states, has also been demonstrated.[113] Due to the eventual compensation of electrons from intrinsic donors whose formation energy is inversely related to the concentration of active acceptors,[114] continuing work in this area has focused on the stability and reproducibility of electrical properties. In addition to ZnO, intrinsically insulating SnO_2 nanowires can be doped with Sb[115] or Ta[116] to increase conductivity, yielding transparent FETs with mobilities ranging from 150 to 550 $cm^2V^{-1}s^{-1}$, respectively. Likewise, In_2O_3 nanowires typically have intrinsically high resistivities, with electron mobilities as high as 71 $cm^2V^{-1}s^{-1}$,[117] yet they can be controllably doped to metallic-like conductivity levels using Sn or Mo.[118]

3.5 Electronic Sensor Devices

Much of the early work on SiNW FETs focused on mitigating the effects of the surface on conduction, in order to maintain the pristine nature of the single crystal nanowire channel. However, this sensitivity to surface changes can be quite advantageous for sensing applications. Chemical, molecular, and biological detection at extremely low concentrations is made possible by measuring the change of an electrical signal resulting from reactions and/or effects of species on the surface of the nanowire channel, even if the exact mechanisms may not be fully understood. Ideally, a change in the electric field around the nanowire channel that results from binding of a charged species will cause a corresponding change in conduction, effectively acting as a top- or surround-gate electrode. The binding of specific species can be targeted by functionalization of the surface with materials or molecules that promote the intended interaction. While similar effects can be observed in planar sensors, nanowires can have radii on the order of the Debye length (the distance within which electron exchange can take place between the surface and the bulk), making the entire channel susceptible to surface changes. These considerations allow for real-time, high-sensitivity, and high-selectivity sensing using sensors that incorporate nanowires.

Several nanowire materials that have been extensively studied as active channels in FET devices have also been explored for sensing applications. Specifically, the surfaces of metal oxides, upon which a specific reaction can occur, serve as excellent gas sensors. For example, electrical detection of O_2 and CO has been achieved using SnO_2 nanowires.[119] **Figure 8**b schematically illustrates the reaction of these gaseous species with the NWs. The formation of oxygen vacancies (electron donors) at the nanowire surface is a result of interaction with a combustible gas (CO), which increases the conduction of the nanowire channel due to accumulation. In an oxidative environment, the oxygen vacancy concentration is reduced, restoring the SnO_2 to an insulating state by depletion (Figure 8a). The relative oxidative/reductive potential of the SnO_2 surface can be influenced by creating photogenerated holes upon UV irradiation, leading to sensible changes in channel current from controllable adsorption/desorption of reactive species.[120] Similar work showed that intrinsically conductive SnO_2 can exhibit fast response times and a high sensitivity to slight changes to the relative humidity in air (Figure 8c).[121] Even greater chemical reactivity and selectivity can be achieved by either the addition of catalyst particles to help facilitate the redox process[122] or by independently controlling the electron density via a gate bias.[123] Likewise, In_2O_3 and TiO_2 nanowires have also exhibited high sensitivities to specific chemical species, including NO_2 and NH_3.[124] Detection as low as ~20 ppb of NO_2 was achieved using a single In_2O_3 nanowire device, with 5 ppb detection possible when multiple devices are used.[125] While materials grown by bottom-up methods are usually used in these devices, top-down processes can be used to define the active channel as well, as was demonstrated by sensing gaseous ethanol with fully integrated TiO_2 nanowires etched from a deposited thin film (Figure 8d,e).[126]

Similar to the previous oxide materials, ZnO nanowires have been utilized to sense chemical species including, ethanol,[127] oxygen,[105a, 128] and hydrogen.[129] When studied within NWFET devices, the ZnO nanowires exhibited an increase in threshold voltage as a function of the partial pressure of oxygen, indicating a decrease of mobile electrons that result from the surface interaction with oxygen (Figure 8f). Since the sensitivity of a sensor can suffer from either an excess or shortage of electrons depending on the concentration and magnitude of an effect on the nanowire channel, the carrier concentration can be kept at the optimal value for maximum sensitivity. This typically occurs in the subthreshold region by controlling the charge population with an applied gate bias.[130] Furthermore, adsorbed molecules can be controllably desorbed with application of a large negative gate bias, the magnitude of which can be used to distinguish between chemical species (Figure 8g).[131]

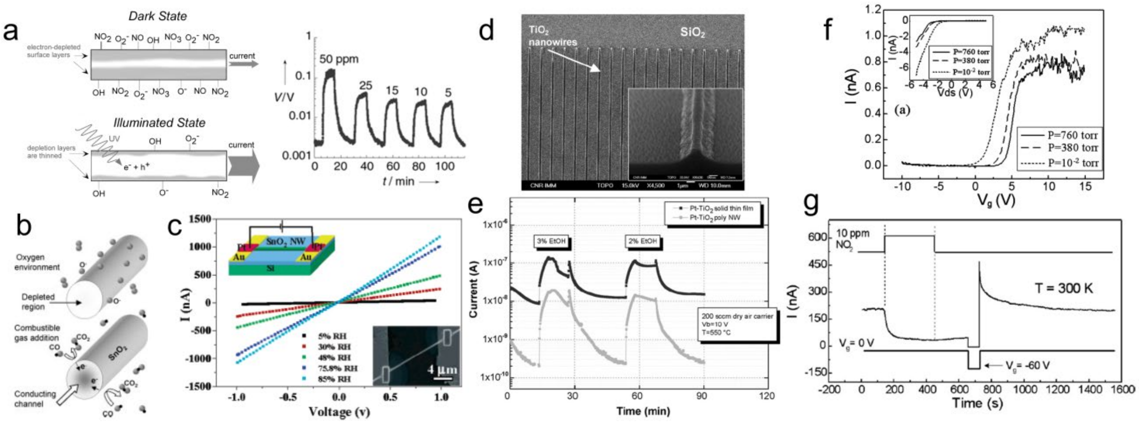

Figure 8. Nanowire chemical sensors. a) Schematic (left) of NO_2 sensing mechanism in SnO_2 nanoribbons under UV irradiation, which leads to increased wire conductivity and a reduced depletion layer thickness. This enables NO_2 sensing (right) with a resolution limit of 5-10 ppm. Reproduced with permission.[120] Copyright 2002, Wiley-VCH. b) Mechanistic schematic of chemical species interaction (reaction below) with the surface of SnO_2 nanowires. Reproduced with permission.[119] Copyright 2003, Wiley-VCH. c) Current responses to various relative humidity percentages vs. applied source-drain bias. Insets are an illustration and SEM image of the 2-termal nanowire sensor device. Reproduced with permission.[121] Copyright 2007, American Chemical Society. d,e) SEM image of top-down fabricated TiO_2 nanowires with ethanol sensing performance (light squares) with time as compared to a thin film control device (dark squares). While higher currents are observed in the film sample, higher sensitivity is observed in the nanowire device. Reproduced with permission.[126] Copyright 2008, Elsevier. f) Transconductance of a ZnO NWFET under various pressures with corresponding I-V_{sd} curves (inset). Reproduced with permission.[128b] Copyright 2004, American Institute of Physics. g) Current response (middle line) of a ZnO nanowire over time when in the presence of NO_2 (top line) and when reset by a large gate bias (bottom line). Reproduced with permission.[131] Copyright 2005, American Institute of Physics.

Nanowire sensors are not limited to the detection of gaseous chemical species. Much work has been directed at the specific detection and sensing of organic and biological species. As opposed to the case of metal oxide nanowires, the sensing species does not react directly with the nanowire surface, typically requiring chemical modification with functional groups to increase the measureable interactions. Due to the vast amount of data concerning surface functionalization in silicon, SiNWs can be easily modified to serve as specific and sensitive sensors for biological receptor groups in addition to molecular detection.[132] Once immersed in an aqueous solution containing the species of interest with net charge, a corresponding change in surface potential can be electrically detected.

SiNWs were first used as chemical and biological sensors by Cui et al.[133] in 2001, and many subsequent studies have demonstrated the robustness, sensitivity, and specificity that SiNW sensors can provide. For example, SiNW sensors functionalized with PNA receptors exhibit real-time, ultrasensitive detection of DNA, down to ~10 femtomolar concentrations.[134] Through the use of covalently linked antibody receptors to the silicon surface, the detection of single viruses using SiNW array devices was also accomplished (**Figure 9**b).[135] Real-time, label-free detection of cancer markers[136] and prostate-specific antigens[137] have also been realized through the utilization of SiNW sensors with appropriate surface modifications (Figure 9a,c). A general approach to incorporate specific SiNW devices to sense specific biological species has also been developed in great detail,[138] as well as the demonstration of immunodetection with CMOS-compatible fabrication techniques.[139]

While real-time detection of various biological species has been demonstrated at low concentrations due to the increased signal-to-noise ratio inherent to the nanowire structure, certain considerations have been examined to optimize device performance. For example, it has been shown that the sensitivity of DNA detection varies as a function of the DNA strand from the SiNW surface.[140] The observed decrease of sensitivity with increasing distance from the surface is a result of charge screening provided by the electrolyte.[141] Additionally, mass transport effects in the sensing medium can limit the overall sensitivity.[142] In static or conventional microfluidic configurations, even nanoscale sensor sensitivities are unlikely to exceed the ~femtomolar range for assays performed on the order of minutes. Additionally, ultrafast detection (< 100s) at femtomolar concentrations may also be difficult to achieve in practice due to the tradeoff between settling time and detectable concentration,[143] although careful control of the Debye length and velocity of injected solution can allow for faster detection speeds.[144] Therefore, failure of detection may not be due to the intrinsic nanowire sensor itself, but rather a limit of the system.

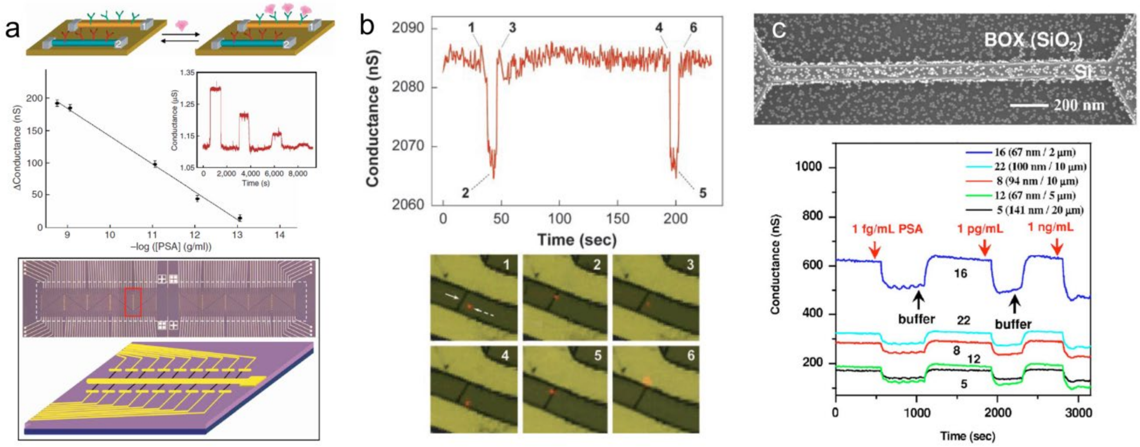

Figure 9. Nanowire biological sensors. a) (top) Schematic of SiNW devices modified with different antibody receptors, making interaction device specific. (middle) Change in conductance as a function of prostate specific antigen (PSA) in a surface-modified SiNW device. The inset is the actual conductance as a function of time when various buffer solutions are used. (bottom) Optical image of a nanowire device array above a schematic of the electrode and nanowire configuration (rotated 90° from optical image). Reproduced with permission.[136] Copyright 2005, Nature Publishing Group. b) (top) Conductance responses and (below) corresponding optical images tracking the position of a single influenza virus (red dot) relative to the SiNW (white arrow). Reproduced with permission.[135] Copyright 2004, National Academy of Sciences, USA. c) (top) SEM image and (bottom) real-time conductance of a SiNW channel fabricated from a Si-on-insulator substrate with 13 nm Au nanoparticles conjugated with DNA immobilized on the surface. The dimensions of the various channels are given in the graph (channel number and width/length). Reproduced with permission.[137] Copyright 2007, American Institute of Physics.

4. Nanowire Photonics

Nanowires as photonic components have gone through more than a decade of intense studies. These nanoscale materials provide a natural and versatile platform for miniaturized optical and optoelectronic devices — a general effort across semiconductor industries. The desire for device miniaturization has led to a variety of opportunities and challenges, and nanowires have exhibited advantageous light emitting, photon collecting, and optical wave manipulating functions.[145]

4.1 Nanowire Waveguides

Nanowires are naturally one-dimensional optical waveguides with nanoscale cross-sectional areas. Nanowires synthesized chemically (using bottom-up methods) are particularly interesting because their atomically smooth side walls allow photons to propagate along the nanowires with low losses. These subwavelength waveguides are critical for the development of photonic circuits, where light generated from one miniaturized source needs to be captured and delivered precisely to the next components along the logic operation trains.

Among the various nanowires which have been studied, those composed of binary oxides exhibit several advantages including single crystallinity, a high degree of flexibility, and high refractive indices. Tin dioxide (SnO_2) nanoribbons, for instance, have proven to be excellent subwavelength waveguides for light above the wavelength of their band-edge emission.[146] With a geometrical cross section of 100-400 nm, these nanoribbons have demonstrated efficient waveguiding with losses from 1-8 dB/mm at a wavelength of 450-550 nm, which is sufficient considering the typical dimensions of photonic circuits. Under UV illumination, these nanoribbons can emit visible light and serve as the nanoscale light source and waveguide simultaneously; alternatively, because of their remarkable mechanical flexibility, SnO_2 nanoribbons can be linked to other photoluminescent nanowires (e.g. GaN and ZnO) and plasmonic nanowires[147] and have even coherent lasing pulses launched into the nanoribbons with simple tangential evanescent coupling schemes. In addition to guiding light in air, SnO_2 nanoribbons are capable to guide optical propagation in water or other liquid media because of their large refractive index (n = 2.1).[148] Such a capability is particularly important for applications such as on-chip chemical or biological spectroscopy.

Nanowire waveguides can exhibit more active functions rather than simply passive waveguiding. SnO_2 nanoribbons with nanoscale cross sections can be used as short-pass filters as broadband light propagating along the nanowires. Cut-off frequencies of 465 nm, 492 nm, 514 nm, 527 nm, and 580 nm have been observed in SnO_2 nanowires with cross-sectional dimensions of 310 nm x 100 nm, 280 nm x 120 nm, 350 nm x 115 nm, 250 nm x 225 nm, and 372 nm x 140 nm, respectively.[146] With unique geometries such as multi-branched nanoribbon assemblies, light sorting and color-differentiated optical routing can be achieved based on the dimension-dependent filtering effect. Nanowires are also prominent candidates for biochemical sensing. While evanescent wave sensing has been demonstrated using conventional optical fibers, subwavelength fibers can carry a larger fraction of their modal power outside of the core and therefore enhanced the interactions between the guided optical modes and the adsorbed molecules.[148] No matter whether the sensors are operated based on optical absorption or perturbation of local refractive index of adsorbed molecules, improved sensitivity was observed with reduced thickness of the nanoribbons.[146]

The strong light-matter interactions in the nanowires were also reported via laterally confined resonances. Nanowires with subwavelength diameters can be viewed as scaled-down version of microcylinder resonators that can weakly trap light in circulating orbits by multiple total internal reflections.[149] Compared to micrometer-scale resonantors, the resonant modes confined in nanowires tend to be leaky and interact more effectively with the outside media. Reciprocally, the light illuminated vertically (in contrast to the end-firing scheme) onto the nanowires can penetrate into the nanowires and form resonances therein.[149] Enhanced optical absorption and photocurrent was reported in Ge nanowire photodetectors by taking advantage of the leaky mode resonances (**Figure 10**b). Theoretical work showed that this concept can be generally applied to a wide variety of nanoscale semiconductor devices including solar cells,[150] light emitters, and lasers. More importantly, leaky mode resonances with the corresponding absorption enhancement can be conveniently tuned to desirable a wavelength by varying the lateral dimensions of the nanowires.

Another property that can be purposely tuned in compound nanowires is the chemical composition of the nanomaterials. In fact, the nanowire geometry offers a unique platform for epitaxial alloy growth because of its large surface-to-volume ratio and strain relieving properties. Moreover, a compositional gradient along the length of CdS_xSe_{1-x} alloy nanowires has been reported using an evaporation-source controlled CVD system (Figure 10c).[151] The bandgap of these nanowires can be tuned from 2.4 eV at one end of a single nanowire to 1.7 eV at the other end. A uniform compositional gradient was evident from the continuous photoluminescent color variation observed along the nanowire under blue illumination (405 nm). Compared to homogeneous nanowire waveguides, such composition-graded nanowires exhibit rather unique waveguiding properties. Light propagation along one axial direction of the nanowires is different to the propagation along the reverse direction, leading to asymmetric light propagation – a crucial function needed for photonic circuit building blocks such as photonic diodes or transistors.

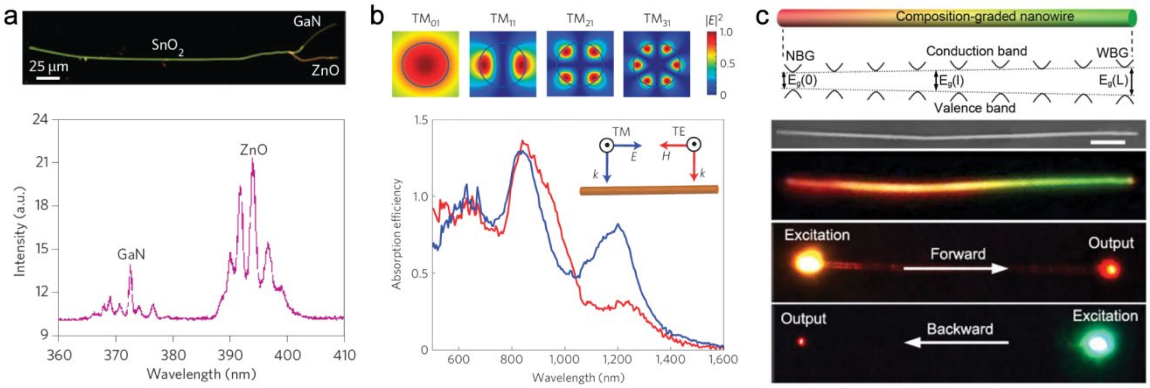

Figure 10. Nanowire waveguides. a) Individual oxide nanoribbons can act as subwavelength optical waveguides and interconnect multiple photonic nanostructures. Reproduced with permission.[148] Copyright 2005, National Academy of Sciences, USA. b) Leaky-mode resonances, which can gently confine light within subwavelength, high-refractive-index semiconductor nanostructures, can enhance and tune light absorption. Reproduced with permission.[149] Copyright 2009, Nature Publishing Group. c) Asymmetric light propagation can be achieved using single semiconductor nanowires with a composition gradient along the length. Reproduced with permission.[151] Copyright 2012, Nature Publishing Group.

4.2 Nanowire Lasers/LEDs

The miniaturization of optoelectronic devices is essential for the continued success of photonic technologies. Nanowires have been identified as potential building blocks that mimic conventional photonic components such as interconnects, waveguides, and optical cavities at the nanoscale. Semiconductor nanowires with high optical gain offer promising solutions for lasers with small footprints and low power consumption.

Since the first demonstration of nanowire lasers in 2001,[152] optically pumped coherent laser emission has been achieved in nanowires. These nanowires act as both waveguides for optical cavities and gain media for light amplification. Most of the nanowire lasers that have been reported were implemented with simple single-nanowire cavities. In these cavities, high optical gain can be obtained because of the large overlap between the photonic mode and the semiconductor gain media. However, low reflectivity at the end-facets (acting as mirrors of the laser cavities) of nanowires induces considerable losses to the cavities, which prevents shorter wires from lasing. There was also some effort toward more efficient lasing cavities such as GaN ring resonators.[153]

Because of the small volume of materials (as little as a few cubic micrometers) used in nanowire lasers, the power required for nanowires to lase is quite low compared to macroscopic lasers. Electrically driven nanowire lasers were reported to reach lasing threshold with just a few microamps current.[154] By placing these nanowires in external cavities such as photonic crystal or distributed Bragg reflectors with high reflectivity, it is likely to be able to further reduce their lasing threshold for even lower power consumption.

Nanowires made of various materials provide opportunities for tunable light emitting devices across the UV, visible and near-infrared spectral regions, including ZnO (385 nm),[152, 155] ZnS (337 nm),[156] GaN (375 nm),[157] CdS (490 nm),[154] GaSb (1550 nm),[158] and others. Assembly of a wide range of efficient direct-gap III-V and II-VI nanowires with silicon nanowires and planar silicon structures has produced multicolor electrically driven nanophotonic and integrated nanoelectronic-photonic systems.[159] Alternatively, multicolor nanowire lasers can also be achieved using multi-quantum well (MQW) nanowire heterostructures, consisting of a GaN NW core that functions as the primary part of the optical cavity, and epitaxial InGaN/GaN MQW shells that serve as the composition tunable gain medium[160]. Optical excitation of individual MQW NW structures yielded lasing with emission engineered from 365 to 494 nm through modulation of quantum well composition (**Figure 11**a).

Compositional tuning of nanowires exhibits increased flexibility compared to bulk materials because their high surface areas assist in strain relaxation, which is particularly important for the growth of nanowires epitaxially on substrates with a large lattice mismatch. Heteroexpitaxial growth of $In_xGa_{1-x}N$ nanowire arrays on c-plane sapphire was achieved using a halide chemical vapor deposition technique.[161] Photoluminescence measurements demonstrated the broadband tunable direct band gap of these InGaN nanowires. NanoLEDs fabricated from nanowires epitaxially on grown p-GaN substrates exhibited electroluminescence ranging from blue to orange, corresponding to an Indium composition from 6 % to 43 % (Figure 11b). Spectral tunability of nanowire lasers has also been demonstrated in organic nanowires.[162] Fluorine-based conjugated polymer nanowires can be synthesized with varying compositions, and thus can provide additional opportunities for continuously tunable laser light.

Although substantial effort has been directed towards controlling their size, shape, and composition, most nanowire lasers currently suffer from emitting at multiple frequencies simultaneously, arising from the longitudinal modes native to simple Fabry-Pérot cavities. As miniaturized lasers are experiencing a rapid increase in applications for digitized communication and signal processing, the monochromaticity of the lasing output becomes an important figure of merit. Laser emission at multiple frequencies can lead to both temporal pulse broadening and false signaling because of group velocity dispersion. These problems can be avoided by controlling the laser to oscillate at a single frequency.

Coupling nanowire cavities is a promising route to produce single-mode operation. Following the Vernier effect, when two sets of Fabry-Pérot modes interact coherently with each other, only the modes that share the same frequencies will be outstanding and observed in the lasing spectra. With properly designed coupled cavities, single frequency lasing can be achieved in optically coupled nanowires. So far, two coupling schemes have been reported in the context of nanowires. By crossing two nanowires or having a single nanowire forming a small loop at on end, single frequency lasing with high suppression ratio (against the neighboring modes) around a wavelength of 738 nm was demonstrated in CdS nanowires (Figure 11c).[163] This form of evanescent wave coupling is highly sensitive to geometric parameters such as inter-nanowire distances, lengths of the coupled segments, and perimeters of the nanowire loops. An alternative photonic architecture to increase the free spectral range is the radiative coupling of two Fabry-Pérot cavities axially through an air gap, known as the cleaved-coupled cavity. Spectral manipulation of lasing modes and lasing operation at a single ultraviolet wavelength at room temperature was achieved by creating cleaved-coupled GaN nanowires – the smallest cleaved-coupled cavities to date (Figure 11d).[164] Besides the reduced number of lasing modes, the cleaved-coupled nanowires also operate with a lower threshold gain than that of the individual component nanowires. A set of numerical methods were developed to verify the operating mechanism of such cleaved-coupled nanowire cavities and provide rational design principles for control of lasing modes in nanowire lasers.

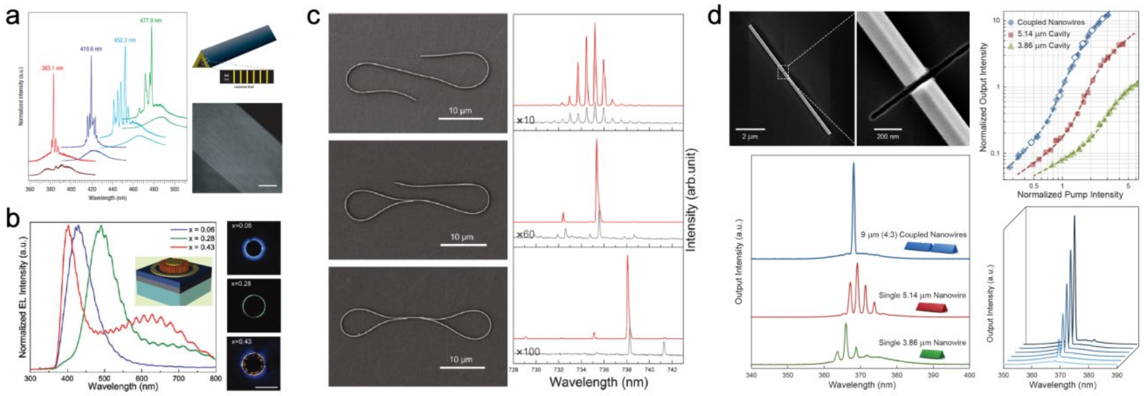

Figure 11. Light emission from nanowires. a) Multi-quantum-well (MQW) core/shell nanowire heterostructures based on well-defined III-nitride materials enable lasing over a broad range of wavelengths at room temperature. Reproduced with permission.[160] Copyright 2008, Nature Publishing Group. b) Wavelength-tunable LEDs were fabricated from $In_xGa_{1-x}N$ nanowires with various indium compositions epitaxially grown on p-GaN(001). Reproduced with permission.[161] Copyright 2011, American Chemical Society. c) A single-mode nanowire laser can be obtained by folding one or two ends of a nanowire into micro loops to form loop mirrors. Reproduced with permission.[163] Copyright 2011, American Chemical Society. d) Versatile manipulation of lasing spectral modes has been theoretically investigated and experimentally demonstrated by creating cleaved-coupled cavities in gallium nitride (GaN) nanowires. Reproduced with permission.[164] Copyright 2013, National Academy of Sciences, USA.

4.3 Nanowire Plasmonics

Miniaturization of semiconductor lasers is critical for the development of chip-integrated photonic and optoelectronic devices. While the use of semiconductor nanowires can reduce the scale of such devices to half of the operating wavelength, they are still subject to the restriction of the diffraction limit. By integrating plasmonic effects, miniaturization of photonic nanowires can be further extended to deep-subwavelength scales beyond the diffraction limit.

Surface plasmons are collective oscillations of electrons on plasmonic metal surfaces, which can guide and manipulate light on scales much smaller than the wavelength. Pure plasmonic waves propagating on metal surfaces typically experience severe Ohmic losses at optical frequencies. Theoretical work, however, predicted that the losses can be significantly reduced with hybrid plasmonic modes forming between a semiconductor nanowire and a plasmonic metal surface, opening the door for the realization for truly nanoscale lasers.[165] The coupling between the plasmonic and photonic waveguide modes across the gap enables energy storage in non-metallic regions and allows plasmonic waves to travel over large distances with strong mode confinement. Using a hybrid plasmonic waveguide consisting of a high-gain CdS nanowire separated from a silver surface by a 5-nm thick insulating (MgF_2) gap, the formation of surface plasmons amplified by stimulated emission of radiation (SPASER) was demonstrated (**Figure 12**a).[166] Since plasmonic modes have no cutoff, downscaling of the lateral dimensions of both the device and the optical mode to deep-subwavelength scales was achieved. The close proximity of the semiconductor and metal interfaces concentrates light into a so-called modal area as small as $\lambda^2/400$. In addition to ultra-small optical mode volumes, the hybrid SPASERs can also operate with smaller physical size than conventional lasers. While CdS nanowires with diameters smaller 150 nm are not able to lase, hybrid plasmonic CdS nanowires as thin as 50 nm can still emit lasing light, although the threshold increases significantly owing to the reduction in the total gain material volume. The successful demonstration of such hybrid SPASERs is also due to a high Purcell factor – a parameter indicating enhanced emission rate – due to strong optical mode confinement. The high Purcell factor not only induces high effective gain in the hybrid waveguide, but also leads to a high spontaneous emission factor (the beta factor, indicating the portion of the spontaneous emission that couples to the lasing mode). With a high Purcell factor and beta factor, smearing of the lasing threshold was observed, which can potentially lead to threshold-less lasers in the future.

Because of the hybrid nature of this semiconductor nanowire-metal thin film structure, not only is the quality of the semiconductor material important, but the plasmonic metal surface also dictates the performance of such SPASERs. It is reported that by making the silver film atomically smooth, InGaN/GaN core-shell nanowires shorter than 500 nm (i.e. requiring larger effective gain to reach the lasing threshold) can also operate as SPASERs (Figure 12b).[167] The epitaxially grown silver film is crucial for reducing the modal volume and plasmonic losses, and therefore allows the hybrid SPASER to be operated under continuous-wave excitation. The impact of plasmonic lasers on optoelectronics integration is potentially significant because the optical fields of these devices rival the smallest commercial transistor gate sizes, and thereby reconcile the length scales of electronics and optics.

The combination of plasmonic resonances and semiconductor nanowires can lead to other exotic effects that give additional functions to traditional optoelectronic devices. With properly designed geometries, nanowire photodetectors covered with plasmonic metals can be “invisible” (low optical scattering) over a broad frequency range (Figure 12c).[168] In these devices, the constituent semiconductors and metals naturally play an electronic (charge extraction) and optical (cloaking) function at the same time and in the same physical space. Demonstration of such invisible photodetectors inspires a bright future, in which the geometry of some of the nanowire devices could be reengineered such that the constituent materials could simultaneously perform valuable electronic and optical functions.

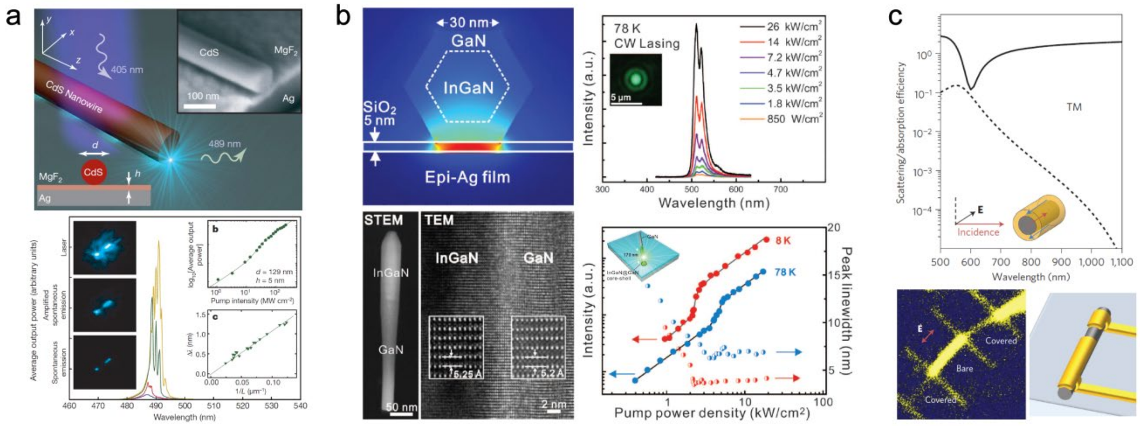

Figure 12. Plasmonic nanowires. a) Nanometer-scale plasmonic lasers were demonstrated with optical modes a hundred times smaller than the diffraction limit. Reproduced with permission.[166] Copyright 2009, Nature Publishing Group. b) A SPASER under CW operation was created using epitaxially grown, atomically smooth Ag films as a scalable plasmonic platform. Reproduced with permission.[167] Copyright 2012, American Academy for the Advancement of Science. c) A photodetector with nanoscale plasmonic electrical contacts has been designed to render the device 'invisible' over a broad frequency range. Reproduced with permission.[168] Copyright 2012, Nature Publishing group.

5. Nanowire Thermoelectrics

Thermoelectric materials can convert thermal energy to electrical energy. This conversion process is reversible, so they can also be used as solid-state coolers. In the presence of a temperature gradient, majority charge carriers diffuse from the hot side to the cold side of the material until an opposing electric field is formed that is sufficient to stop the flow of charge. This open circuit voltage is linearly proportional to the temperature gradient and is determined by a material dependent property is called the Seebeck coefficient (S=dV/dT).

The world uses approximately 500 quads (1 quad = 10^{15} BTU ~10^{18} J) of energy annually. This energy is either used for direct heating or power generation, which typically operates at 30~40% efficiency and loses thermal energy as waste heat to the environment. Thermoelectric modules can potentially utilize a portion of this low-grade waste heat for electricity production, leading to enhanced overall conversion efficiency. Moreover, these stationary solid-state devices are simple and silent compared to other waste heat recovery systems that require moving parts.[169]

The performance of thermoelectric materials is characterized by their dimensionless figure of merit (ZT) as follows:

$$ZT = \frac{S^2\sigma}{k_e + k_{ph}} T$$

where, σ is electrical conductivity and k_e and k_{ph} are electronic and lattice contribution to thermal conductivity. High electrical conductivity, high Seebeck coefficient, and low thermal conductivity are required in order to maximize ZT. While S, σ , and k can be individually tuned by several order of magnitudes, their interdependent nature makes the design of highly efficient thermoelectric materials very challenging. Their relationship can be simplified for degenerate semiconductors and metals by the Mott-Jones relation, assuming a parabolic band model and the energy independent scattering approximation, as follows:[170]

$$S = \frac{8\pi^2 k_B^2}{3eh^2} m^* T \left(\frac{\pi}{3n}\right)^{\frac{2}{3}}$$

where m^* is the carrier effective mass and n is the carrier concentration. Other conventional equations derived by the Boltzmann transport equation and the Fermi-Dirac statistics can be found elsewhere.[171] A high carrier concentration reduces the Seebeck coefficient while it increases the electrical conductivity. A heavy effective mass with flat bands and high density of states (DOS) is beneficial for the Seebeck coefficient, but it decreases the mobility and electrical conductivity. The thermal conductivity is also coupled with electrical conductivity; $k = k_e + k_{ph}$.

Even though thermal energy is mainly conducted by phonons, the contribution of electrons in degenerate semiconductors and metals becomes significant.

Since Bi_2Te_3 and its alloys were discovered to have ZT ~ 1 at room temperature in 1950s, it has been very challenging to increase ZT to values greater than 1.[172] The conversion efficiency of thermoelectric generators is calculated by:

$$\eta = \eta_c \frac{\sqrt{1+ZT}-1}{\sqrt{1+ZT}+T_c/T_h}$$

where η_c is the Carnot efficiency and T_c and T_h are the temperature of the cold and hot sides, respectively. Accordingly, $ZT > 3$ is often targeted for the solid state thermoelectric generators in order to compete with conventional heat engines. Existing approaches such as heavy element alloying or point defect/interface engineering are promising but have not reached $ZT > 3$ yet.[173]

The nanowire geometry has two main potential advantages for thermoelectrics. First, the power factor in quantum wires can be increased due to band structure modification. Second, strong phonon boundary scattering can effectively reduce the thermal conductivity compared to bulk materials. In 1993, Hicks and Dresselhaus predicted that an electronic band structure tuned by quantum confinement effects in nanostructures should increase the power factor ($S^2\sigma T$) for quantum wires or quantum well structures dramatically. For example ZT =14 was predicted for Bi_2Te_3 quantum wires.[174] The sharp increase in the DOS near the Fermi level in a 1-D structure may enhance the electrical conductivity and the 'asymmetry' of its band structure and may also lead to a larger Seebeck coefficient.[171] Power factor enhancement was experimentally achieved by introducing resonant states or high valley degeneracy in electronic bands for bulk, but these approaches have not been applied to nanowire structures to our knowledge.[175]

Significant research effort has been performed at the single nanowire level to characterize their fundamental thermoelectric properties. The measurement of the electrical conductivity and

Seebeck coefficient of single nanowires is relatively common and can be measured by conventional photolithography techniques including 4-point probe electrodes, which also work as thermometers to sense the local temperature along the nanowires for the Seebeck coefficient measurement. The thermal conductivity measurement, however, is more complicated because only the heat conduction through the nanowire should be probed without parasitic environmental heat convection or radiation.[176] To address this, two suspended membranes with metal thermometers are thermally isolated and bridged by a nanowire, which provides the only heat channel between them. As one side is heated, heat is conducted through the nanowire from one side to the other, and temperature is simultaneously measured to calculate thermal conductance. However, as thermal contact resistance between the nanowire and the membrane is unknown, the thermal resistance of nanowires has to be carefully chosen to minimize the contact resistance.

Experimentally, much effort to synthesize Bi/Pb chalcogenide nanowires has been performed due to their promising ZT values in the bulk materials. The thermoelectric properties of Bi-Te nanowires or nanotubes have been measured by various groups.[177] Mavrokefalos *et al*. and Zhou *et al*. measured thermoelectric properties of electrodeposited Bi_xTe_{1-x} nanowires but did not observe a clear improvement.[177a, 177b] Zhang *et al.*, and Zhao et al, however, independently investigated the thermoelectric performance of Bi_2Te_3 nanocomposites compressed from Bi_2Te_3 nanowires and nanotubes, respectively, and reported ZT ~ 1 at 380K and 450K, respectively.[177e, 177h] Pb chalcogenide materials have a low thermal conductivity of ~1.7W/mK in the bulk, which is reported to be even lower in nanowires due to enhanced phonon boundary scattering.[178] Roh et al. and Liang et al. synthesized PbTe and PbSe nanowires by vapor phase methods, which demonstrated suppressed thermal conductivity down to 1.29 W/m-K and 0.8W/m-K for PbTe and PbSe, respectively.[178a, 178c] It became clear from these single nanowire studies that although enhanced phonon boundary scattering lowers the thermal conductivity of these chalcogenide nanowires, their poor electrical properties led to ZT values lower than the bulk materials, possibly due to defects or non-optimized doping conditions. Liang *et al*. demonstrated that a field effect can modify the position of the Fermi level and tune the Seebeck coefficient of PbSe nanowires and Si/Ge nanowires.[178d, 179] This approach may be useful particularly when nanowires are hard to dope or the impurity scattering by dopants needs to be minimized.[179]

Mingo predicted that thin III-V and II-IV nanowires may be promising thermoelectric materials as well.[180] Among these candidate materials, the predicted *ZT* of 10nm thick InSb nanowires was calculated to be ~6. Despite this high *ZT* prediction, the *ZT* value of InSb nanowires was measured to be only 0.01 at 400K, which may be attributed to the loss of In during the growth and the formation of Sb-doped InSb instead.[181] Andrews *et al*, investigated thermoelectric properties of $In_{2-x}Ga_xO_3(ZnO)_n$ (IGZO) nanowires.[182] These superlattice nanowires contain periodic InO_2^- layers with a uniform Ga distribution along the ZnO nanowires (**Figure 13**). This unique polytypoid structure demonstrated an improved power factor and thermal conductivity, resulting in a 2.5 orders of magnitude higher *ZT* value than ZnO nanowires at room temperature. The authors attributed the suppressed thermal conductivity and higher power factor to enhanced phonon scattering and cold electron filtering by the periodic inclusion layer or quantum confinement by the superlattice structure.

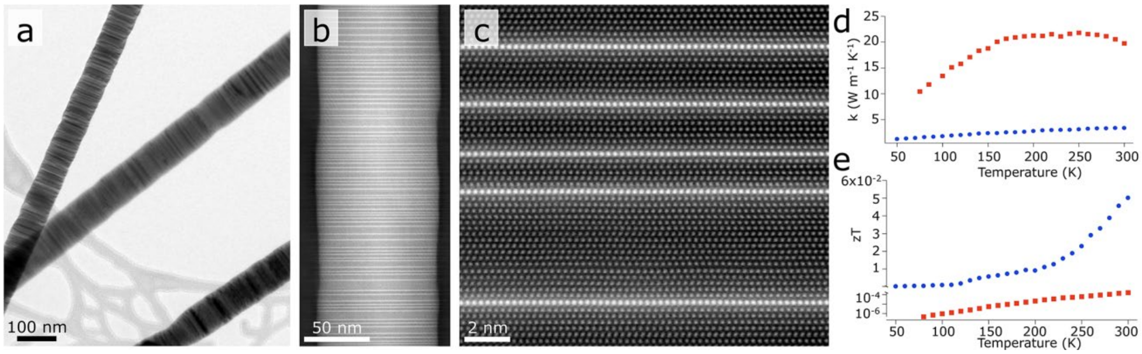

Figure 13. a) TEM image of multiple $In_{2-x}Ga_xO_3(ZnO)_n$ nanowires. b) Z-contrast STEM image of an IGZO nanowire, showing indium inclusion layers oriented perpendicular to the nanowire growth direction. c) HRSTEM image of an IGZO nanowire revealing inclusion layers (MO_2^- , M=In or G) at an atomic level. d) Variation in thermal conductivity with temperature for an IGZO nanowire (blue) and a ZnO nanowire (Red). Interface - phonon scattering in IGZO nanowires suppressed thermal conductivity compared to intrinsic ZnO nanowires. e) An enhancement of 2.5 orders of magnitude in figure of merit was observed for IGZO nanowires compared to ZnO nanowires. Reproduced with permission.[182] Copyright 2011, Royal Society of Chemistry.

While the successful enhancement of power factor in nanowires has been limited, it is quite clear that the thermal conductivity generally decreases via enhanced phonon boundary scattering. The thermal conductivity of solid state materials is given by:

$$k = \int \frac{C(w)v(w)l(w)}{3} dw$$

where *w* is phonon frequency, *C(w)* is frequency-dependent heat capacity, *v(w)* is group velocity, and *l(w)* is mean free path (mfp) of phonons. Unlike electrons, the wavelengths of heat carrying phonons in solids are spectrally broad, while the mfp of phonons ranges from roughly 10nm ~ 10μm due to their frequency dependent relaxation rate. A recent first principles calculation revealed that approximately 90% of heat conduction is conducted by phonons with a mfp of 40nm – 10μm in bulk silicon.[183] Due to this relatively longer *mfp*, bulk silicon is one of the most thermally conductive materials, with a conductivity of ~150 W/mK at room temperature.

In fact, the power factor of optimally doped silicon is comparable to that of optimally doped Bi_2Te_3. Furthermore, since the bandgap of Si (1.1 eV) is much higher than that of Bi_2Te_3, the power factor does not drop at high temperatures. Li *et al*. demonstrated that silicon NWs have a much lower thermal conductivity than the bulk, and the clear diameter dependence of thermal conductivity observed indicates that surface boundary-phonon scattering is highly diffusive (~38 W/mK, 27 W/mK, and 18 W/mK for 115 nm, 56 nm, and 37 nm nanowires, respectively).[184] In 2008, Hochbaum et al. measured a *ZT* value of rough silicon nanowires of 0.6 at room temperature, which is ~ two orders of magnitude higher than that of the bulk. The rough silicon nanowires were prepared via an electroless etching method (EE).[185] Typically, silver nanoparticles form mesh-like structures on silicon wafers and catalyze the etching of silicon lattices vertically, leaving high aspect ratio silicon nanowires.[186] These nanowires have rough surfaces and show an order of magnitude lower thermal conductivity than that of smooth vapor-liquid-solid (VLS) nanowires at the similar diameter. Since the phonon scattering at the smooth surfaces of VLS nanowires is known to be very diffusive (close to the Casimir limit), conventional models could not explain this greatly enhanced boundary scattering, which leads to sub-diffusive phonon transport.[187] A number of research groups proposed models to explain these phenomena, but their validity is still a matter of debate.[188] For example, Martin *et al.* employed the Born approximation toward phonon scattering and assumed that the surface roughness alters the phonon dispersion.[188b] Carrete and Mingo *et al.*, however, argued that the Born approximation is invalid at phonon wavelengths similar to the size of the scattering medium.[188f] This warrants an experimental analysis of the impact of surface roughness on phonon scattering.[189] Although the dominant wavelength of phonons at room temperature is ~ 1nm, the wavelength of phonons which actually contribute to heat conduction is much broader (1 – 100nm), and surface roughness at this characteristic length scale suppresses phonon transport and lattice thermal conductivity.[183a] The degree of roughness is typically characterized by the root-mean-square (rms) value for amplitude and correlation length for the lateral scale of roughness. Thermal conductivity is correlated with these two traditional parameters independently, but the spectral roughness factor at the phonon characteristic length scale determines the thermal conductivity more strongly (**Figure 14**).[189a] Recently, the thermal conductivity of rough nanowires with short correlation lengths (5 ~ 10nm) was measured at low temperature, 10K – 60K where surface boundary scattering is prominent. The agreement with multiple scattering theory supports sub-diffusive behavior.[188g, 190] Boukai *et al*. demonstrated that thin silicon nanowires (10 – 20nm) prepared by superlattice nanowire pattern transfer (SNAP) also have high thermoelectric properties with a maximum ZT of 1.0 at 200K due to an enhanced Seebeck coefficient.[191] The authors explain that the thin nanowire geometry confines phonons, which enhances the Seebeck coefficient via phonon drag.

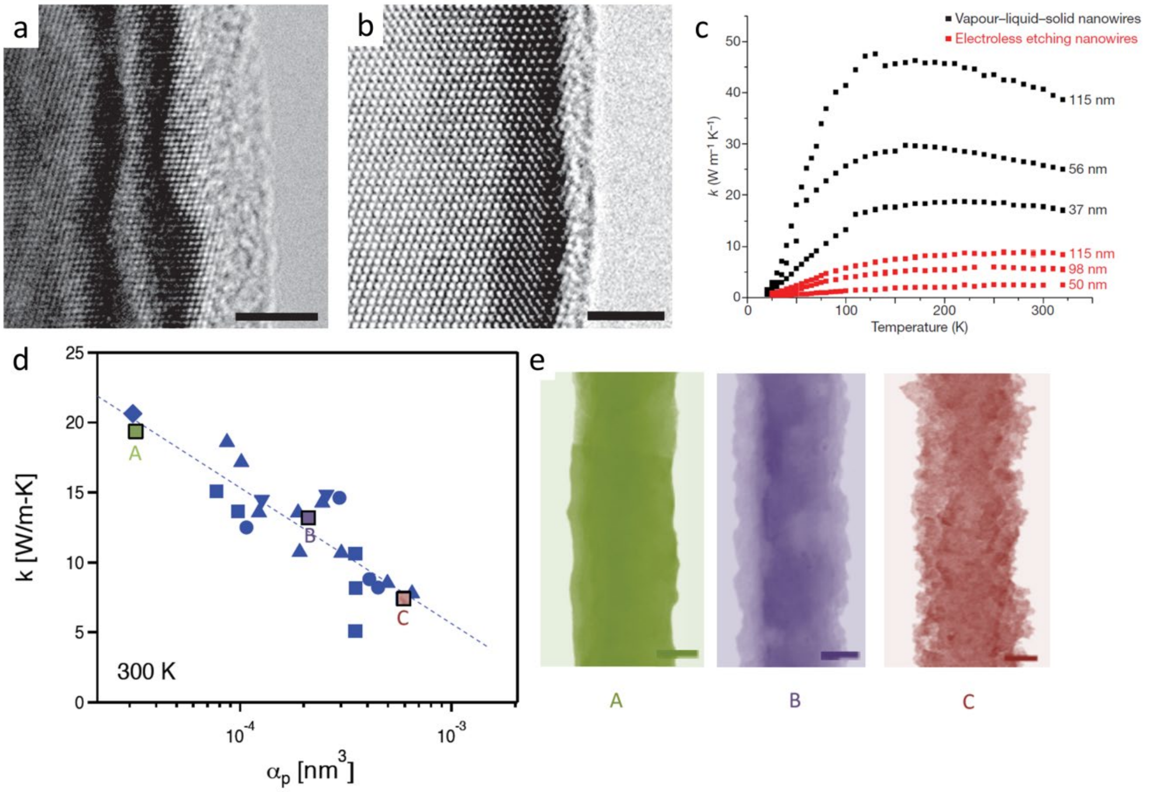

Figure 14. Rough silicon nanowires and their thermal conductivity. a,b) TEM images of an EE wire and a VLS wire, respectively. c) Temperature-dependent thermal conductivity of EE wires

and VLS wires. EE wires exhibit suppressed thermal conductivity for their diameter. Reproduced with permission.[185] Copyright 2008, Nature Publishing Group. d) Thermal conductivity at 300K correlated to the spectral surface roughness factor, α_p. Roughness increases from A < B < C. Reproduced with permission.[189a] Copyright 2012, American Chemical Society.

Bulk Si-Ge alloy and metal silicides have also been considered promising thermoelectric materials. Bulk Si-Ge alloy is used in radioisotope thermoelectric generators (RTG) in remote unmanned space flights due to a high *ZT* value at elevated temperatures (1100 K). According to Rayleigh scattering theory, atomic scale defects in Si-Ge alloy systems scatter short wavelength phonons effectively, while long wavelength phonons remain affected. In Si-Ge alloy nanowires, long wavelength phonons scatter at the nanowire boundaries in addition to alloy scattering, which effectively decreases the thermal conductivity.[192] A recent report demonstrated that these long wavelength phonons could propagate up to 8um by ballistic conduction in SiGe nanowires.[192e] Lee *et al.* has simultaneously measured both the electrical and thermal properties of individual Si-Ge alloy nanowires and reported a *ZT* value of ~ 0.46 at 450K, and predicted a theoretical value of 2 at 800K.[192d] Metal silicide nanowires have also been fabricated and tested. The ZT value of Cr_2Si nanowires synthesized by chemical vapor transport was measured to be ~0.07 at 320K without quantum confinement effects present.[193]

In summary, even though nanowires possess theoretical advantages for thermoelectric applications, including quantum confinement effects and phonon boundary scattering, synthetic challenges still limit the figure of merit, which remains inferior to bulk counterparts. Improved control of crystallinity, defects, and dopants is still required to improve nanowire power factors, especially for thinner wires. However, it has been shown that thermal conductivity can be suppressed in various nanowire structures, including rough silicon nanowires. Although the underlying mechanism of surface roughness on phonon scattering is not clearly understood, it represents a potential advantage of the nanowire geometry and will be an important consideration when designing improved nanowire thermoelectric devices in the future.

6. Nanowire Photovoltaics

The unique properties of semiconductor nanowires make them promising candidates for efficient and inexpensive solar cells. Nanowire array solar cells are the natural heir to second-generation thin-film photovoltaics (PV) for reducing processing costs while maintaining practical efficiencies. The potential of nanowires lies primarily in their tunable geometric effects rather than in any new physical phenomena, as is the case for third-generation quantum-dot solar cells. Nanowire solar cells typically use large nanowires that are well beyond quantum confinement effects so that conventional semiconductor physics applies. The main difference from bulk or thin-film devices is their much larger surface-to-volume ratio, with roughness factors up to ~300. Also, the dimensions of nanowires are on the same scale as the wavelength of visible light and the minority carrier diffusion lengths in many solar materials. Because of this geometrical coincidence, nanowires offer unique opportunities for improving light absorption and charge collection in solar cells. They are also attractive because of their potential for integration into flexible devices and for inexpensive, low-temperature processing.

Research into nanowire PV focuses on both nanowire array solar cells as well as single-nanowire devices. Single-nanowire solar cells provide fundamental information about the optical and electronic properties of the solar cell's materials and the quality of its charge-separating junction. To produce practical amounts of power, however, large-area solar cells must consist of nanowires wired in parallel, which is most easily realized by nanowire array solar cells. Efficiency comparisons between thin-film and nanowire PV are best made using nanowire array solar cells because only arrays can produce amounts of power comparable to those produced by conventional PV. Also, since single-nanowire solar cells are typically smaller in diameter than the wavelength of light in the visible spectrum, their absorption cross-section can exceed their geometrical cross-sectional area, which increases their apparent efficiency;[194] however, such concentrating effects are not directly relevant in large-area solar cells because their efficiency is normalized to the total area of the array, not to the area of active material.

One of the earliest-recognized advantages of nanowires is their potential for improved separation and collection of photogenerated charges. Radial p-n junctions orthogonalize the directions for absorption of light and separation of charges: absorption occurs along the long axis of the wire, while the photogenerated minority carriers must travel only the radial distance to be separated and collected (**Figure 15**). This geometry is most beneficial in materials whose optical absorption length is much longer than their minority carrier diffusion length; consequently, nanowire solar cells can be made from materials that are unsuitable for planar thin-film solar cells because the core-shell geometry relaxes the requirements on minority carrier diffusion length.[195] Also, less expensive and lower purity materials can be used. Interesting candidates include sulfides,[51b] oxides,[196] and low-purity[197] or heavily doped silicon,[198] which exhibit acceptable light absorption but low minority carrier diffusion lengths. This concept has even been applied to dye-sensitized solar cells[199] and semiconductor-organic hybrid solar cells[200] to improve charge collection from the dye or low-mobility organic phase.

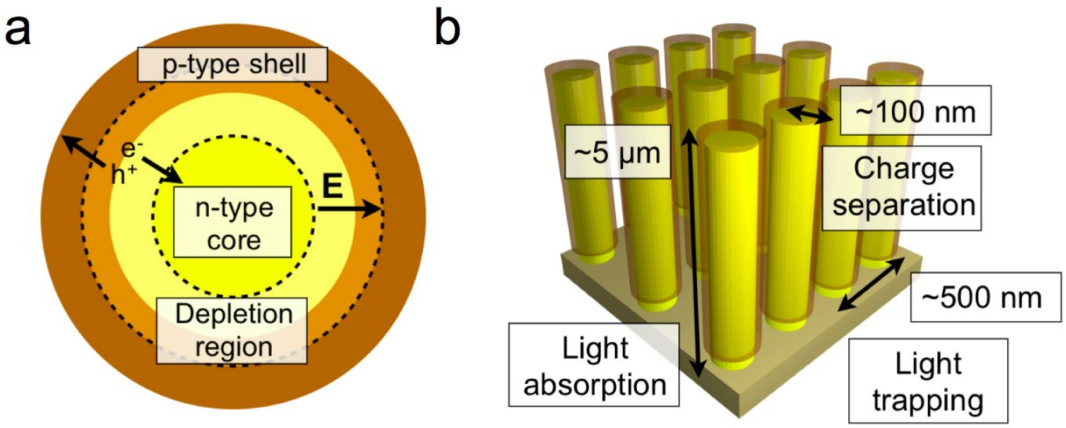

Figure 15. The geometry of nanowire solar cells. a) Diagram of a radial core-shell nanowire solar cell showing the depletion region's built-in electric field that separates charges between an n-type core and p-type shell. b) Schematic of the length scales that improve light absorption and charge separation in nanowire array solar cells.

Radial p-n junctions offer many opportunities for improved solar cells, but they also introduce additional challenges that must be overcome to realize their benefits. Because of their small size, the core or shell of a nanowire with low carrier concentration can be easily depleted of its carriers at a p-n junction if the junction's other side is more heavily doped. Fully depleting half the junction leads to lower built-in voltage and higher series resistance through the depleted semiconductor, both of which degrade the solar cell's efficiency. For this reason, the core and shell doping levels must be carefully controlled in nanowire solar cells to ensure their performance.[196, 201] Also, although radial p-n junctions can be somewhat less sensitive to high surface recombination velocities than their planar counterparts, they are highly sensitive to depletion-region recombination.[195, 202] Recent experimental work indicates that the quality of the junction is critically important to the efficiency of nanowire solar cells because of their large junction area and depletion volume. Silicon nanowire solar cells illustrate this point in that they have shown much improvement in their open-circuit voltage (V_{oc}) and fill factor (FF) with the creation of a p-i-n structure and improved junction quality. Initial results in 2007 yielded p-i-n nanowire solar cells with V_{oc} of 260 mV and FF of 55%,[203] but by 2012, these values had increased to as high as 500 mV and 73% through better control of the crystallinity of the shell and the doping structure of the homojunction (**Figure 16**a,b).[194a] The V_{oc} and FF of even these best silicon nanowire solar cells, however, still fall short of those of planar crystalline silicon PV, whose record values are 706 mV and 83%.[204] Examples of single-nanowire solar cells in other materials include those produced from GaAs,[194b, 205] GaAsP,[206] and the GaN/$In_xGa_{1-x}N$ system,[207] but their junction quality, as indicated by their V_{oc} and FF, still lags behind planar benchmarks for these material systems. In stark contrast to these systems, CdS-Cu_2S nanowire solar cells exhibit V_{oc} and FF that slightly exceed those of their planar counterparts, likely because of their high-quality heteroepitaxial junction (Figure 16c,d).[51b] Both the experimental and theoretical literature to date indicate that extremely high quality junctions with very low dark current are necessary to produce nanowire solar cells with reasonable V_{oc} and FF, and therefore efficiency.

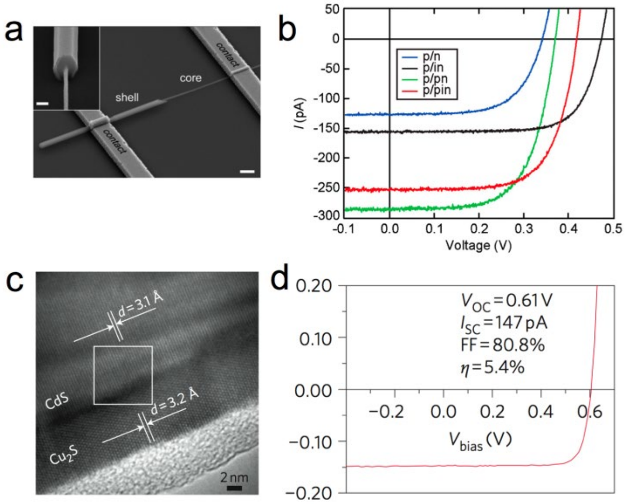

Figure 16. Single-nanowire solar cells. a) SEM of a single-nanowire silicon solar cell. b) The V_{oc} and FF values of these silicon single-nanowire solar cells are strongly influenced by the growth process of the junction. Reproduced with permission.[194a] Copyright 2012, National Academy of Sciences, USA. b) High-resolution TEM of the heteroepitaxial junction in a CdS-Cu_2S nanowire solar cell. c) *I-V* curve of the CdS-Cu_2S nanowire solar cell with a V_{oc} and FF that are records for this material system. Reproduced with permission.[51b] Copyright 2011, Nature Publishing Group.

Although single-nanowire solar cells are appropriate to study the quality of the charge-separating junction, one key challenge inherent to charge collection within the nanowire array geometry is its dilution of photo-generated carriers across a larger interface, resulting in lower V_{oc} as compared to planar solar cells.[194a] This effect is analogous to a planar cell with the equivalent junction area operating in lower light conditions and suggests that nanowires might be most efficient as concentrator solar cells. Fortunately, the nanowire geometry itself can create such concentration effects because of its unique optical properties.

Films of nanowires exhibit light-trapping effects that arise from the microscopic arrangement of the nanowires. Because of these effects, a film of nanowires absorbs more light than a thin film made from the equivalent volume of material would absorb. Part of this increase comes from nanowires' anti-reflection properties, which can be understood as grading the refractive index difference between air and the material of the nanowire;[208] however, within a nanowire film, scattering from the many air-semiconductor interfaces traps light and leads to increased absorption in the nanowires. The record nanowire solar cell, made from InP nanowires with axial p-i-n junctions (**Figure 17**), is a clear example of this phenomenon: its nanowires cover only 12% of the area of the cell, yet they produce 83% of the short-circuit current (J_{sc}) of the best InP planar cells.[209] While light-trapping effects are present in even random arrays of wires, it is theorized that carefully engineered nanowire arrays can exceed the light trapping generated by a randomly textured film[210] and produce a nanowire solar cell whose efficiency exceeds that of its planar counterpart.[211] Much experimental work has demonstrated increased absorption within nanowire and microwire films,[209, 212] yet definitive proof of exceeding the limit of random light trapping is still lacking.

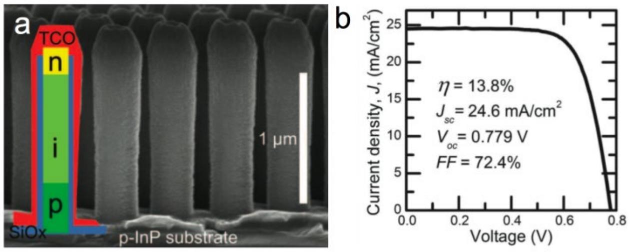

Figure 17. Nanowire array solar cells. a) Diagram and SEM of the record InP axial p-i-n nanowire array solar cell and its *J-V* characteristic in b). Reproduced with permission.[209] Copyright 2013, American Academy for the Advancement of Science.

Individual nanowires also exhibit a form of light trapping because their subwavelength dimensions give them optical resonances in the visible region of the spectrum. The electromagnetic modes of a dielectric cylinder can be either bound, waveguiding modes or leaky modes, as denoted by either a real or complex propagation constant, respectively.[213] When light hits a wire, bound modes guide light along the axis of the cylinder, yielding increased absorption within the nanowire.[194b, 214] Leaky modes, so named because they allow energy to radiate or "leak" from the system, also confine light within the semiconductor and lead to increased absorption at their resonance wavelength.[149, 215] These resonances essentially concentrate light within the nanowire, making its absorption cross-section at a resonance wavelength much larger than its geometrical cross-section. Numerical electromagnetic simulations can be used to predict such enhancements in absorption and are in agreement with experimental results.[194a] Because these resonances are excitations of a single nanowire, however, taking advantage of them to improve the efficiency of an array device implies sparse coverage of a substrate with nanowires, since dense films would make the concentrating effect unnecessary. In this case, since nanowire solar cells operate more efficiently under concentrated light, an array device might achieve greater efficiency by concentrating light into a few nanowires rather than harvesting dilute light over a dense array of many nanowires.[194b, 211b] To achieve such an optimal architecture would require predicting the diameter and pitch of the nanowire array necessary to create sufficient concentration of light within the nanowires. Numerical electromagnetic simulations will therefore continue to play a key role in optimizing the design of nanowire PV. The next step, which is increasingly common in the literature of thin-film PV, will be to integrate electromagnetic simulations with simulations of the device physics to understand and optimize where charges are generated and collected within the nanowire solar cell.[201]

For a solar technology to be truly relevant, not only must the efficiency be high, but also the cost of implementation must be low. The extensive literature on low-temperature, solution-based, and scalable syntheses of nanowires suggests that nanowire solar cells will ultimately be less expensive to produce than their thin-film counterparts. Nanowires' unique optical and transport properties will allow less actual material to be used in a solar cell to achieve similar efficiencies,[209, 211a] and single-crystalline nanowires can be grown at low temperatures (200-500°C), comparable to thin-film processing temperatures. Also, like organic solar cells and some thin-film PV, nanowire array solar cells can be produced using lightweight, flexible substrates that will make them less expensive to install than current technology and suitable for mobile applications.[216]

The field of nanowire photovoltaics has made much progress in understanding how the nanowire geometry can be leveraged for improved performance. Applying this knowledge to develop large-area solar cells, however, will take a combined effort. Chemists and material scientists continue to develop new nanowire syntheses, yet they must work closely with device physicists to ensure that the properties of their nanowires are suitable for PV applications, particularly for solution-synthesized nanowires. Currently, their conductivity and optical quality often lag behind those of nanowires grown at high temperature in vapor-phase syntheses. Also, creating high-quality junctions and interfaces for charge separation and collection is essential, and much fundamental science in this area still remains to be explored. By combining synthetic control of nanowires' material, size, doping, and junctions with electromagnetic and device simulations, it will be possible to optimize large-scale array solar cells to yield efficiencies comparable to those of current thin-film technology. As materials and designs become more mature, the final step will be integrating these solar cells into inexpensive, flexible substrates to realize the full potential of nanowire PV.

7. Nanowires for Artificial Photosynthesis

In addition to photovoltaics, which convert solar energy into electricity, a pathway to capture solar energy and directly convert it into chemical fuels is also desirable for energy storage and transportation applications. Typical chemical reactions that produce fuels include splitting water into H_2 and O_2 and reducing carbon dioxide into organic molecules. This solar-to-fuel process, termed artificial photosynthesis,[217] mimics natural photosynthesis and is an alternative approach to photovoltaic cells for production of carbon-neutral energy from sunlight. Recent advances in scientific research have yielded rich knowledge in this area, yet challenges remain[218]. By taking advantage of nanowire materials, it is possible that these challenges can be overcome and that large-scale implementation of solar-to-fuel energy conversion is on the horizon[219].

Although the solar-to-fuel conversion process shares several similarities with photovoltaics, direct production of fuels from sunlight is more flexible in some aspects, while is more restricted in others. Both processes require light absorption and charge separation in semiconductors that exhibit band-bending at a junction[220]. However, because solar-to-fuel conversion typically requires a liquid electrolyte to facilitate the electrochemical reactions[221], band-bending can be caused by either semiconductor/electrolyte interfaces[220, 222] or embedded solid junctions[223]. Additionally, since the photoexcited carriers need to cross the solid/electrolyte interface for photoelectrochemical reactions to occur, the materials used should be stable in the electrolyte under illumination, and the surface states at the interfaces should be engineered to alleviate detrimental effects such as surface recombination[224] and Fermi-level pinning[225]. Moreover, unlike photovoltaics, which aim to maximize power output, producing fuels from sunlight requires a minimum voltage output that is imposed by the chemical reaction involved. For example, at standard conditions, splitting water into hydrogen and oxygen requires at least 1.23V. Additionally, electrochemical overpotentials need to be overcome to facilitate a high reaction rate. This voltage restriction limits the choice of materials. If only one light-absorber is applied, a large band gap semiconductor is required. To achieve high efficiency, it is more desirable to use two light-absorbers with smaller band gaps to provide the necessary voltage for the electrochemical reaction.[226] Under this biomimetic "Z-scheme",[227] one semiconductor acts as a photocathode for reduction, while the other acts as a photoanode for oxidation. In these electrodes photo-excited minority carriers move to the solution to power the reaction, while majority carriers recombine at the interface connecting the light absorbers. Discounting stability requirements, the full arsenal of small band gap materials developed in photovoltaic research could potentially be applied, making the "Z-scheme" one of the most promising directions for solar-to-fuel conversion.

The application of nanowire materials presents new possibilities to address the issues mentioned above. The introduction of a nanowire morphology with a large surface area could reduce the electrochemical overpotential required[219a]. For nanowire photoelectrodes there are additional benefits, including enhanced light absorption and improved charge collection, as described in the photovoltaics section. Generating a core-shell nanowire heterostructure could further exploit these advantages by assigning a specific function to each material component. For optimized performance, careful structural and material design is needed, along with fundamental insight into the interplay among the various components. Despite the intensive research on nanowire photoelectrodes for half-reactions, demonstration of spontaneous solar-to-fuel processes based on nanowires is still in its infancy and many opportunities exist.

First, let us consider the general benefits that a nanowire morphology could introduce. The small feature size of nanowires provides a large surface area at the solid/electrolyte interface, similar to other nanomaterials. Because solar-to-fuel conversion requires a chemical reaction at the interface, the nanowire structure could lower the electrochemical overpotential[222], which is partially determined by the kinetic barrier for the chemical reaction. This facilitates reactions that are kinetically slow[228], and reduces the required use of noble-metal electrocatalysts[229] or allows the use of less active earth-abundant ones[230]. For example, a quantitative exploration of the lower limits of Pt catalyst loading on Si nanowire photocathodes demonstrated that a uniform surface coating of ~13 ng/cm^2 was sufficient for efficient photoelectrochemical proton reduction[229]. Moreover, for the "Z-scheme", which uses a separate photocathode and photoanode, nanowire photoelectrodes are advantageous for charge collection. Particularly for semiconductors with indirect band gaps, the nanowire morphology orthogonalizes the directions of charge collection and light absorption[195, 222, 231], enhancing the quantum efficiency. An equivalent circuit for a photoelectrochemical cell can be considered in which the junction functions as a diode, the electrochemical charge transfer behaves as series resistor, while the recombination of photo-generated carriers acts as a shunt resistor.

Accordingly, the nanowire morphology could also increase the fill factor of the photocurrent curve by decreasing the charge-transfer resistance, allowing for more chemicals to be produced without increasing the voltage supply. In the literature, usually both a reduced overpotential and more efficient charge collection are cited for nanowires, and the observed performance enhancement is a synergic effect (**Figure 18**a). Additionally, a similar light trapping benefits to those in nanowire photovoltaics can be observed. Because the diameter and spacing of the nanowires is on the same length scale as the wavelength of visible light, strong light-trapping effects take place and promote absorption within the semiconductor even though much less material is used[212a, 212b], including direct band gap semiconductors such as GaAs[232]. This effect reduces the material cost input for the device, which is important for commercial applications.

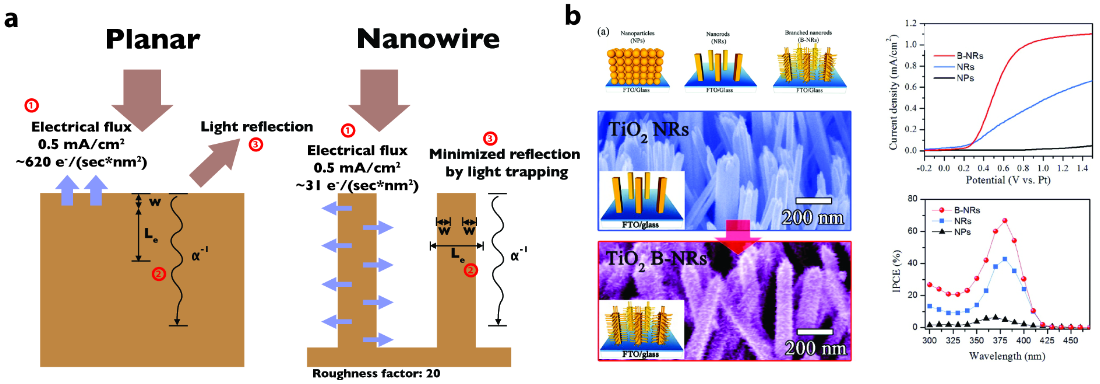

Figure 18. a) Schematic of the comparison between planar and nanowire photoelectrodes. The numbers denote three major advantages of nanowires for solar-to-fuel conversion. b) A TiO_2 nanowire photoanode was used as an example for comparison of various morphologies. NPs: nanoparticle film electrode, NRs: nanorod electrode, B-NRs: branched nanowire electrode. Reproduced with permission.[228] Copyright 2011, American Chemical Society.

To elucidate the advantages listed above, we consider a TiO_2 photoanode as an example. Water oxidation at the photoanode is generally sluggish because it requires the transfer of four electrons[221], and the mobility of photo-generated holes in TiO_2 is relatively low[233]. By using TiO_2 nanowires[42b], the performance is significantly improved[228, 234]. As compared with a film of nanoparticles as a photoanode, the nanowire electrode has better absorption and charge collection and consequently much larger photocurrent (Figure 18b)[228]. Moreover, when creating a nanowire-based branched structure for larger surface area, the saturation photocurrent and fill factor further increase[228]. These results indicate enhanced charge collection, as well as reduced series resistance from the electrochemical reaction. A similar demonstration of one-dimensional nanostructures has been reported in several material systems, including hematite (α-Fe_2O_3)[235], ZnO[236], WO_3[237] , GaAs[232], GaP[35, 238], GaN[239], and Si[240]. It is evident that the wire morphology is a general strategy to use less material and improve performance for photoelectrodes.

One extension of this geometry is the use of core-shell nanowire photoelectrodes[241]. Although single-composition nanowire electrodes improve charge separation within the band-bending region, charge transport through the electrode may still be hindered by the large resistivity of the bulk material in the core of the nanowire. A core-shell configuration can alleviate this issue, by designing a photoactive shell for charge separation and a conductive core specialized for charge collection. Additionally, the heterojunction between the two materials may provide extra photovoltage for the device[241a, 242]. Photoelectrochemical characterization of core-shell nanowire photoelectrodes was first reported on the combination of Si/TiO_2 with enhanced photoanode performance (**Figure 19**a)[241a]. In this case TiO_2 is the shell material for water oxidation, and Si is the core material for charge transport. Also it was found that a p-type Si core experiences downward band-bending and creates a more anodic onset voltage for photocurrent, while a junction between n-type Si and TiO_2 induces upward band-bending in the Si and shifts the photocurrent curve cathodically. This demonstrates that the photocurrent performance of TiO_2 can be modified by the band alignment with the core material. Subsequent reports have applied this idea to other material combinations. Silicon has been used as the core material for

Si/TiO_2[241a, 243], Si/Fe_2O_3[242] (Figure 19b), Si/WO_3[244], and $Si/In_xGa_{1-x}N$[245], owing to its good conductivity, tunable doping, and desirable stability. Metal silicides, titanium silicide (TiSi) in particular, have also been chosen as the core material for their good conductivity to realize $TiSi/TiO_2$[246], $TiSi/WO_3$[247], and $TiSi/Fe_2O_3$[248] photoanodes via atomic layer deposition. The optical properties of metal silicide NW arrays have been shown to exhibit highly efficient light-trapping properties to minimize reflection and enhance absorption, providing a highly conductive template for coating with a thin absorbing material[249]. WO_3 has also been reported as a core material in combination with $BiVO_4$[250], not only for the good conductivity of WO_3 but also for its desirable band-bending at the heterojunction, which enhances charge separation.

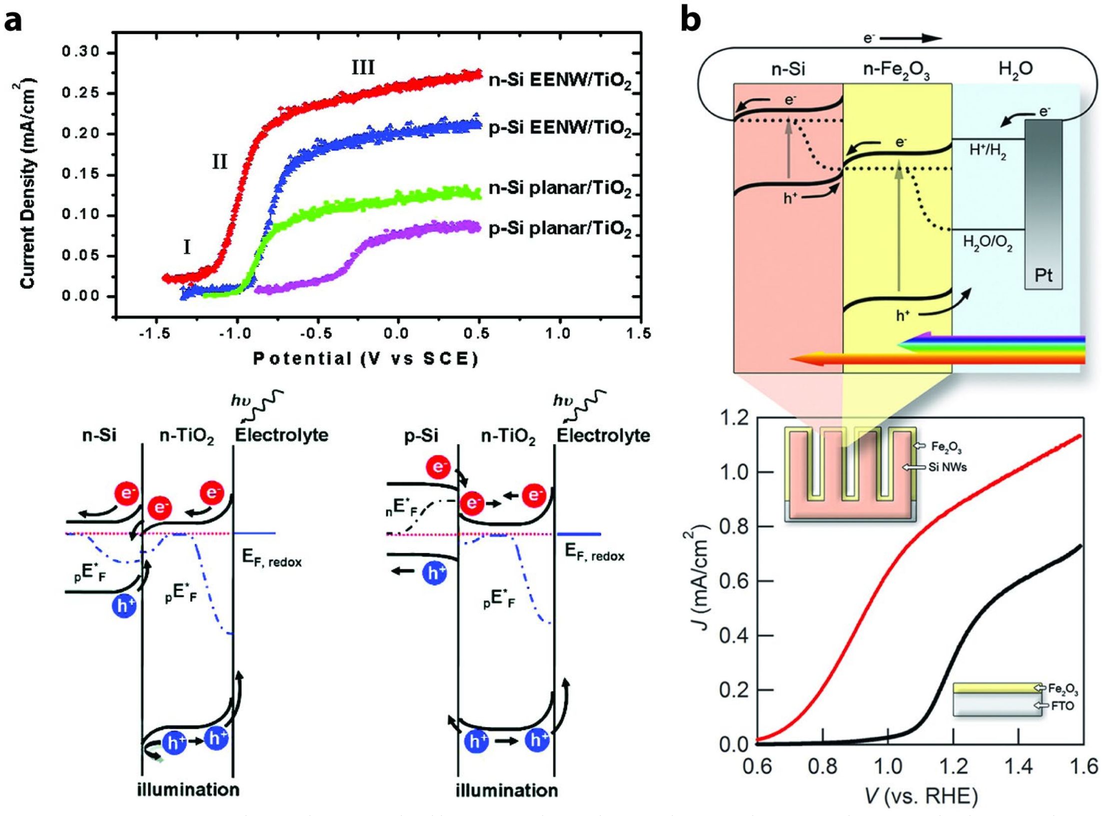

Figure 19. Examples of core-shell nanowire photoelectrodes. Owing to their good conductivity and tunable electrical properties, Si nanowire arrays were chosen not only to improve charge collection but also to provide extra photovoltage in the combination of a) Si/TiO_2 and b) Si/Fe_2O_3. The band bending in both material combinations provides additional photovoltage for water oxidation. Panel (a) reproduced with permission[241a]. Copyright 2008, American

Chemical Society. Panel (b) reproduced with permission.[248] Copyright 2011, American Chemical Society.

In spite of these potential benefits, the nanowire morphology is not a panacea. Nanowires present new opportunities, but careful design of their electrodes should be ensured. First of all, the diameter, doping level, and tapering of the nanowires should all be considered[231, 251], and the effect of surface states should be understood at least qualitatively, for example via electrochemical impedance spectroscopy[240f, 252]. It has been shown that without these considerations, a nanowire electrode may not yield any gain in performance over a planar electrode[231, 252a]. Second, even though a nanowire morphology helps charge separation, the material properties, for example the life-time of photo-excited carriers, are still very important. Good material quality ensures a better starting point when applying a nanowire morphology[245]. Finally, since the participating redox couples have to be transported into/from the bulk solution, mass transport within the wire array may be a concern under conditions of concentrated illumination or low redox concentration[253]. The complicated interaction among multiple factors for device optimization suggests the need for a view of materials engineering at the systems level[254] (**Figure 20**a), analogous with systems biology. This is needed to first answer the fundamental questions that underlie the experimental phenomena, to realize how these factors interact, and then to design a possible structure for device application. For example, as mentioned above, the introduction of a nanowire morphology helps for both electrochemical reaction and charge collection, and usually both effects synergistically increase the photoactivity. One intriguing question is how much of this relative improvement comes from the charge transfer occurring in the chemical reaction vs. from charge collection in the junction. A comparative study by using different redox couples with various charge transfer rates could answer such a question[255], and can enlist directions for further device optimization.

The above discussion mostly assumes that a photoelectrode carries out a half-reaction, most commonly proton reduction or oxygen evolution. But every electrochemical device requires both reduction and oxidation, and more specifically the discussed “Z-scheme” of artificial photosynthesis requires one photocathode and one photoanode to drive the overall reaction. There have not been many efforts to answer whether the nanowire morphology can be used as the building block to fabricate a device capable of performing an overall process to capture sunlight and produce fuels. Equipped with an understanding of its various interfaces [256], an integrated Si/TiO_2 nanotree structure composed of nanowires has been designed and demonstrated for solar-driven water splitting (Figure 20b)[257]. Analogous with the natural photosynthesis process, light-absorption, charge separation, and chemical reactions have been carefully designed at a microscopic scale in an inorganic device. When compared to the same composite materials without the tree-shaped structure, the Si/TiO_2 nanosystem was at least one order of magnitude more active, and was capable of achieving an energy conversion efficiency comparable to that of natural photosynthesis. This is quite remarkable, when considering that the overall efficiency is limited by the TiO_2 photoanode that absorbs only ultraviolet light. Bearing the idea of system-level materials engineering in mind (Figure 20a)[254], newly discovered components, for example a nanowire photoanode with a smaller band gap, will be able to replace old ones to yield better performance.

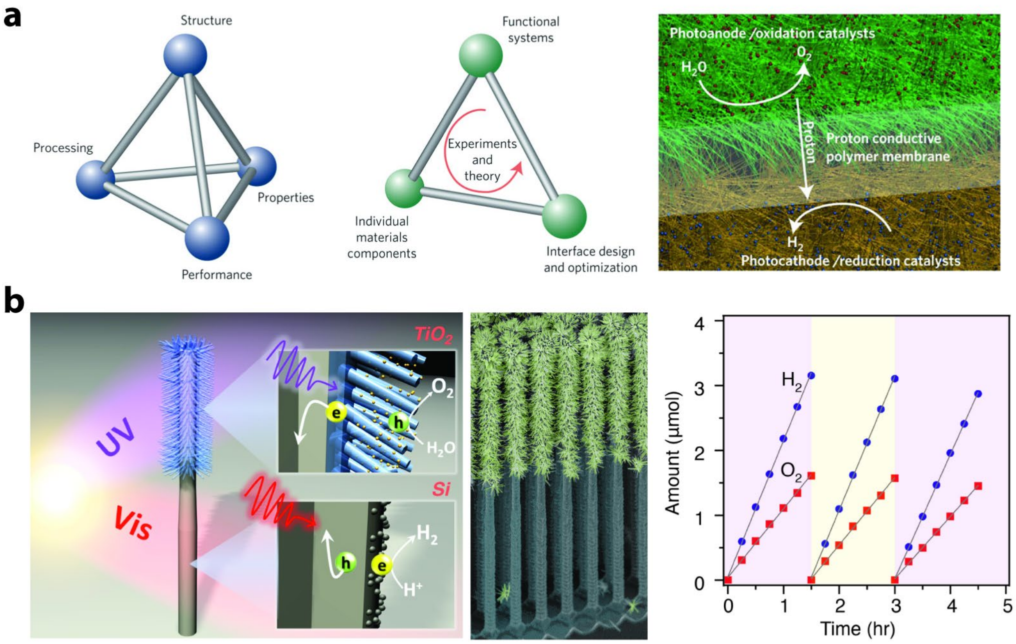

Figure 20. a) Systems-level materials engineering is needed to balance various factors from multiple components in order to achieve optimized performance in artificial photosynthesis. Reproduced with permission.[254] Copyright 2012, Nature Publishing Group. b) To illustrate this concept, a fully integrated nanosystem composed of nanowires has been constructed, which demonstrated water-splitting performance comparable to that of natural photosynthesis. Reproduced with permission.[257] Copyright 2013, American Chemical Society.

To summarize, it is clear that the concept of using nanowires has merit for solar-to-fuel conversion, both for energy capture from sunlight and for electrochemical charge transfer. Moreover, a core-shell nanowire heterojunction offers additional benefits by combining the advantages of multiple materials. While nature has evolved for millions of years to tackle the challenges of photosynthesis, we are just beginning our journey toward producing fuels from sunlight. Nanostructures are powerful tools with which to design integrated microscopic systems, and it is possible that their use will enable practical applications of efficient solar-to-fuel conversion.

8. Nanowires for Lithium-Ion Batteries

Batteries are important for a wide range of applications from portable electronics to electric vehicles to backup power supplies. These devices are often characterized in terms of a Ragone plot, which compares the energy density (J/kg) and power density (W/kg) of various storage technologies. Both of these properties should be optimized to fit the needs of the specific technology application. For example, in the transportation sector, a large energy density is desirable to maximize the range of the vehicle, while a large power density is desirable to maximize the performance of the vehicle. Additionally, both volumetric (J/m^3) and gravimetric (J/kg) energy density are critical for mobile applications such as portable electronics. Therefore, improved battery technologies should maximize and maintain the energy stored per unit volume and weight, while also maximizing the rate of charging/discharging the storage unit.

To address these challenges, the nanowire geometry has been studied due to several favorable properties (**Figure 21**a). In the case of lithium-ion batteries, the ability to improve the density of lithium stored the electrode materials is desirable to increase capacity. However, when inserting large amounts of lithium into a solid electrolyte, volume expansion can cause mechanical degradation due to large volumetric strains. A nanowire geometry can compensate for this, by allowing for larger strains, enabling the use of materials such as silicon as an anode[258]. Furthermore, the nanowire architecture provides a direct current pathway to the electrode, improving charge transport compared to nanoparticle electrodes, which rely on inter-particle charge transfer. Nanowires grown directly on a metal electrode surface can also avoid the need for adding a binder material to the electrode. The high surface-areas and short required ionic diffusion lengths in the electrode material have the potential to increase charge-discharge times, although a high electrode-electrolyte interfacial area may also accelerate undesirable side reactions at this interface[259]. Another challenge is the reduced packing density of nanowires compared to bulk materials, which can lead to a lower volumetric energy density, highlighting the need for high density arrays. Here we highlight several examples of both anode and cathode materials which have incorporated nanowires.

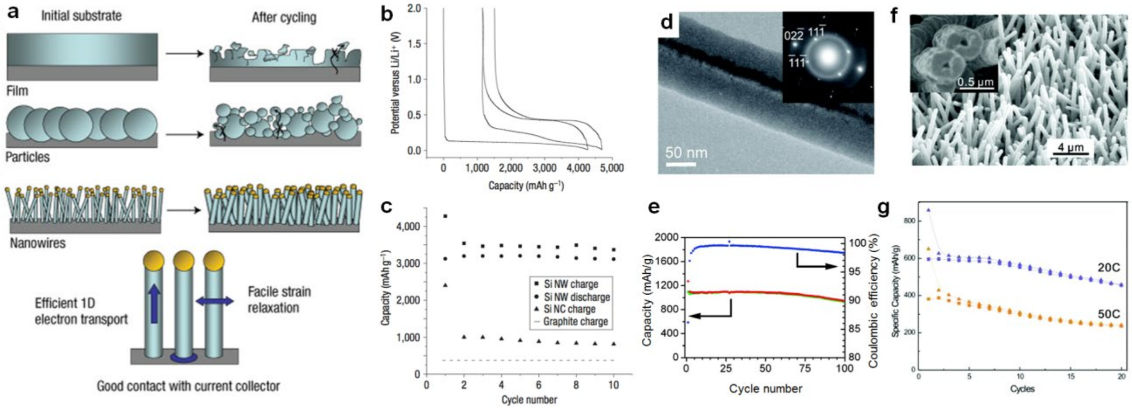

Figure 21. Nanowire array electrodes for batteries. a) Schematic of advantages of NWs for battery electrodes. (top) Bulk materials such as Si suffer from large volume expansions upon lithium insertion, leading to large mechanical strains and failure after cycling. (bottom) NW arrays allow for strain relaxation, leading to improved mechanical stability upon fracture. NW arrays also provide a direct current pathway to the current collector, while minimizing lithium diffusion lengths inside the NW. b) Crystalline Si NW anode voltage profiles for first and second galvanostatic cycles and c) capacity vs. cycle number for the first 10 cycles at a C/20 rate. Frames (a-c) reproduced with permission.[258] Copyright 2008, Nature Publishing Group. d) TEM image with SAED pattern of a crystalline-core amorphous-shell Si NW and e) capacity (left y-axis) and coulombic efficiency (right y-axis) vs. cycle number of core-shell NW arrays with a cutoff voltage of 150 mV and discharge rate of 0.2C. Reproduced with permission.[260] Copyright 2008, American Chemical Society. f) SEM image and g) capacity vs. cycle number at two different discharge rates of mesoporous Co_3O_4 NW arrays. Reproduced with permission.[261]

8.1 Anodes

The potential advantages and disadvantages of nanoscale materials has been experimentally studied by many groups, with long-recognized potential advantages of short diffusion lengths and improved strain accommodation[259]. In the case of the anode (negative electrode) of the battery, the standard material used is graphite. While this material has several advantages such as relatively low cost and high electrical and ionic conductivity, it is limited to a theoretical capacity of ~372 mA-h/g, and suffers from capacity loss during repeated charge/discharge cycles. Therefore a variety of different anode materials based primarily on either intercalation, alloying, or conversion (redox) reactions with lithium are being explored in the nanowire geometry[262].

Among the various metal oxide materials which employ an intercalation mechanism, TiO_2 has been heavily studied. An early example of the study of lithium intercalation into nanowire arrays was performed on TiO_2-B nanowires synthesized by a hydrothermal method[263]. A lithium storage capacity of up to 305 mA-h/g was measured, with very little capacity loss upon cycling, and a rate capability superior to nanoparticle electrodes of the same diameter. TEM analysis confirmed that the nanowire morphology was maintained after 200 cycles, without evidence of the formation of a solid-electrolyte interface (SEI) layer on the surface. These electrodes were used to fabricate rechargeable lithium-ion polymer batteries using either $LiFePO_4$ or $LiNi_{0.5}Mn_{1.5}O_4$ as a cathode material[264]. A capacity of 225 mA-h/g was measured, with excellent capacity retention. A rate capability of 80% of the low-rate capability was maintained at a discharge rate of C/5 (full capacity discharged over 5 hours), demonstrating the advantage of the nanostructured morphology for high power applications. Around the same time, the spinel phase $Li_4Ti_5O_{12}$ was fabricated via hydrothermal synthesis, which also showed improved rate capability compared to the bulk spinel material[265]

A variety of metal oxide materials (based on Co, Ni, Cu or Fe) based on conversion reactions have also been explored due to their high theoretical capacities[266]. The Tarascon group demonstrated high rate capabilities using Cu-Fe_3O_4 core-shell nanorods fabricated by templated electrodeposition[267]. Similar to in photoelectrochemical core-shell structures, this strategy is attractive to improve electronic transport along the NW axis. These electrodes demonstrated a factor of six improvement in power density compared to planar electrodes, and maintained a capacity of over 80% at a discharge rate of 8C. Biological templating using viruses has also been used to fabricate Co_3O_4 NWs, and Co_3O_4-Au hybrid nanowires[268]. It was found that by incorporating Au nanoparticles into the Co_3O_4 NWs, the capacity increased due to either a catalytic effect from the Au, or an improved conductivity of the NWs. In addition, self-assembly of viruses was used to create a 2-D assembly of NWs, demonstrating the potential benefits of biological self-assembly for creating ordered NW arrays. Co_3O_4 NWs were also fabricated by templating in mesoporous Si, which showed an initial increase in capacity first 10-15 cycles, followed by dramatic decrease attributed to loss of morphology to isolated particles[269]. However, these NWs required the addition of a conductive binder to form the electrode, which reduces some of the potential benefits of the NW array morphology compared to nanoparticle approaches. To address this challenge, single-crystalline, mesoporous Co_3O_4 NWs were fabricated using a solution-based approach[261] (Figure 21f). These arrays were grown directly on a conductive substrate, providing a direct current path to the electrode. An irreversible capacity loss was observed after the first discharge cycle, followed improved reversibility in subsequent charge-discharge cycles, resulting in a capacity of 700 mA-h/g after 20 cycles (Figure 21g). Additionally, 50% of the capacity was retained at a discharge rate of 50C, confirming the benefits of short ionic diffusion lengths in NW electrodes.

SnO_2 has also been extensively studied as an anode material due to a high theoretical capacity, although it suffers from significant capacity fading due to the large volume changes which occur upon lithium uptake, suggesting a potential benefit from the NW geometry due to strain relaxation. Self-catalyzed growth of SnO_2 NWs showed higher initial Coulombic efficiency, and decreased capacity fade compared to SnO_2 powders[270]. This is another successful example of the benefits of a 1-D geometry, including short lithium diffusion lengths associated with the NW diameter, and improved charge transport along the NW length. It was also found that by creating core-shell In_2O_3-SnO_2 NWs, both the electrical conductivity and anode performance could be improved, although capacity fade still remained an issue for these materials[271]. A decreased capacity fade was observed in very small, polycrystalline SnO_2 NWs fabricated by a templating method in in mesoporous SiO_2, but the NW morphology was observed to degrade into aggregated nanoparticles after several discharges[272]. Again, the use of these template wires required a binder, and an increased percolation pathway for charge transport. In contrast, hydrothermal SnO_2 NWs were grown directly on flexible metal foil substrates without the need for a binder[273], which exhibited a reversible capacity of 580 mA-h/g after 100 cycles at a rate of 0.1C.

To visualize and gain an improved fundamental understanding of the insertion of lithium into SnO_2 NW on a single-NW level, an *in situ* electrochemical cell for TEM observation was fabricated based on a SnO_2 NW, an ionic-liquid based electrolyte, and a $LiCoO_2$ cathode[274] (**Figure 22**a). This allowed for direct observation of the expansion in the length and diameter of the NW, accompanied by large plastic deformation in the NW shape. The propagation of the lithium into the nanowire was accompanied by a region with a high density of dislocations at the interface between the pristine SnO_2 material and the reacted portion of the NW. This dislocation region led to the amorphization of the crystalline material, and facilitated lithium insertion into the crystalline SnO_2. Observation of the diffraction pattern during lithiation showed the loss of the crystalline SnO_2 structure, and the eventual formation of Li_xSn and Sn nanoparticles dispersed in an amorphous Li_2O matrix. Despite the dramatic increase in volume and morphology changes, fracture of the NW was not observed, providing further evidence of the mechanical robustness of the NW geometry under large stresses.

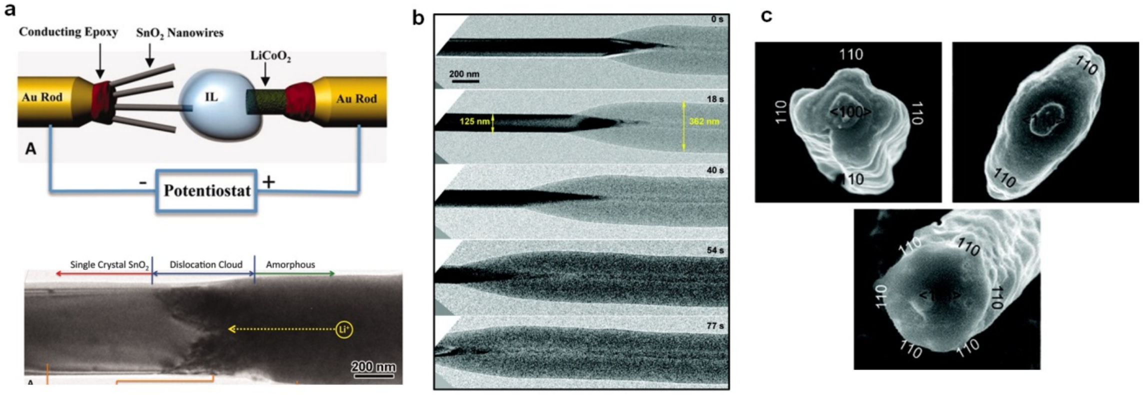

Figure 22. Single nanowire lithiation studies. a) *In situ* TEM investigation of lithiation of a single SnO_2 NW. (top) Schematic of experimental cell with a $LiCoO_2$ cathode, ionic liquid electrolyte, and SnO_2 NW anode. (bottom) TEM image of a nanowire with a crystalline unreacted region, amorphous lithiated region, and "dislocation cloud" at the reaction front. Reproduced with permission.[274] Copyright 2010, American Academy for the Advancement of Science. b) Time lapse TEM series of the lithiation of a single Si NW using a similar setup. Reproduced with permission.[275] Copyright 2011, American Chemical Society. c) SEM images of anisotropic expansion of Si nanopillars with three different crystallographic orientations after lithiation. Reproduced with permission.[276] Copyright 2011, American Chemical Society.

Among the various potential anode materials, silicon has the highest known theoretical charge capacity (4,200 mA-h/g), which is significantly higher than graphite or the previously mentioned metal oxide materials. However, to accommodate this large quantity of lithium, a significant expansion of the silicon material is required (~400% volume expansion), leading to large mechanical strains and fracture behavior in bulk or micro-structured materials. To address this issue, VLS-grown Si nanowires were grown directly on stainless steel substrates and tested as an anode material[258]. The measured capacity during the initial charge was 4,277 mA-h/g, which is essentially equivalent to the theoretical capacity (Figure 21b). The coulombic efficiency during the first discharge was 73%, followed by a second charge capacity of 3541 mA-h/g. After this initial loss of capacity, the little capacity loss was measured for the first 10 cycles (Figure 21c). The NW anodes also displayed high capacities and excellent cyclability at higher discharge rates. Around the same time, top-down metal-induced chemical etched Si NWs were tested as a promising anode material, although the specific capacity of the NWs could not be measured due to contributions from the Si wafer substrate.[277]

The use of a NW architecture allows for *ex situ* TEM observation of the evolution of the Si crystal structure and morphology during charging/discharging. During the initial charging, the Si material in the VLS-grown NWs was observed to transform from crystalline Si into amorphous $Li_{4.4}Si$[258]. The evolution from a crystalline NW to the formation of an amorphous shell and subsequent amorphization of the entire wire was observed at different potentials. Additionally, *in situ* TEM analysis has been performed on single Si NW electrochemical cells to directly observe the lithiation process. Liu et al. fabricated a cell based on a single Si NW, an ionic liquid electrolyte, and a $LiCoO_2$ cathode [275] (Figure 22b), similar to the single SnO_2 NW cell. They observed a dependence of lithium charging speed and storage capacity on the doping of the NW, which was also increased by incorporating a carbon coating. The initially crystalline Si wire was transformed to amorphous Li_xSi during the lithiation process, which was subsequently transformed to Li crystalline $Li_{15}Si_4$. In another study, the authors observed anisotropic swelling of the NWs during lithiation, leading to the formation of a dumbbell cross-section which resulted during the propagation of lithium along the length of the wire[278]. This was attributed to variations in the diffusion rate along different crystallographic directions, which led to anisotropic stress profiles in the material. Anisotropic swelling was also observed by SEM analysis of Si NWs with different growth directions after first lithiation, showing a transformation from initially circular cross-sections to cross, ellipse, or hexagonal shapes based on growth direction[276] (Figure 22c). This is explained by a fast lithium diffusion rate along the <110> direction.

After the initial development of Si NW anodes, the concept was extended to core-shell NW architectures. To improve upon the single-crystalline Si NW design, crystalline-amorphous core-shell NWs were grown directly on stainless steel substrates[260] (Figure 21d). By limiting the charging potential, the amorphous core could be selectively used to store Li, while the crystalline Si core remains intact, providing structural stability and improved charge transport. While the initial lithium storage capacity is less in this architecture (~1000 mA-h/g), the core-shell architecture leads to improved capacity retention, with ~90% capacity retention over 100 cycles (Figure 21e). TEM analysis confirmed that the core remained crystalline under these charging conditions. This concept was subsequently extended to carbon nanofiber-amorphous Si core-shell architectures[279], which allowed for charging to ~2000 mA-h/g due to the lower lithium capacity of carbon, while maintaining the benefits of improved cycle life and charge transport through the conductive core. This anode allowed for an improved area capacity of ~4 mA-h/cm^2, which is comparable to commercial battery materials. Si NW anodes have also been coated with conducting polymer coatings, which has shown to significantly enhance cycle stability compared to pristine NWs[280].

While Si anodes allow for a high charge capacity, the overall capacity of the battery using traditional cathode materials will still be limited by the cathode. Therefore, Si NW anodes have been used in combination with nanostructured Li_2S/carbon composite cathode to demonstrate lithium-metal free battery with high theoretical capacity[281]. In another approach to achieve a lithium-metal free battery with high capacity, prelithiated Si NWs loaded to 2000 mA-h/g were combined with a sulfur cathode[236b]. This removes the requirement to use pre-lithiated cathode materials, opening up the possibility for a new class of battery based on high-capacity cathodes.

VLS-grown germanium nanowires have also been grown under a similar scheme as the VLS Si NWs, and were tested as anodes[282]. In the case of Ge, the initial charge capacity was 2,967 mA-h/g, which is significantly higher than the theoretical capacity of 1,600 mA-h/g. This was attributed to irreversible side reactions. The first discharge capacity at a rate of C/20 was 1141 mA-h/g, which remained relatively constant over the first 20 cycles. A high rate capability was observed at discharge rates up to 2C, with Coulombic efficiency >99%. Similar to the Si NW anodes, the Ge NWs became amorphous upon lithiation, but did not pulverize after cycling, demonstrating the generality of strain relaxation benefits in the NW geometry.

8.2 Cathodes

While significant research has been performed on NW anodes for Li-ion batteries, there has also been work performed on the cathode (positive electrode) side. Various candidates to replace $LiCoO_2$ are being investigated, due to the potential for reduced cost and/or increased capacity. For example, $LiFePO_4$ is a candidate cathode material due to its very low cost, although it has a lower voltage of 3.5 V[262]. $LiFePO_4$ NWs have been fabricated by a hard templating method in porous SiO_2[283]. Similar to the anode NWs fabricated by this method, these NWs required the use of carbon black and a binder material. The electrodes showed a high capacity retention of 89% at a discharge rate of 15C. Amorphous $FePO_4$ NWs were also fabricated based on a virus-based templating method,[284] analogous to the Co_3O_4 NW anodes. To improve the electrical conductivity between the NWs, a two-gene engineering approach was developed to attach single-walled carbon nanotubes to one end of the virus. This improved the high rate performance of the NW cathodes to provide performance comparable to crystalline $LiFePo_4$, with virtually no capacity fade at a discharge rate of 1C after 50 cycles.

Another lithiated metal oxide material of interest as a cathode is spinel $LiMn_2O_4$ due to its low cost and nontoxicity. However, this material suffers from relatively slow lithium diffusion rates in the electrode, making it a good candidate for the NW morphology when used in high power applications. $LiMn_2O_4$ nanorods fabricated by a topochemical method resulted in highly crystalline spinel material, which exhibited low capacity fade and a high rate performance with 88% of the capacity retained at a discharge rate of 5C[285]. Likewise, $LiMn_2O_4$ nanorods fabricated by hydrothermal synthesis of MnO_2 followed by a simple solid-state conversion reaction demonstrated over 85% retention of charge capacity after 100 cycles at a discharge rate of 1C (148 mA/g)[286], which is a much higher capacity retention at this fast discharge rate than commercial $LiMn_2O_4$ powders. Again, this is attributed to the relatively high surface areas and short required Li diffusion lengths in the NW geometry. Much longer faceted single-crystalline $LiMn_2O_4$ NWs fabricated by reacting hydrothermally grown $Na_{0.44}MnO_2$ in a molten salt containing lithium demonstrated even higher rate performance, with over 90% of the capacity remaining at a discharge rate of 5 A/g, and 75% at 20A/g[287]. Moreover, after 100 discharge cycles, these NW electrodes maintained a capacity of over 100 mA-h/g, without losing their single-crystalline morphology. High capacity retention at similar discharge rates was also observed in ultrathin single-crystalline NWs fabricated by solvothermal synthesis of α-MnO_2 followed by solid-state lithiation[288].

Vanadium oxide (V_2O_5) has also been extensively studied in nanostructured architectures as a cathode material with the potential for improved lithium storage capacity[289]. For example, lithium insertion into single-crystalline V_2O_5 nanorods fabricated by templated electrodeposition exhibited a capacity 5 times larger sol-gel derived thin-films at a discharge rate of 0.7 A/g[290]. The size dependence of lithium insertion into V_2O_5 nanoribbons was studied, and it was found that in thin ribbons the transformation into the ω-$Li_3V_2O_5$ phase occurred within 10 seconds, suggesting a diffusion constant 3 orders of magnitude higher than in bulk materials[291]. It was also shown that ultralong hierarchical V_2O_5 NWs with millimeter lengths could be fabricated by a low-cost electrospinning and annealing process[292], which provided an initial discharge capacity of 390 mA-h/g and a capacity of 201 mA-h/g after 50 discharges when cycled between 1.75 V and 4.0 V. This geometry was found to prevent aggregation compared to shorter nanorods, while retaining the improved rate capability associated with the 1-D NW geometry.

In summary, NW electrodes present several advantages for batteries due primarily to geometric advantages compared to bulk materials. The short diffusion lengths for ions in the radial direction allow for improved performance at high discharge rates, because a lower driving force is required to supply ions at a high rate. Addionally, strain relaxation in the NW geometry allows for successful use of high capacity materials such as silicon, which suffer from severe mechanical degradation in planar architectures. It was shown that to maximize the benefits of the NW geometry, wires should be grown directly off of a conductive charge collector, to avoid the need for adding binder materials and decrease the percolation pathway for electronic charge transport. The core-shell geometry was also shown to be beneficial to reduce electrical resistivity in the electrodes. However, challenges remain, including a reduced packing density (reducing volumetric energy density), and passivation of surfaces against undesirable side reactions at the electrode-electrolyte interface, which can increase when using high surface-area electrodes. While significant progress has been made in these NW battery materials, commercialization of the technologies will rely on continued improvement of energy density while maintaining the high rate capability benefits and minimizing capacity loss after large numbers of charge-discharge cycles.

9. Nanowire Mechanics

In addition to the novel optical, electronic, and thermal properties of nanowires, technological advances have been achieved based on the mechanical properties of nanowires. Due to the high surface-to-volume ratio of nanowires, their mechanical properties are strongly influenced by the nature of the surface atoms. In addition to a different bonding nature of surface atoms, surface stresses play in important role in the mechanical properties of nanowires.

9.1 Elastic Properties of Nanowires

The elastic properties of a material are often characterized by the Young's modulus, which is a measure of the strain response to an applied stress. This has been measured experimentally for various types of nanowires using bending, resonance, or tension techniques. Early measurements of the elastic modulus of nanowires were performed by bending individual wires with an atomic force microscope (AFM) tip, and measuring the corresponding force-displacement data[293]. Tensile testing has also been performed to extract the stress-strain behavior[294]. Alternately, individual NWs can be resonantly excited by a conductive AFM tip to extract the mechanical elastic properties[295]. Resonance measurements can also be performed *in situ* in a TEM, allowing for a direct observation of the wire including structural and crystallographic information[296].

Several experimental measurements of nanowires have demonstrated size-dependent phenomena in the elastic modulus[295, 297]. These deviations are often explained by surface stress effects, which have been supported by computational simulations of NW surfaces[298]. Additionally, a continuum approach has been developed for NWs with larger diameters, using the Young-Laplace equation to incorporate the effects of surface stress into the Euler-Bernoulli equation[299]. These surface stresses can lead to atomic reconstructions on the surface, which affect the diameter dependence of the elastic properties[297b]. Variations in the effect of the nanowire geometry on the elastic properties depend on the type of material, type and concentration of defects present, crystallographic orientation, and cross-sectional shape. Furthermore, simulations have shown that as the NW diameter becomes smaller, the measured elastic properties will vary based on the measurement technique employed, due to an increased concentration of stress at the surface during bending conditions compared to tension testing[300]. This highlights the need for multiple testing techniques to gain a full picture of the elastic properties of NWs.

9.2 Plastic Deformation and Failure of Nanowires

In addition to variations of the elastic properties between nanowires and bulk materials, the nanowire geometry affects the plasticity and eventual failure mechanisms of nanowires under applied stress. By applying a lateral force to a suspended NW which is clamped on both ends over a trench, the entire force-displacement behavior of a NW can be measured from elastic strain to yielding and fracture[301]. This technique was used to demonstrate ultrahigh-yield strength in gold nanowires, which exhibited strain-hardening with diameters down to 40 nm[293c]. Additionally, the bending strength of NWs can be measured by the lateral deflection of a vertically-oriented NW with an AFM tip, which was used to measure a bending strength near the theoretical maximum in VLS-grown Si NWs[302].

The fracture mechanics of NWs can also be measured by tensile stress-strain techniques. By employing a MEMS-based nanoscale testing stage, the fracture behavior of individual ZnO NWs has been observed *in situ* in a TEM[303]. This approach allows for the measurement of the stress-strain behavior of individual NWs until fracture occurs. In the case of ZnO wires, brittle fracture was observed, which was preceded by the observation of localized stress concentrations at the site of failure. This allows for a quantitative analysis of the fracture statistics of NWs, as well as an observation of the smooth fracture surface, which is consistent with brittle fracture. Tensile testing on VLS-grown Si NWs has also been performed using an AFM cantilever to measure force inside an SEM[294]. Linear elastic behavior was observed until fracture, with no detectable plasticity for wires down to a diameter of 15 nm. Both the fracture strength and strain were observed to increase with decreasing wire diameter, showing the robustness of the NW geometry for applications which involve mechanical forces.

The compressive behavior of NWs has also been observed, and NW buckling has been measured. The buckling behavior of individual Si NWs was measured by manipulation using a tungsten probe, and measurement of the force-displacement behavior under compression using an AFM inside of an SEM[304]. Bucking behavior characteristic of a thin column under an axial compressive load was observed, without fracture for very large deformations, indicating that the NW geometry greatly increases the flexibility of the crystalline Si material beyond the bulk. Buckling behavior is also influenced by surface stresses, which must be taken into account when measuring the mechanical properties of NWs under compression[305]. Additionally, buckling behavior[306] and the hardness[307] of NWs can be tested using a nanoindentation technique.

The plastic deformation of NWs has been modeled by computational simulations[298b]. For example, molecular dynamics (MD) simulations have provided atomic-scale insight into plastic deformation and failure mechanisms as a function of temperature and strain rate[308], as well as cross-sectional geometry[309]. Simulations have also predicted phenomena such as stress-induced phase transformations in ZnO wires[303]. However, discrepancies remain between the simulations and experimental results, which are compounded by variations in the experimental data. This could be attributed to a number of factors, including defects in experimental wires, strain-rate effects, and inadequate potentials for the simulations, suggesting the need for multi-scale models based on quantum mechanical considerations[298b].

9.3 Nanowire Mechanical Resonators

Nanowires are of interest as mechanical resonators, due to their ability to achieve resonant frequencies in the very high frequency (VHF) range, allowing for improved sensitivity as sensors and in nanoelectromechanical systems (NEMS) applications[310]. The damping behavior of resonators is characterized by the Q-factor, which is a function of several variables including both internal and external damping forces. While high Q factors can be achieved in vacuum for top-down[310] and bottom-up synthesized NWs[311], a low mechanical Q factor due to viscous damping for the NW geometry (comparable to the damping of micro-scale cantilevers in water) limits the sensitivity of resonators in air[312]. Additionally, surface roughness is an important factor to maximize the Q-factor, as observed in the high Q-factor for GaN NWs (~3000 in high vacuum)[297a] compared to top-down Si NWs of the same surface-to-volume ratio. This is attributed to the smooth GaN NW surfaces, minimizing “internal friction” losses compared to etched NWs.

VHF resonators based on double-clamped VLS-grown Si NWs (**Figure 23**a) were demonstrated to have quality factors of up to Q ≈ 13,100 for pristine unmetalized NWs[311b]. However, due to the large electrical impedance (~1-100 kΩ) of these wires, metalized Si NW with impedances compatible with standard 50 Ω RF components have also been fabricated based on these structures, which exhibited Q values of Q ≈ 2,000-2500 at a frequencies near 200 MHz. These wires have the potential for extremely low mass sensitivity on the zeptrogram scale. These suspended doubly-clamped resonators were subsequently engineered to produce room-temperature VHF frequency on-chip transducers[313], which exploit the large piezoresistance effect in Si NWs[314]. By incorporating NWs with diameters below 100 nm, efficient displacement transducers can be fabricated which operate at frequencies up to 100 MHz, and with mass sensitivities in the sub-zeptrogram range. This mass sensitivity allows for real-time, single biomolecule detection, and it was proposed that smaller diameter wires could produce mass sensitivities approaching the single Dalton level (1 amu).

Beyond simply mass detection, by measuring the splitting of resonance frequencies of singly-clamped NW resonators it has been shown that the position of the adsorbate on the NW surface can be measured (Figure 23c), as well as the stiffness of the adsorbate[315]. The stiffness sensing resolution for Si wire resonators using this approach is approximately 0.1 kPa per femtogram of sample, suggesting the capability of measuring small changes in biomolecules, such as variations in the stiffness as a result of mutations. Furthermore, parallel arrays of aligned singly-clamped nanowire resonators have been developed using self-assembly techniques (Figure 23b), demonstrating the ability to integrate large numbers of NW resonators fabricated off-chip into on-chip device architectures[316].

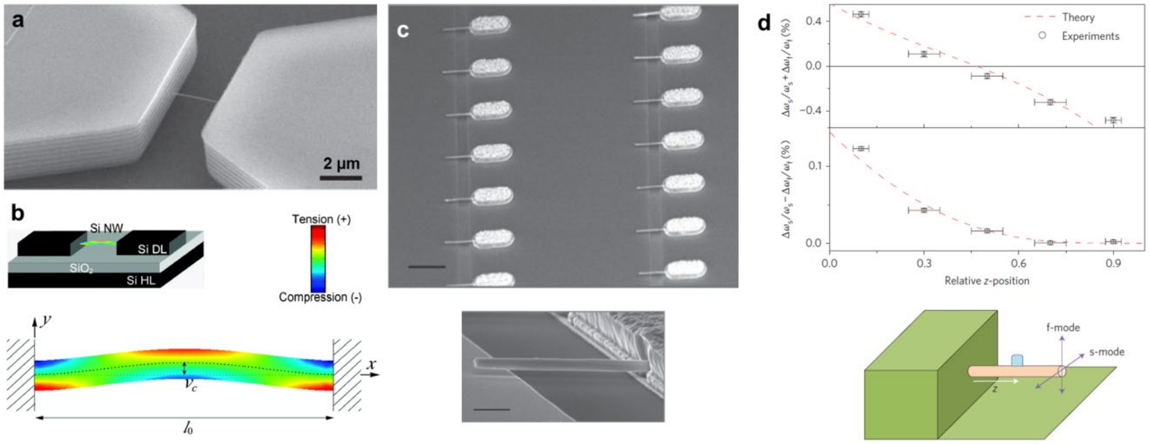

Figure 23. Nanowire mechanical resonators. a) SEM image of a double clamped suspended Si NW grown on a SOI wafer. Reproduced with permission.[314] Copyright 2006, Nature Publishing Group. b) Schematic (top) of a double clamped NW resonator, with a finite element analysis simulation (bottom) of the NW strain during deflection. Reproduced with permission.[313]

Copyright 2008, American Chemical Society. b) SEM images of nanowire resonator arrays fabricated by bottom-up assembly. Scale bar is 10 μm (top) and 1μm (bottom). Reproduced with permission.[316] Copyright 2008, Nature Publishing Group. c) (bottom) Schematic illustration of measurement of mass position of an adsorbate on a NW resonator surface by splitting of resonance frequencies in orthogonal directions. (top) Plot showing relative frequency shifts of a NW resonator with a 3 fg adsorbate deposited at various z-positions. The measured data (symbols) match well to a theoretical model (dashed line) allowing for z-position measurement. Reproduced with permission.[315] Copyright 2010, Nature Publishing Group.

9.4 Nanowire Piezoelectrics

The piezoelectric effect is a well-known property of certain anisotropic crystalline materials, leading to the formation of an electric field within the material when a mechanical stress is applied. Conversely, when an electric field is applied to a piezoelectric material, a mechanical strain results. This can be used in a variety of applications, including nanoscale positioning, force/acoustic sensing, and energy harvesting.

The Wang research group first demonstrated the concept of a piezoelectric nanogenerator using ZnO NWs, which were bent using a conductive AFM tip[317]. The Schottky junction formed between the metallic tip and semiconducting NW allowed for charge separation, and an electric current could be extracted upon bending. This concept has subsequently been developed in the form of single NW and NW array devices[105b, 318], as well as laterally-packaged NWs attached to a flexible substrate[319], with a continual improvement of output voltage[320]. The initial array device design was based on a zigzag top electrode, which acted as an array of AFM tips to generate and extract a DC current from the NW arrays due to excitation from an ultrasonic wave[318]. This design was improved upon by creating vertical and lateral arrays with metal contacts bonded on both ends of the wires, which acted as an AC generator when actuated by a periodic mechanical force (**Figure 24**a-d).[219b] The voltage can be increased by connecting arrays of NWs in series, allowing for voltages useful for powering devices[219b, 321]. By replacing the Schottky junction between the metal contact and NWs by an insulating PMMA layer, the output voltage could be increased up to 58 V for ZnO arrays[322]. These nanogenerators have the potential to harvest energy from sources such as mechanical vibrations, ambient pressure gradients, and biological sources. The nanogenerators are sensitive to a wide bandwidth of excitation frequencies[105b], and are being explored for wireless power for electronic devices that do not require a battery[219b].

Beyond power generation, the properties of piezoelectric NWs have been exploited for electronic devices known as piezotronics. For example, a piezoelectric field effect transistor can be formed[323], which is gated by mechanical strain rather than an applied electric field. This can lead to charge accumulation or depletion at a semiconductor/metal Schottky contact such that the charge transport properties across the interface are modified by the strain[324]. Therefore, strain can be used to control an electrical signal in a device. These devices can be fully packaged on flexible substrates, for strain sensing in a variety of applications[325] (Figure 24e-f). In addition to the piezoelectric effect, giant piezoresistive effects compared to bulk have been observed in Si nanowires, which can also lead to significant variations in conductivity under applied strain[314]. These effects open the possibility for interaction between mechanical systems, including biological systems, and electronic devices for sensing and/or control[326]. For example, large-scale arrays of piezotronic transistors have been fabricated as active pressure/force sensors, capable of mimicking the tactile sensing capabilities of human skin[327].

In addition to coupling the mechanical and electronic properties of piezoelectric semiconductor-metal junctions, the interaction of these devices with optoelectronic effects has been termed the piezo-phototronic effect[326, 328]. The ability to couple piezotronic effects with photon absorption or emission, has led to enhanced performance and unique effects in photodetectors[329] and LEDs[330]. This effect has been used to develop pressure sensors based on arrays of individual NW-LEDs, which can map pressure variations with micron resolution through light emission[331] (Figure 24g-h).

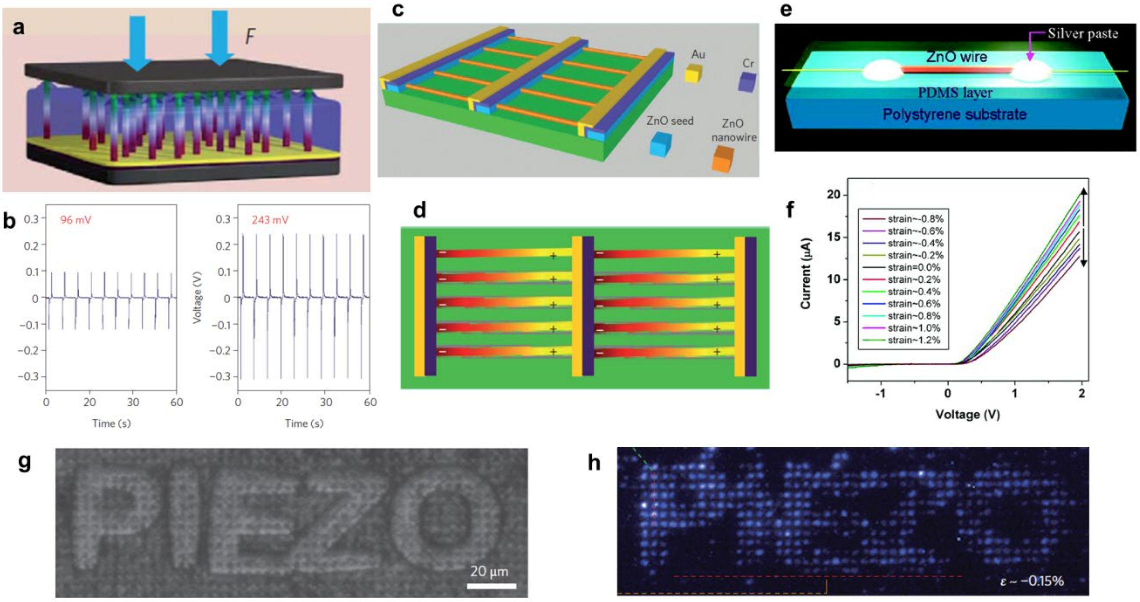

Figure 24. Nanowire piezoelectrics. a) Schematic of a vertical ZnO NW array integrated nanogenerator, and b) voltage response of (left) single vertical-array nanogenerator and (right) device with 3 generators connected in series. c) Schematic of a lateral ZnO NW array integrated nanogenerator and d) principle of operation, showing polarization of NWs upon deformation. Reproduced with permission.[219b] Copyright 2010, Nature Publishing Group. e) Schematic of a flexible piezotronic strain sensor based on a single ZnO NW, and f) typical I-V characteristics of a sensor at different levels of strain. Reproduced with permission.[325] Copyright 2008, American Chemical Society. g) Optical image and h) electroluminescence image of n-ZnO/p-GaN NW LED arrays with a convex mold on top, allowing for visual mapping of applied pressure from the mold with high spatial-resolution. Reproduced with permission.[331] Copyright 2013, Nature Publishing Group.

10. Nanowire-Cell Interface

The nanowire-living cell interface is another emerging area of great interest. First, the cross sections of nanowires are much smaller than the typical cell dimensions yet larger than that of the lipid bi-layer, which means they can easily penetrate cell membranes while leaving the cellular structures and functions intact[332]. Second, their high surface to volume ratio ensures proper cell−nanowire interaction for chemical/bio/electrical sensing[333], as well as payload delivery[334]. The most unique feature of nanowires, when compared with other nanoscale materials for bioassay such as quantum dots or gold nanoparticles, is their high aspect ratio, which makes it feasible to communicate optical and electrical signals across cellular membranes[333b, 333c, 334b]. This provides an extra handle for targeted, high-resolution, and even addressable intracellular monitoring. For the past two decades, a comprehensive understanding of controlled nanowire synthesis, functionalities, device fabrication and surface modification has offered an ideal starting point for implementation of nanowires as a powerful platform to interface with living cells for various purposes. These include precise and/or high throughput delivery of small and macro bio-active molecules into the cytoplasm, measurement and recording of neuronal action and response to study neuron circuit-connectivity and physiology, high spatiotemporal resolution subcellular imaging and sensing, as well as their potential use as a universal platform for guided stem cell differentiation.

10.1 Nanowire FET based neuron physiology

The first attempt of interfacing nanowire with live cells was the tour de force demonstration by the Lieber group of high density silicon nanowire transistor arrays for the detection, stimulation, and inhibition of neuronal signal propagation[335]. The multiplexed and individually addressable arrays of nanowire transistor-neuron junctions enabled simultaneous measurement of the rate, amplitude, and shape of signals propagating along individual axons and dendrites of a single living neuron (**Figure 25**a). This task was very difficult to fulfill if not impossible with traditional micropipettes because of the difficulty in signal multiplexing, or microfabricated electrode arrays because of their poor spatial resolution for detection and stimulation of neuronal activity at the level of individual axons and/or dendrites. This pioneering work marked the debut of the nanowire FET-based neuron physiology technique that is now capable of recording extracellular[336] and intracellular[333a, 337] action potentials of individual heart muscle cells with high signal to noise ratio, in-vivo recording of the beating of a whole heart[338], as well as multiplexed mapping of neural circuits in acute brain slices with simultaneous high temporal and spatial resolution[339].

Lately, the scope of the nanowire FET-live cell interface has been further expanded to the engineering of "cyborg-tissue" to address the long-standing problem in the field of tissue engineering of getting biomaterials to monitor or interact with chemical and electrical changes around them, like normal human tissue does. The strategy proposed to mimic these natural feedback loops in synthetic tissues is to use integrated nanowire FETs arrays with biocompatible extracellular scaffolds, from which the Lieber group has demonstrated the three-dimensional (3D) culture of neurons, cardiomyocytes and smooth muscle cells into tissue, as well as the capability to monitor the local electrical activity throughout their 3D and macroporous interior and their response to cardio- or neuro-stimulating drugs in real-time[340]. The development of such "cyborg-tissue" will directly benefit pharmaceutical industry by allowing for drug testing in 3-D tissues, and advance our fundamental understanding of human functions and the body's ability to detect and response to external stimuli.

10.2 Vertical Nanowire Arrays for Cell Culture, Payload Delivery, Neurophysiology and Therapy

In contrast to nanowire FETs, which are primarily specialized for interacting with electrically active cells with the aim of high spatial- and temporal-resolution in electrical measurements, vertically aligned nanowire arrays represent a more universal and versatile platform for high throughput live cell manipulation and assays. In 2007, the Yang group successfully cultured mammalian stem cells (mouse embryonic stem cells) directly on a Si nanowire array with a uniform diameter of ~90 nm and length of ~6 μm, demonstrating for the first time the direct interconnection of nanowires with living cells (Figure 25c).[332a] The cells grown on the nanowire array were penetrated by the Si nanowires within approximately 1 hour as they settled on to the substrate without the application of external force. The stem cells pierced by nanowires not only survived for days, but also continued to differentiate into beating heart muscles on the bed of needles. As a proof of concept, the researchers also showed that they could introduce a small amount of DNA into human embryonic kidney cells, demonstrating the feasibility of the Si nanowire arrays for gene delivery. This groundbreaking work holds profound implications for many aspects of live cell research, including cell culture, attachment and manipulation, drug discovery, cellular reprogramming, cell and system biology, neuron electrophysiology, and potentially tissue engineering, where vertical nanowire arrays can be expected to introduce programmable electrical and chemical stimuli to guide stem cell differentiation.

The exciting potential of this work has been extensively explored over the last several years. A wide variety of cell lines have been successfully cultured on different nanowire arrays to study the nanowire-cell interface, as well as the impact of nanowire impalement on live cell functions and structure[332b, 341]. Park and co-workers have developed these vertical Si nanowire arrays into a universal platform to introduce a broad range of exogenous materials (siRNAs, peptides, DNAs and proteins) into multiple mammalian cell types, both immortalized (Hela) and primary (human fibroblasts, rat neural progenitor cells and rat hippocampal neurons), with high throughput by attaching biomolecules to nanowire arrays pretreated with 3-aminopropyltrimethoxysilane (APTMS), a chemical that would allow molecules to bind relatively weakly to the surface of the nanowires[334a]. These nanowire arrays can also manipulate genes in various primary immune cell lines without activating an immune response or interfering with their immune functions[342]. This nanowire-based approach was quickly adopted by biologists to deliver genes into fragile immune cells that are extremely difficult to transfect otherwise, which has led to the discovery of new components in a crucial pathway that allows immune cells to detect viral invaders[343] and the molecular circuitry controlling the differentiation of T helper 17 (T_H17) cells, a type of white bold cell that has been linked to autoimmune diseases, such as multiple sclerosis and type 1 diabetes[344].

The fact that cells can engulf vertical nanowires arrays into their interior without affecting their vitality, structures and functions has offered an intriguing solution for intracellular mapping of neuron activity. The flow of electrical currents in a given cell was traditionally measured using micropipette electrodes, however, it is extremely hard to conduct such measurement without harming the cell's membrane or interfering with its activity. It is also difficult to monitor multiple cells simultaneously. Recently, two research groups independently devised nanoelectrode arrays based on vertical nanowire arrays for intracellular recordings. Park and co-workers[333b] built their electrode arrays from doped, conducting Si nanowires (150 nm in diameter and 3 μm in height) that are capped with a conducting metal tip (Figure 25d). Cui and co-workers[333c] built arrays of nanopillars made of platinum that are also 150 nm in diameter, but slightly shorter in height (1-2 μm). Since cells cultured on nanowire arrays wrap the nanowires in a thin layer of cell membrane to separate the nanowire from the cell interior[345], both groups had to resort to a technique called membrane electroporation to get the nanowires efficiently into cells, where they applied small electrical currents through the nanoelectrodes to make infinitesimal holes in the cell membrane near the electrodes. Both of these nanoelectrode arrays allowed for intracellular monitoring of action potentials from multiple cells simultaneously over a long period of time (hours to days), and are much less damaging to the cells than conventional micrometer-sized pipettes. However, the amplitude of recorded signals were one order of magnitude smaller than that of micropipette electrodes and nanowire FETs with a branched nanotube inserted into the cell[337b]. Nonetheless, these nanoelectrode arrays hold great promise for studying bioelectricity in nerves and heart muscles, and for brain activity mapping by packing hundreds of thousands of these nanowire electrodes into flexible sheets that conform to the surface of the brain with minimal tissue damage.

The engineered nanotopographic cell culture substrate and the ability of vertical nanowire arrays to effectively interact with the cell membrane and access the cell cytoplasm also provide new insight into effective cell capture, separation and assays. Immuno-functionalized transparent quartz nanowire arrays can effectively capture rare tumor cells from a heterogeneous cell population or even human whole blood, and has enabled laser scanning imaging cytometry for automated quantitation of captured cells and rapid evaluation of functional cellular parameters[346]. Au nanoparticle coated Si nanowire arrays with antibody coatings are also capable of simultaneous capture and plasmonic photothermal therapy for circulating tumor cells[347]. Such functionalized nanowire arrays represent a powerful platform for the investigation of the biology of rare tumor cells and for differential diagnosis of cancer progression and metastasis. In addition, endogenous enzyme activity in live cells can be detected by a “sandwich” assay, where cells are “sandwiched” in between a nanowire cell holder and a nanowire exogenous enzymatic substrate to allow well timed access of the enzymatic substrate into the cell cytoplasm[348]. Subsequent dissembling of this nanowire–cell sandwich allows for detection of changes induced to the enzyme substrates by fluorescence microscopy and mass spectrometry, demonstrating the assay’s potential for probing enzyme function in situ.

10.3 Nanowire-Based Single Cell Endoscopy

To dissect the complexity of mammalian cells, where different subcellular functional units orchestrate a variety of biological processes, non-invasive optical tools that have high spatial and temporal resolution are central for the studying of individual events inside these compartments. Current optical methods for studying subcellular events rely on high-precision optical imaging systems that are bulky, complicated and expensive. Furthermore, standard light microscopy is not applicable to the study of individual cells deep within living tissues.

Mobilizing optical spectroscopy techniques with our current knowledge of nanomaterials is an essential component to revolutionize subcellular fluorescent assay. In particular, the introduction of a nanoscopic light source into the organism, without interfering with cellular functions or compromising the outer cell membrane, could lead to non-invasive means for in-situ living cell imaging and sensing with high spatial and temporal resolution and precision. Such light sources, or essentially a nano-endoscope, will be able to probe sub-cellular events (e.g. infection and pathogen response), sense local environments both optically and chemically for disease diagnostics, induce photo-destruction (i.e., photodynamic therapy) of cancerous cells or tissue, or induce local optical and chemical stimuli to guide stem cell differentiation.

Such a milestone device has been demonstrated recently by combining subwavelength optical waveguide and fiber optic technology for highly localized optical imaging and cargo delivery in a single living cell (Figure 25e).[334b] Because of the small cross section of the nanowire probe (~250 nm), the nanowire endoscope doesn’t kill the cell or induce any apparent cellular stress while being able to achieve an illumination/detection volume down to picoliters to avoid the excitation and collection of unwanted signals from cellular autofluorescence or other sources distant from the tip. Functionalization of the probe tip itself with a fluorescent sensor can additionally confine the signal and ensure measurement of only local changes, which was demonstrated with pH sensing in micro-droplets. The small dimension of the nanowire also enables localized delivery of payloads selectively into the designated spots in both nucleus and cytoplasm with active temporal control. Single cell endoscopes offer a unique instrumental platform for advancing our fundamental understanding of cellular functions, signal pathways and intracellular physiological processes.

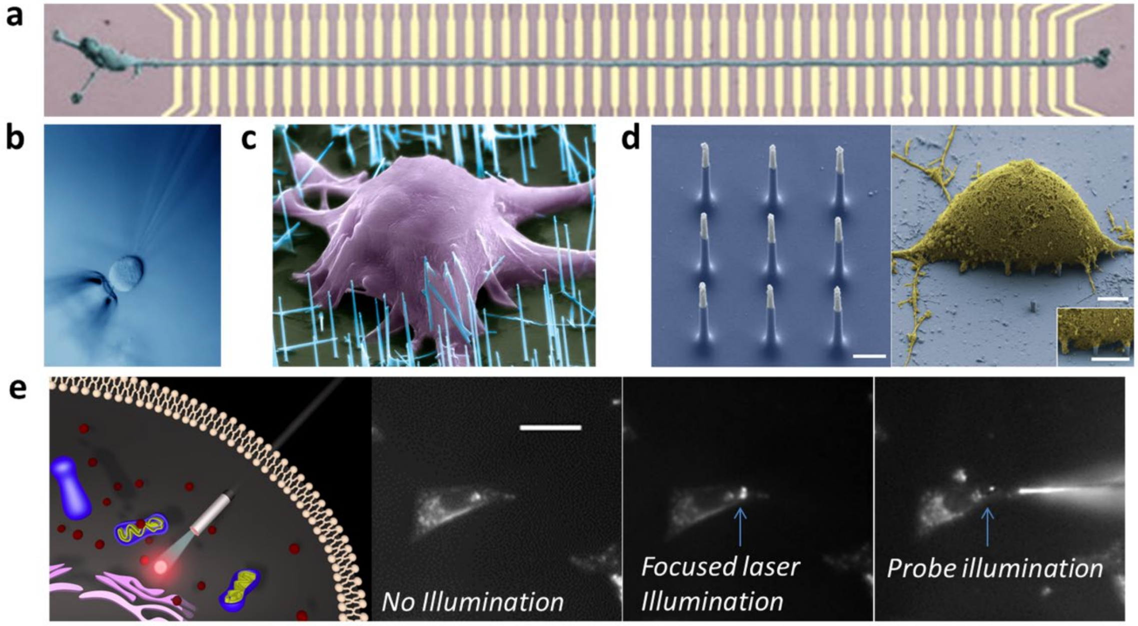

Figure 25. a) Optical image of a neuron (green) with an axon crossing an array of 50 nanowire FET devices (yellow) with 10 μm pitch. Signal propagation along the axon can be monitored in real time. Reproduced with permission.[335] Copyright 2006, American Academy for the Advancement of Science. b) Differential interference contrast microscopy images an HL-1 cell and 60° kinked nanowire probe showing that the cell internalized the nanoprobe. A pulled-glass micropipette (inner tip diameter ~ 5 μm) was used to manipulate the cell. Reproduced with permission.[349] Copyright 2010, Nature Publishing Group. c) Scanning electron micrograph (SEM) of a mouse embryonic stem cell growing on vertical silicon nanowires. Reproduced with permission.[332a] Copyright 2007, American Chemical Society. d) SEM image of a vertical nanowire electrode array (VNEA) pad constituent of nine Si nanowires (blue) with metal coated tips (white) (left; scale bar, 1 μm), and a rat cortical cell (yellow) on a VNEA pad (blue; scale bar, 2.5 μm), showing nanowires interfacing with the cellular membrane (inset; scale bar, 2.5 μm). Reproduced with permission.[333b] Copyright 2012, Nature Publishing Group. e) Schematics of nanowire endoscope for highly localized subcellular illumination (left) and microscope images showing the dark field (second left) of a living Hela Cell and QD fluorescence images comparing focused laser (second right) and endoscope (right) excitations of two adjacent quantum dot clusters in the cell. The endoscope can selectively excite one of the clusters,

showing the capability of high-resolution imaging. Reproduced with permission.[334b] Copyright 2012, Nature Publishing Group.

11. Conclusions and Future Directions

Each of these applications has been developed based on years of research into the synthesis, characterization, manipulation, and assembly of nanowires. The path from fundamental understanding to practical applications has led to numerous benefits for the entire materials research community. The interdisciplinary nature of the research presented here represents the future of scientific discovery, where the boundaries between chemistry, physics, biology, and engineering are no longer relevant.

The dramatic improvements in computational simulation and modeling, for example, have led to a new paradigm of materials discovery where rapid screening of potential materials, including new material phases, can be performed to allow for experimental researchers to focus on the most promising directions, and gain atomistic insight into novel results. In the past decade, tremendous advances have been made in the scale and speed of both quantum and classical simulations, which has been partially facilitated by an increase of three orders of magnitude in the power of high performance computing resources.[350] In particular, advances in predictive materials design and multiscale simulation tools will allow researchers to gain improved control over scientific and engineering challenges ranging from individual atomic defects to the assembly and integration of nanomaterials into larger systems and devices. This allows for the development of models with increased complexity, which can integrate multiple basic physical phenomena (optical, electronic, magnetic, thermal, etc.) that may occur at different physical length scales, in order to understand their interactions in nanostructured materials.

The spatial and temporal resolution of tools for nanoscale materials characterization has also increased significantly in the past decade (as well as their general availability to the research community). In particular, the combination of scanning probe, electron microscope, atom probe, ultrafast optical, and synchrotron techniques has enabled researchers to probe the physical, chemical, and electronic properties of nanowires with improved resolution. The insights from these measurements span a wide range of fields, including advances in fundamental physics, an improved understanding of the processes that occur during synthesis, dynamic processes that occur during device operation, and durability and failure mechanisms that dictate the lifetime and applicability of these materials. One trend that has been increasing in recent years is the application of these techniques for *in situ* characterization of materials during synthesis and device operation, as discussed throughout this Review. This trend is likely to continue to increase in coming years, as an improved understanding of the dynamics of these processes has allowed researchers to improve the design and fabrication of complex nanostructures and nanosystems. In the future, the combination of these techniques to probe multiple processes simultaneously will provide additional breakthroughs. For example, the combination of ultrafast laser spectroscopy with electron microscopy can enable a new level of characterization of dynamic processes which occur at the nanoscale.[350]

Another important emerging phenomenon in nanowire research is the need for systems-level engineering of devices, rather than simply focusing on the individual components (Figure 19a).[254] This is analogous to biological systems, where a full understanding of their behavior requires not only an understanding of the individual parts, but also the interfaces between them and how their interactions determine the performance of the entire system. In fact, these engineering approaches can often benefit from studying natural systems, as in the case of artificial photosynthesis. This will require an improvement in our ability to assemble nanostructures into specific orientations with complex 3-D geometries, as well as engineering of the interfaces which control the transfer of energy, force, charge, and/or mass across them.

Beyond the assembly of individual components into nanosystems with engineered interfaces, these architectures must be fabricated at large scale, with high throughput and low cost, while simultaneously maintaining control of material properties at the nanoscale. Therefore, the development of advanced nanomanufacturing processes such as large-scale self-assembly, advanced reactor design, and roll-to-roll processes for nanowire growth and assembly will be critical for commercial adaptation of these technologies. An emphasis should be placed on use of low-cost, environmentally-friendly, and earth-abundant materials, while minimizing the waste in utilization of more expensive elements in the processing. Avoiding energy-intensive processing such as high temperature or vacuum levels will also help to reduce production costs. Additionally, novel metrology tools with the necessary spatial and temporal resolution will be necessary to implement quality control in these high-throughput processes. This will facilitate the next era of nanotechnology, in which the technological, environmental, biomedical, and economic benefits of the aforementioned technologies to society are realized on a global scale.

Acknowledgement

This work was supported by the Director, Office of Science, Office of Basic Energy Sciences, Materials Sciences and Engineering Division, of the U.S. Department of Energy under Contract No. DE-AC02-05CH11231 (P-Chem).

References

[1] Y. Xia, P. Yang, Y. Sun, Y. Wu, B. Mayers, B. Gates, Y. Yin, F. Kim, H. Yan, *Adv. Mater.* **2003**, *15*, 353.

[2] a) B. J. Kim, J. Tersoff, C. Y. Wen, M. C. Reuter, E. A. Stach, F. M. Ross, *Phys. Rev. Lett.* **2009**, *103*, 155701; b) B. J. Kim, J. Tersoff, S. Kodambaka, M. C. Reuter, E. A. Stach, F. M. Ross, *Science* **2008**, *322*, 1070; c) C.-Y. Wen, M. C. Reuter, J. Bruley, J. Tersoff, S. Kodambaka, E. A. Stach, F. M. Ross, *Science* **2009**, *326*, 1247.

[3] O. G. Shpyrko, R. Streitel, V. S. K. Balagurusamy, A. Y. Grigoriev, M. Deutsch, B. M. Ocko, M. Meron, B. Lin, P. S. Pershan, *Science* **2006**, *313*, 77.

[4] a) C. Y. Wen, J. Tersoff, K. Hillerich, M. C. Reuter, J. H. Park, S. Kodambaka, E. A. Stach, F. M. Ross, *Phys. Rev. Lett.* **2011**, *107*, 025503; b) A. D. Gamalski, C. Ducati, S. Hofmann, *J. Phys. Chem. C.* **2011**, *115*, 4413; c) S. H. Oh, M. F. Chisholm, Y. Kauffmann, W. D. Kaplan, W. Luo, M. Rühle, C. Scheu, *Science* **2010**, *330*, 489.

[5] J. B. Hannon, S. Kodambaka, F. M. Ross, R. M. Tromp, *Nature* **2006**, *440*, 69.

[6] S. Kodambaka, J. B. Hannon, R. M. Tromp, F. M. Ross, *Nano Lett.* **2006**, *6*, 1292.

[7] J. E. Allen, E. R. Hemesath, D. E. Perea, J. L. Lensch-Falk, Z. Y. Li, F. Yin, M. H. Gass, P. Wang, A. L. Bleloch, R. E. Palmer, L. J. Lauhon, *Nature Nanotechnol.* **2008**, *3*, 168.

[8] O. Moutanabbir, D. Isheim, H. Blumtritt, S. Senz, E. Pippel, D. N. Seidman, *Nature* **2013**, *496*, 78.

[9] a) Y. Wu, Y. Cui, L. Huynh, C. J. Barrelet, D. C. Bell, C. M. Lieber, *Nano Lett.* **2004**, *4*, 433; b) V. Schmidt, S. Senz, U. Gösele, *Nano Lett.* **2005**, *5*, 931; c) A. Lugstein, M. Steinmair, Y. J. Hyun, G. Hauer, P. Pongratz, E. Bertagnolli, *Nano Lett.* **2008**, *8*, 2310; d) P. Madras, E. Dailey, J. Drucker, *Nano Lett.* **2009**, *9*, 3826.

[10] N. Shin, M. A. Filler, *Nano Lett.* **2012**, *12*, 2865.

[11] B. Tian, P. Xie, T. J. Kempa, D. C. Bell, C. M. Lieber, *Nature Nanotechnol.* **2009**, *4*, 824.

[12] T. Kuykendall, P. J. Pauzauskie, Y. Zhang, J. Goldberger, D. Sirbuly, J. Denlinger, P. Yang, *Nature Mater.* **2004**, *3*, 524.

[13] P. Caroff, K. A. Dick, J. Johansson, M. E. Messing, K. Deppert, L. Samuelson, *Nature Nanotechnol.* **2009**, *4*, 50.

[14] H. J. Joyce, Q. Gao, H. H. Tan, C. Jagadish, Y. Kim, X. Zhang, Y. Guo, J. Zou, *Nano Lett.* **2007**, *7*, 921.

[15] R. E. Algra, M. A. Verheijen, M. T. Borgstrom, L.-F. Feiner, G. Immink, W. J. P. van Enckevort, E. Vlieg, E. P. A. M. Bakkers, *Nature* **2008**, *456*, 369.

[16] H. J. Joyce, J. Wong-Leung, Q. Gao, H. H. Tan, C. Jagadish, *Nano Lett.* **2010**, *10*, 908.

[17] a) T. Mårtensson, M. Borgström, W. Seifert, B. J. Ohlsson, L. Samuelson, *Nanotechnology* **2003**, *14*, 1255; b) T. Mårtensson, P. Carlberg, M. Borgström, L. Montelius, W. Seifert, L. Samuelson, *Nano Lett.* **2004**, *4*, 699; c) B. Fuhrmann, H. S. Leipner, H.-R. Höche, L. Schubert, P. Werner, U. Gösele, *Nano Lett.* **2005**, *5*, 2524.

[18] H. J. Fan, W. Lee, R. Scholz, A. Dadgar, A. Krost, K. Nielsch, M. Zacharias, *Nanotechnology* **2005**, *16*, 913.

[19] S. A. Fortuna, J. Wen, I. S. Chun, X. Li, *Nano Lett.* **2008**, *8*, 4421.

[20] D. Tsivion, M. Schvartzman, R. Popovitz-Biro, P. von Huth, E. Joselevich, *Science* **2011**, *333*, 1003.

[21] Y. Shan, A. K. Kalkan, C.-Y. Peng, S. J. Fonash, *Nano Lett.* **2004**, *4*, 2085.

[22] M. T. Borgström, G. Immink, B. Ketelaars, R. Algra, E. P. A. M. Bakkers, *Nature Nanotechnol.* **2007**, *2*, 541.

[23] a) K. A. Dick, K. Deppert, M. W. Larsson, T. Martensson, W. Seifert, L. R. Wallenberg, L. Samuelson, *Nature Mater.* **2004**, *3*, 380; b) D. Wang, F. Qian, C. Yang, Z. Zhong, C. M. Lieber, *Nano Lett.* **2004**, *4*, 871.

[24] a) C. Yang, Z. Zhong, C. M. Lieber, *Science* **2005**, *310*, 1304; b) M. Hocevar, G. Immink, M. Verheijen, N. Akopian, V. Zwiller, L. Kouwenhoven, E. Bakkers, *Nature Commun.* **2012**, *3*, 1266.

[25] D. E. Perea, N. Li, R. M. Dickerson, A. Misra, S. T. Picraux, *Nano Lett.* **2011**, *11*, 3117.

[26] M. Heurlin, M. H. Magnusson, D. Lindgren, M. Ek, L. R. Wallenberg, K. Deppert, L. Samuelson, *Nature* **2012**, *492*, 90.

[27] S. Kodambaka, J. Tersoff, M. C. Reuter, F. M. Ross, *Science* **2007**, *316*, 729.

[28] a) A. I. Persson, M. W. Larsson, S. Stenstrom, B. J. Ohlsson, L. Samuelson, L. R. Wallenberg, *Nature Mater.* **2004**, *3*, 677; b) K. A. Dick, K. Deppert, T. Mårtensson, B. Mandl, L. Samuelson, W. Seifert, *Nano Lett.* **2005**, *5*, 761.

[29] a) S. Hofmann, R. Sharma, C. T. Wirth, F. Cervantes-Sodi, C. Ducati, T. Kasama, R. E. Dunin-Borkowski, J. Drucker, P. Bennett, J. Robertson, *Nature Mater.* **2008**, *7*, 372; b) C. Y. Wen, M. C. Reuter, J. Tersoff, E. A. Stach, F. M. Ross, *Nano Lett.* **2010**, *10*, 514.

[30] Y.-C. Chou, C.-Y. Wen, M. C. Reuter, D. Su, E. A. Stach, F. M. Ross, *ACS Nano* **2012**, *6*, 6407.

[31] V. T. Renard, M. Jublot, P. Gergaud, P. Cherns, D. Rouchon, A. Chabli, V. Jousseaume, *Nature Nanotechnol.* **2009**, *4*, 654.

[32] a) A. Dong, R. Tang, W. E. Buhro, *J. Am. Chem. Soc.* **2007**, *129*, 12254; b) A. Dong, F. Wang, T. L. Daulton, W. E. Buhro, *Nano Lett.* **2007**, *7*, 1308; c) L. Ouyang, K. N. Maher, C. L. Yu, J. McCarty, H. Park, *J. Am. Chem. Soc.* **2006**, *129*, 133.

[33] F. Wang, R. Tang, H. Yu, P. C. Gibbons, W. E. Buhro, *Chem. Mater.* **2008**, *20*, 3656.

[34] a) H. Yu, J. Li, R. A. Loomis, L.-W. Wang, W. E. Buhro, *Nature Mater.* **2003**, *2*, 517; b) H. Yu, J. Li, R. A. Loomis, P. C. Gibbons, Wang, W. E. Buhro, *J. Am. Chem. Soc.* **2003**, *125*, 16168; c) J. Sun, L.-W. Wang, W. E. Buhro, *J. Am. Chem. Soc.* **2008**, *130*, 7997; d) A. Dong, H. Yu, F. Wang, W. E. Buhro, *J. Am. Chem. Soc.* **2008**, *130*, 5954; e) F. Wang, H. Yu, S. Jeong, J. M. Pietryga, J. A. Hollingsworth, P. C. Gibbons, W. E. Buhro, *ACS Nano* **2008**, *2*, 1903.

[35] J. Sun, C. Liu, P. Yang, *J. Am. Chem. Soc.* **2011**, *133*, 19306.

[36] R. Laocharoensuk, K. Palaniappan, N. A. Smith, R. M. Dickerson, D. J. Werder, J. K. Baldwin, J. A. Hollingsworth, *Nature Nanotechnol.* **2013**, *8*, 660.

[37] a) H.-Y. Tuan, D. C. Lee, T. Hanrath, B. A. Korgel, *Nano Lett.* **2005**, *5*, 681; b) H.-Y. Tuan, D. C. Lee, T. Hanrath, B. A. Korgel, *Chem. Mater.* **2005**, *17*, 5705; c) H.-Y. Tuan, D. C. Lee, B. A. Korgel, *Angew. Chem. Int. Ed.* **2006**, *45*, 5184.

[38] B. D. Joyce, J. A. Baldrey, *Nature* **1962**, *195*, 485.

[39] K. Ikejiri, J. Noborisaka, S. Hara, J. Motohisa, T. Fukui, *J. Cryst. Growth* **2007**, *298*, 616.

[40] a) L. E. Greene, M. Law, J. Goldberger, F. Kim, J. C. Johnson, Y. Zhang, R. J. Saykally, P. Yang, *Angew. Chem. Int. Ed.* **2003**, *42*, 3031; b) L. E. Greene, M. Law, D. H. Tan, M. Montano, J. Goldberger, G. Somorjai, P. Yang, *Nano Lett.* **2005**, *5*, 1231.

[41] J. Joo, B. Y. Chow, M. Prakash, E. S. Boyden, J. M. Jacobson, *Nature Mater.* **2011**, *10*, 596.

[42] a) X. Feng, K. Shankar, O. K. Varghese, M. Paulose, T. J. Latempa, C. A. Grimes, *Nano Lett.* **2008**, *8*, 3781; b) B. Liu, E. S. Aydil, *J. Am. Chem. Soc.* **2009**, *131*, 3985.

[43] a) M. J. Bierman, Y. K. A. Lau, A. V. Kvit, A. L. Schmitt, S. Jin, *Science* **2008**, *320*, 1060; b) J. Zhu, H. Peng, A. F. Marshall, D. M. Barnett, W. D. Nix, Y. Cui, *Nature Nanotechnol.* **2008**, *3*, 477.

[44] a) F. Meng, S. Jin, *Nano Lett.* **2012**, *12*, 234; b) F. Meng, S. A. Morin, S. Jin, *J. Am. Chem. Soc.* **2011**, *133*, 8408.

[45] S. A. Morin, S. Jin, *Nano Lett.* **2010**, *10*, 3459.

[46] a) Z. Huo, C.-k. Tsung, W. Huang, X. Zhang, P. Yang, *Nano Lett.* **2008**, *8*, 2041; b) X. Lu, M. S. Yavuz, H.-Y. Tuan, B. A. Korgel, Y. Xia, *J. Am. Chem. Soc.* **2008**, *130*, 8900; c) C. Wang, Y. Hu, C. M. Lieber, S. Sun, *J. Am. Chem. Soc.* **2008**, *130*, 8902.

[47] M. G. Campbell, D. C. Powers, J. Raynaud, M. J. Graham, P. Xie, E. Lee, T. Ritter, *Nature Chem.* **2011**, *3*, 949.

[48] C. Mao, D. J. Solis, B. D. Reiss, S. T. Kottmann, R. Y. Sweeney, A. Hayhurst, G. Georgiou, B. Iverson, A. M. Belcher, *Science* **2004**, *303*, 213.

[49] D. H. Son, S. M. Hughes, Y. Yin, A. Paul Alivisatos, *Science* **2004**, *306*, 1009.

[50] U. Jeong, Y. Xia, Y. Yin, *Chem. Phys. Lett.* **2005**, *416*, 246.

[51] a) R. D. Robinson, B. Sadtler, D. O. Demchenko, C. K. Erdonmez, L.-W. Wang, A. P. Alivisatos, *Science* **2007**, *317*, 355; b) J. Tang, Z. Huo, S. Brittman, H. Gao, P. Yang, *Nature Nanotechnol.* **2011**, *6*, 568.

[52] D. H. Reneker, I. Chun, *Nanotechnology* **1996**, *7*, 216.

[53] a) G. Larsen, R. Velarde-Ortiz, K. Minchow, A. Barrero, I. G. Loscertales, *J. Am. Chem. Soc.* **2003**, *125*, 1154; b) D. Li, Y. Xia, *Nano Lett.* **2003**, *3*, 555; c) M. Bognitzki, M. Becker, M. Graeser, W. Massa, J. H. Wendorff, A. Schaper, D. Weber, A. Beyer, A. Gölzhäuser, A. Greiner, *Adv. Mater.* **2006**, *18*, 2384.

[54] G. Meng, Y. J. Jung, A. Cao, R. Vajtai, P. M. Ajayan, *Proc. Natl. Acad. Sci. U.S.A.* **2005**, *102*, 7074.

[55] Y. Wu, G. Cheng, K. Katsov, S. W. Sides, J. Wang, J. Tang, G. H. Fredrickson, M. Moskovits, G. D. Stucky, *Nature Mater.* **2004**, *3*, 816.

[56] Z. Tang, N. A. Kotov, M. Giersig, *Science* **2002**, *297*, 237.

[57] K.-S. Cho, D. V. Talapin, W. Gaschler, C. B. Murray, *J. Am. Chem. Soc.* **2005**, *127*, 7140.

[58] N. Pradhan, H. Xu, X. Peng, *Nano Lett.* **2006**, *6*, 720.

[59] C. O'Sullivan, R. D. Gunning, A. Sanyal, C. A. Barrett, H. Geaney, F. R. Laffir, S. Ahmed, K. M. Ryan, *J. Am. Chem. Soc.* **2009**, *131*, 12250.

[60] Y. Cui, X. Duan, J. Hu, C. M. Lieber, *J. Phys. Chem. B* **2000**, *104*, 5213.

[61] V. Schmidt, S. Senz, U. Gösele, *Appl. Phys. A* **2006**, *86*, 187.

[62] X. H. Sun, S. D. Wang, N. B. Wong, D. D. D. Ma, S. T. Lee, B. K. Teo, *Inorg. Chem.* **2003**, *42*, 2398.

[63] a) B. Hoex, J. Schmidt, P. Pohl, M. C. M. van de Sanden, W. M. M. Kessels, *J. Appl. Phys.* **2008**, *104*, 044903; b) G. Agostinelli, a. Delabie, P. Vitanov, Z. Alexieva, H. F. W. Dekkers, S. De Wolf, G. Beaucarne, *Sol. Energy Mater. Sol. Cells* **2006**, *90*, 3438.

[64] a) Y. Cui, Z. Zhong, D. Wang, W. U. Wang, C. M. Lieber, *Nano Lett.* **2003**, *3*, 149; b) H. Haick, P. T. Hurley, A. I. Hochbaum, P. Yang, N. S. Lewis, *J. Am. Chem. Soc.* **2006**, *128*, 8990.

[65] G. Hamaide, F. Allibert, H. Hovel, S. Cristoloveanu, *J. Appl. Phys.* **2007**, *101*, 114513.

[66] D. D. D. Ma, C. S. Lee, F. C. K. Au, S. Y. Tong, S. T. Lee, *Science* **2003**, *299*, 1874.

[67] R. Q. Zhang, Y. Lifshitz, D. D. D. Ma, Y. L. Zhao, T. Frauenheim, S. T. Lee, S. Y. Tong, *J. Chem. Phys.* **2005**, *123*, 144703.

[68] J. P. Gambino, E. G. Colgan, *Mater. Chem. Phys.* **1998**, *52*, 99.

[69] S. E. Mohney, Y. Wang, M. a. Cabassi, K. K. Lew, S. Dey, J. M. Redwing, T. S. Mayer, *Solid State Electron.* **2005**, *49*, 227.

[70] S. H. Hong, M. G. Kang, B.-S. Kim, D. S. Kim, J. H. Ahn, D. Whang, S. H. Sull, S. W. Hwang, *Solid State Electron.* **2011**, *56*, 130.

[71] Y.-C. Lin, K.-C. Lu, W.-W. Wu, J. Bai, L. J. Chen, K. N. Tu, Y. Huang, *Nano Lett.* **2008**, *8*, 913.

[72] N. S. Dellas, B. Z. Liu, S. M. Eichfeld, C. M. Eichfeld, T. S. Mayer, S. E. Mohney, *J. Appl. Phys.* **2009**, *105*, 094309.

[73] F. Léonard, a. A. Talin, *Nature Nantechnol.* **2011**, *6*, 773.

[74] G. Zheng, W. Lu, S. Jin, C. M. Lieber, *Adv. Mater.* **2004**, *16*, 1890.

[75] Y. Wu, J. Xiang, C. Yang, W. Lu, C. M. Lieber, *Nature* **2004**, *430*, 61.

[76] D. R. Khanal, J. Wu, *Nano Lett.* **2007**, *7*, 2778.

[77] M. T. Björk, H. Schmid, J. Knoch, H. Riel, W. Riess, *Nature Nantechnol.* **2009**, *4*, 103.

[78] S. Ramo, J. R. Whinnery, T. V. Duzer, *Fields and Waves in Communication Electronics*, Wiley, New York **1994**.

[79] O. Wunnicke, *Appl. Phys. Lett.* **2006**, *89*, 083102.

[80] D. Vashaee, A. Shakouri, J. Goldberger, T. Kuykendall, P. Pauzauskie, P. Yang, *J. Appl. Phys.* **2006**, *99*, 054310.

[81] W. Lu, J. Xiang, B. P. Timko, Y. Wu, C. M. Lieber, *Proc. Natl. Acad. Sci. U.S.A.* **2005**, *102*, 10046.

[82] J. Xiang, W. Lu, Y. Hu, Y. Wu, H. Yan, C. M. Lieber, *Nature* **2006**, *441*, 489.

[83] P. Nguyen, H. T. Ng, T. Yamada, M. K. Smith, J. Li, J. Han, M. Meyyappan, *Nano Lett.* **2004**, *4*, 651.

[84] a) T. Bryllert, L. E. Wernersson, L. E. Froberg, L. Samuelson, *IEEE Electron Device Lett.* **2006**, *27*, 323; b) H. T. Ng, J. Han, T. Yamada, P. Nguyen, Y. P. Chen, M. Meyyappan, *Nano Lett.* **2004**, *4*, 1247.

[85] N. Singh, A. Agarwal, L. K. Bera, T. Y. Liow, R. Yang, S. C. Rustagi, C. H. Tung, R. Kumar, G. Q. Lo, N. Balasubramanian, D. L. Kwong, *IEEE Electron Device Lett.* **2006**, *27*, 383.

[86] J. Goldberger, A. I. Hochbaum, R. Fan, P. Yang, *Nano Lett.* **2006**, *6*, 973.

[87] V. Schmidt, H. Riel, S. Senz, S. Karg, W. Riess, U. Gösele, *Small* **2006**, *2*, 85.

[88] E. C. Garnett, Y.-c. Tseng, D. R. Khanal, J. Wu, J. Bokor, P. Yang, *Nature Nantechnol.* **2009**, *4*, 21.

[89] M. Diarra, Y.-M. Niquet, C. Delerue, G. Allan, *Phys. Rev. B* **2007**, *75*, 045301.

[90] B. Weber, S. Mahapatra, H. Ryu, S. Lee, A. Fuhrer, T. C. G. Reusch, D. L. Thompson, W. C. T. Lee, G. Klimeck, L. C. L. Hollenberg, M. Y. Simmons, *Science* **2012**, *335*, 64.

[91] G. Imamura, T. Kawashima, M. Fujii, C. Nishimura, T. Saitoh, S. Hayashi, *Nano Lett.* **2008**, *8*, 2620.

[92] D. E. Perea, E. R. Hemesath, L. J. Lauhon, *Nature Nantechnol.* **2009**, *4*, 315.

[93] E. Koren, J. K. Hyun, U. Givan, E. R. Hemesath, L. J. Lauhon, Y. Rosenwaks, *Nano Lett.* **2011**, *11*, 183.

[94] A. B. Greytak, L. J. Lauhon, M. S. Gudiksen, C. M. Lieber, *Appl. Phys. Lett.* **2004**, *84*, 4176.

[95] T. Hanrath, B. a. Korgel, *J. Am. Chem. Soc.* **2004**, *126*, 15466.

[96] D. Wang, Q. Wang, A. Javey, R. Tu, H. Dai, H. Kim, P. C. McIntyre, T. Krishnamohan, K. C. Saraswat, *Appl. Phys. Lett.* **2003**, *83*, 2432.

[97] X. Duan, Y. Huang, Y. Cui, J. Wang, C. M. Lieber, *Nature* **2001**, *409*, 66.

[98] S. a. Dayeh, D. P. R. Aplin, X. Zhou, P. K. L. Yu, E. T. Yu, D. Wang, *Small* **2007**, *3*, 326.

[99] Q. Hang, F. Wang, P. D. Carpenter, D. Zemlyanov, D. Zakharov, E. a. Stach, W. E. Buhro, D. B. Janes, *Nano Lett.* **2008**, *8*, 49.

[100] A. C. Ford, J. C. Ho, Y. L. Chueh, Y. C. Tseng, Z. Fan, *Nano Lett.* **2009**, *9*, 360.

[101] T. Kuykendall, P. Pauzauskie, S. Lee, Y. Zhang, J. Goldberger, P. Yang, *Nano Lett.* **2003**, *3*, 1063.

[102] Y. Huang, X. Duan, Y. Cui, C. M. Lieber, *Nano Lett.* **2002**, *2*, 101.

[103] Z. Zhong, F. Qian, D. Wang, C. M. Lieber, *Nano Lett.* **2003**, *3*, 343.

[104] A. Janotti, C. G. Van de Walle, *Phys. Rev. B* **2007**, *76*, 1.

[105] a) J. Goldberger, D. J. Sirbuly, M. Law, P. Yang, *J. Phys. Chem. B* **2005**, *109*, 9; b) Y. Qin, X. Wang, Z. L. Wang, *Nature* **2008**, *451*, 809.

[106] P.-C. Chang, Z. Fan, C.-J. Chien, D. Stichtenoth, C. Ronning, J. G. Lu, *Appl. Phys. Lett.* **2006**, *89*, 133113.

[107] G. D. Yuan, W. J. Zhang, J. S. Jie, X. Fan, J. X. Tang, I. Shafiq, Z. Z. Ye, C. S. Lee, S. T. Lee, *Adv. Mater.* **2008**, *20*, 168.

[108] M. Ahmad, J. Zhao, J. Iqbal, W. Miao, L. Xie, R. Mo, J. Zhu, *J. Phys. D: Appl. Phys.* **2009**, *42*, 165406.

[109] D. D. Lin, H. Wu, W. Pan, *Adv. Mater.* **2007**, *19*, 3968.

[110] J. Lee, S. Cha, J. Kim, H. Nam, S. Lee, W. Ko, K. L. Wang, J. Park, J. Hong, *Adv. Mater.* **2011**, *23*, 4183.

[111] B. Xiang, P. Wang, X. Zhang, S. Dayeh, D. Aplin, C. Soci, D. Yu, D. Wang, *Nano Lett.* **2007**, *7*, 323.

[112] G. D. Yuan, W. J. Zhang, J. S. Jie, X. Fan, J. a. Zapien, Y. H. Leung, L. B. Luo, P. F. Wang, C. S. Lee, S. T. Lee, *Nano Lett.* **2008**, *8*, 2591.

[113] A. B. Yankovich, B. Puchala, F. Wang, J. H. Seo, D. Morgan, X. Wang, Z. Ma, A. V. Kvit, P. M. Voyles, *Nano Lett.* **2012**, *12*, 1311.

[114] a) C. H. Park, S. B. Zhang, S.-H. Wei, *Phys. Rev. B* **2002**, *66*, 1; b) S. Zhang, S. H. Wei, A. Zunger, *Phys. Rev. B* **2001**, *63*, 1.

[115] Q. Wan, E. Dattoli, W. Lu, *Small* **2008**, *4*, 451.

[116] E. N. Dattoli, Q. Wan, W. Guo, Y. Chen, X. Pan, W. Lu, *Nano Lett.* **2007**, *7*, 2463.

[117] C. Li, D. Zhang, S. Han, X. Liu, T. Tang, C. Zhou, *Adv. Mater.* **2003**, *15*, 143.

[118] Q. Wan, E. N. Dattoli, W. Y. Fung, W. Guo, Y. Chen, X. Pan, W. Lu, *Nano Lett.* **2006**, *6*, 2909.

[119] A. Kolmakov, Y. Zhang, G. Cheng, M. Moskovits, *Adv. Mater.* **2003**, *15*, 997.

[120] M. Law, H. Kind, B. Messer, F. Kim, P. Yang, *Angew. Chem. Int. Ed.* **2002**, *41*, 2405.

[121] Q. Kuang, C. Lao, Z. L. Wang, Z. Xie, L. Zheng, *J. Am. Chem. Soc.* **2007**, *129*, 6070.

[122] a. Kolmakov, D. O. Klenov, Y. Lilach, S. Stemmer, M. Moskovits, *Nano Lett.* **2005**, *5*, 667.

[123] Y. Zhang, A. Kolmakov, S. Chretien, H. Metiu, M. Moskovits, *Nano Lett.* **2004**, *4*, 403.

[124] a) C. Li, D. Zhang, X. Liu, S. Han, T. Tang, J. Han, C. Zhou, *Appl. Phys. Lett.* **2003**, *82*, 1613; b) I.-D. Kim, A. Rothschild, B. H. Lee, D. Y. Kim, S. M. Jo, H. L. Tuller, *Nano Lett.* **2006**, *6*, 2009.

[125] D. Zhang, Z. Liu, C. Li, T. Tang, X. Liu, S. Han, *Nano Lett.* **2004**, *4*, 1919.

[126] L. Francioso, a. Taurino, a. Forleo, P. Siciliano, *Sensor. Actuat. B-Chem.* **2008**, *130*, 70.

[127] Q. Wan, Q. H. Li, Y. J. Chen, T. H. Wang, X. L. He, J. P. Li, C. L. Lin, *Appl. Phys. Lett.* **2004**, *84*, 3654.

[128] a) Q. H. Li, Y. X. Liang, Q. Wan, T. H. Wang, *Appl. Phys. Lett.* **2004**, *85*, 6389; b) Z. Fan, D. Wang, P.-C. Chang, W.-Y. Tseng, J. G. Lu, *Appl. Phys. Lett.* **2004**, *85*, 5923.

[129] O. Lupan, V. V. Ursaki, G. Chai, L. Chow, G. a. Emelchenko, I. M. Tiginyanu, a. N. Gruzintsev, a. N. Redkin, *Sensor. Actuat. B-Chem.* **2010**, *144*, 56.

[130] X. P. a. Gao, G. Zheng, C. M. Lieber, *Nano Lett.* **2010**, *10*, 547.

[131] Z. Fan, J. G. Lu, *Appl. Phys. Lett.* **2005**, *86*, 123510.

[132] M. W. Shao, Y. Y. Shan, N. B. Wong, S. T. Lee, *Adv. Funct. Mater.* **2005**, *15*, 1478.

[133] Y. Cui, Q. Wei, H. Park, C. M. Lieber, *Science* **2001**, *293*.

[134] J.-i. Hahm, C. M. Lieber, *Nano Lett.* **2004**, *4*, 51.

[135] F. Patolsky, G. Zheng, O. Hayden, M. Lakadamyali, X. Zhuang, C. M. Lieber, *Proc. Natl. Acad. Sci. U.S.A.* **2004**, *101*, 14017.

[136] G. Zheng, F. Patolsky, Y. Cui, W. U. Wang, C. M. Lieber, *Nat. Biotechnol.* **2005**, *23*, 1294.

[137] A. Kim, C. S. Ah, H. Y. Yu, J.-H. Yang, I.-B. Baek, C.-G. Ahn, C. W. Park, M. S. Jun, S. Lee, *Appl. Phys. Lett.* **2007**, *91*, 103901.

[138] F. Patolsky, G. Zheng, C. M. Lieber, *Nat. Protoc.* **2006**, *1*, 1711.

[139] E. Stern, J. F. Klemic, D. a. Routenberg, P. N. Wyrembak, D. B. Turner-Evans, A. D. Hamilton, D. a. LaVan, T. M. Fahmy, M. a. Reed, *Nature* **2007**, *445*, 519.

[140] G.-J. Zhang, G. Zhang, J. H. Chua, R.-E. Chee, E. H. Wong, A. Agarwal, K. D. Buddharaju, N. Singh, Z. Gao, N. Balasubramanian, *Nano Lett.* **2008**, *8*, 1066.

[141] P. R. Nair, M. a. Alam, *Nano Lett.* **2008**, *8*, 1281.

[142] P. E. Sheehan, L. J. Whitman, *Nano Lett.* **2005**, *5*, 803.

[143] P. R. Nair, M. a. Alam, *Appl. Phys. Lett.* **2006**, *88*, 233120.

[144] E. Stern, R. Wagner, F. J. Sigworth, R. Breaker, T. M. Fahmy, M. a. Reed, *Nano Lett.* **2007**, *7*, 3405.

[145] R. Yan, D. Gargas, P. Yang, *Nature Photon.* **2009**, *3*, 569.

[146] M. Law, D. J. Sirbuly, J. C. Johnson, J. Goldberger, R. J. Saykally, P. Yang, *Science* **2004**, *305*, 1269.

[147] R. Yan, P. Pausauskie, J. Huang, P. Yang, *Proc. Natl. Acad. Sci. U.S.A.* **2009**, *106*, 21045.

[148] D. J. Sirbuly, M. Law, P. Pauzauskie, H. Yan, A. V. Maslov, K. Knutsen, C. Z. Ning, R. J. Saykally, P. Yang, *Proc. Natl. Acad. Sci. U.S.A.* **2005**, *102*, 7800.

[149] L. Cao, J. S. White, J.-S. Park, J. A. Schuller, B. M. Clemens, M. L. Brongersma, *Nature Mater.* **2009**, *8*, 643.

[150] L. Cao, P. Fan, M. L. Brongersma, *Nano Lett.* **2011**, *11*, 1463.

[151] J. Xu, X. Zhuang, P. Guo, W. Huang, W. Hu, Q. Zhang, Q. Wan, X. Zhu, Z. Yang, L. Tong, X. Duan, A. Pan, *Sci. Rep.* **2012**, *2*, 820.

[152] M. H. Huang, S. Mao, H. Feick, H. Yan, Y. Wu, H. Kind, E. Weber, R. Russo, P. Yang, *Science* **2001**, *292*, 1897.

[153] P. J. Pauzauskie, D. J. Sirbuly, P. Yang, *Phys. Rev. Lett.* **2006**, *96*, 143903.

[154] X. Duan, Y. Huang, R. Agarwal, C. M. Lieber, *Nature* **2003**, *421*, 241.

[155] H. Yan, R. He, J. Johnson, M. Law, R. J. Saykally, P. Yang, *J. Am. Chem. Soc.* **2003**, *125*, 4728.
[156] J. A. Zapien, Y. Jiang, X. M. Meng, W. Chen, F. C. K. Au, Y. Lifshitz, S. T. Lee, *Appl. Phys. Lett.* **2004**, *84*, 1189.
[157] J. C. Johnson, H.-J. Choi, K. P. Knutsen, R. D. Schaller, P. Yang, R. J. Saykally, *Nature Mater.* **2002**, *1*, 106.
[158] A. H. Chin, S. Vaddiraju, A. V. Maslov, C. Z. Ning, M. K. Sunkara, M. Meyyappan, *Appl. Phys. Lett.* **2006**, *88*.
[159] Y. Huang, X. Duan, C. M. Lieber, *Small* **2005**, *1*, 142.
[160] F. Qian, Y. Li, S. Gradecak, H. G. Park, Y. Dong, Y. Ding, Z. L. Wang, C. M. Lieber, *Nature Mater.* **2008**, *7*, 701.
[161] C. Hahn, Z. Zhang, A. Fu, C. H. Wu, Y. J. Hwang, D. J. Gargas, P. Yang, *ACS Nano* **2011**, *5*, 3970.
[162] D. O'Carroll, I. Lieberwirth, G. Redmond, *Nature Nanotechnol.* **2007**, *2*, 180.
[163] Y. Xiao, C. Meng, P. Wang, Y. Ye, H. Yu, S. Wang, F. Gu, L. Dai, L. Tong, *Nano Lett.* **2011**, *11*, 1122.
[164] H. Gao, A. Fu, S. C. Andrews, P. Yang, *Proc. Natl. Acad. Sci. USA* **2013**.
[165] R. F. Oulton, V. J. Sorger, D. A. Genov, D. F. P. Pile, X. Zhang, *Nature Photon.* **2008**, *2*, 496.
[166] R. F. Oulton, V. J. Sorger, T. Zentgraf, R. M. Ma, C. Gladden, L. Dai, G. Bartal, X. Zhang, *Nature* **2009**, *461*, 629.
[167] Y. J. Lu, J. Kim, H. Y. Chen, C. Wu, N. Dabidian, C. E. Sanders, C. Y. Wang, M. Y. Lu, B. H. Li, X. Qiu, W. H. Chang, L. J. Chen, G. Shvets, C. K. Shih, S. Gwo, *Science* **2012**, *337*, 450.
[168] P. Fan, U. K. Chettiar, L. Cao, F. Afshinmanesh, N. Engheta, M. L. Brongersma, *Nature Photon.* **2012**, *6*, 380.
[169] L. E. Bell, *Science* **2008**, *321*, 1457.
[170] G. J. Snyder, E. S. Toberer, *Nature Mater.* **2008**, *7*, 105.
[171] G. Chen, A. Shakouri, *ASME J. Heat Transfer* **2002**, *124*, 242.
[172] A. Majumdar, *Science* **2004**, *303*, 777.
[173] a) G. Joshi, H. Lee, Y. C. Lan, X. W. Wang, G. H. Zhu, D. Z. Wang, R. W. Gould, D. C. Cuff, M. Y. Tang, M. S. Dresselhaus, G. Chen, Z. F. Ren, *Nano Lett.* **2008**, *8*, 4670; b) K. F. Hsu, S. Loo, F. Guo, W. Chen, J. S. Dyck, C. Uher, T. Hogan, E. K. Polychroniadis, M. G. Kanatzidis, *Science* **2004**, *303*, 818; c) B. Poudel, Q. Hao, Y. Ma, Y. C. Lan, A. Minnich, B. Yu, X. A. Yan, D. Z. Wang, A. Muto, D. Vashaee, X. Y. Chen, J. M. Liu, M. S. Dresselhaus, G. Chen, Z. F. Ren, *Science* **2008**, *320*, 634; d) J. Androulakis, K. F. Hsu, R. Pcionek, H. Kong, C. Uher, J. J. DAngelo, A. Downey, T. Hogan, M. G. Kanatzidis, *Adv. Mater.* **2006**, *18*, 1170; e) R. Venkatasubramanian, E. Siivola, T. Colpitts, B. O'Quinn, *Nature* **2001**, *413*, 597; f) T. C. Harman, P. J. Taylor, M. P. Walsh, B. E. LaForge, *Science* **2002**, *297*, 2229.
[174] a) L. D. Hicks, M. S. Dresselhaus, *Phys. Rev. B* **1993**, *47*, 16631; b) L. Hicks, M. Dresselhaus, *Phys. Rev. B* **1993**, *47*, 12727; c) Y.-M. Lin, M. S. Dresselhaus, *Phys. Rev. B* **2003**, *68*, 075304.
[175] a) J. P. Heremans, V. Jovovic, E. S. Toberer, A. Saramat, K. Kurosaki, A. Charoenphakdee, S. Yamanaka, G. J. Snyder, *Science* **2008**, *321*, 554; b) Y. Z. Pei, X. Y. Shi, A. LaLonde, H. Wang, L.

D. Chen, G. J. Snyder, *Nature* **2011**, *473*, 66; c) Y. Z. Pei, H. Wang, G. J. Snyder, *Adv. Mater.* **2012**, *24*, 6125.
[176] L. Shi, D. Y. Li, C. H. Yu, W. Y. Jang, D. Y. Kim, Z. Yao, P. Kim, A. Majumdar, *ASME J. Heat Transfer* **2003**, *125*, 1209.
[177] a) A. Mavrokefalos, A. L. Moore, M. T. Pettes, L. Shi, W. Wang, X. G. Li, *J. Appl. Phys.* **2009**, *105*, 104318; b) J. H. Zhou, C. G. Jin, J. H. Seol, X. G. Li, L. Shi, *Appl. Phys. Lett.* **2005**, *87*, 113109; c) B. Hamdou, J. Kimling, A. Dorn, E. Pippel, R. Rostek, P. Woias, K. Nielsch, *Adv. Mater.* **2013**, *25*, 239; d) G. Tai, B. Zhou, W. L. Guo, *J. Phys. Chem. C* **2008**, *112*, 11314; e) G. Zhang, B. Kirk, L. A. Jauregui, H. Yang, X. Xu, Y. P. Chen, Y. Wu, *Nano Lett.* **2011**, *12*, 56; f) W. Wang, X. L. Lu, T. Zhang, G. Q. Zhang, W. J. Jiang, X. G. Li, *J. Am. Chem. Soc.* **2007**, *129*, 6702; g) W. Wang, G. Q. Zhang, X. G. Li, *J. Phys. Chem. C* **2008**, *112*, 15190; h) X. B. Zhao, X. H. Ji, Y. H. Zhang, T. J. Zhu, J. P. Tu, X. B. Zhang, *Appl. Phys. Lett.* **2005**, *86*, 062111; i) J. Ham, W. Shim, D. H. Kim, S. Lee, J. Roh, S. W. Sohn, K. H. Oh, P. W. Voorhees, W. Lee, *Nano Lett.* **2009**, *9*, 2867.
[178] a) J. W. Roh, S. Y. Jang, J. Kang, S. Lee, J. S. Noh, W. Kim, J. Park, W. Lee, *Appl. Phys. Lett.* **2010**, *96*; b) M. Fardy, A. I. Hochbaum, J. Goldberger, M. M. Zhang, P. D. Yang, *Adv. Mater.* **2007**, *19*, 3047; c) W. J. Liang, O. Rabin, A. I. Hochbaum, M. Fardy, M. J. Zhang, P. D. Yang, *Nano Res.* **2009**, *2*, 394; d) W. J. Liang, A. I. Hochbaum, M. Fardy, O. Rabin, M. J. Zhang, P. D. Yang, *Nano Lett.* **2009**, *9*, 1689.
[179] J. Moon, J. H. Kim, Z. C. Y. Chen, J. Xiang, R. K. Chen, *Nano Lett.* **2013**, *13*, 1196.
[180] a) N. Mingo, *Appl. Phys. Lett.* **2004**, *85*, 5986; b) N. Mingo, *Appl. Phys. Lett.* **2004**, *84*, 2652.
[181] F. Zhou, A. L. Moore, M. T. Pettes, Y. Lee, J. H. Seol, Q. L. Ye, L. Rabenberg, L. Shi, *J. Phys. D: Appl. Phys.* **2010**, *43*.
[182] S. C. Andrews, M. A. Fardy, M. C. Moore, S. Aloni, M. J. Zhang, V. Radmilovic, P. D. Yang, *Chem. Sci.* **2011**, *2*, 706.
[183] a) A. S. Henry, G. Chen, *J. Comput. Theor. Nanosci.* **2008**, *5*, 141; b) K. Esfarjani, G. Chen, H. T. Stokes, *Phys. Rev. B* **2011**, *84*.
[184] D. Y. Li, Y. Y. Wu, P. Kim, L. Shi, P. D. Yang, A. Majumdar, *Appl. Phys. Lett.* **2003**, *83*, 2934.
[185] A. I. Hochbaum, R. K. Chen, R. D. Delgado, W. J. Liang, E. C. Garnett, M. Najarian, A. Majumdar, P. D. Yang, *Nature* **2008**, *451*, 163.
[186] K. Q. Peng, Y. Wu, H. Fang, X. Y. Zhong, Y. Xu, J. Zhu, *Angew. Chem. Int. Ed.* **2005**, *44*, 2737.
[187] N. Mingo, *Phys. Rev. B* **2003**, *68*.
[188] a) A. L. Moore, S. K. Saha, R. S. Prasher, L. Shi, *Appl. Phys. Lett.* **2008**, *93*; b) P. Martin, Z. Aksamija, E. Pop, U. Ravaioli, *Phys. Rev. Lett.* **2009**, *102*; c) L. Liu, X. Chen, *J. Appl. Phys.* **2010**, *107*; d) A. Sellitto, F. X. Alvarez, D. Jou, *J. Appl. Phys.* **2010**, *107*; e) F. X. Alvarez, D. Jou, A. Sellitto, *ASME J. Heat Transfer* **2011**, *133*; f) J. Carrete, L. J. Gallego, L. M. Varela, N. Mingo, *Phys. Rev. B* **2011**, *84*; g) J. Sadhu, S. Sinha, *Phys. Rev. B* **2011**, *84*; h) Z. Wang, Z. H. Ni, R. J. Zhao, M. H. Chen, K. D. Bi, Y. F. Chen, *Physica B* **2011**, *406*, 2515.
[189] a) J. W. Lim, K. Hippalgaonkar, S. C. Andrews, A. Majumdar, P. D. Yang, *Nano Lett.* **2012**, *12*, 2475; b) K. Hippalgaonkar, B. L. Huang, R. K. Chen, K. Sawyer, P. Ercius, A. Majumdar, *Nano Lett.* **2010**, *10*, 4341.
[190] M. G. Ghossoub, K. V. Valavala, M. Seong, B. Azeredo, K. Hsu, J. S. Sadhu, P. K. Singh, S. Sinha, *Nano Lett.* **2013**, *13*, 1564.

[191] A. I. Boukai, Y. Bunimovich, J. Tahir-Kheli, J. K. Yu, W. A. Goddard, J. R. Heath, *Nature* **2008**, *451*, 168.
[192] a) D. Y. Li, Y. Wu, R. Fan, P. D. Yang, A. Majumdar, *Appl. Phys. Lett.* **2003**, *83*, 3186; b) H. Kim, I. Kim, H. J. Choi, W. Kim, *Appl. Phys. Lett.* **2010**, *96*; c) M. C. Wingert, Z. C. Y. Chen, E. Dechaumphai, J. Moon, J.-H. Kim, J. Xiang, R. Chen, *Nano Lett.* **2011**, *11*, 5507; d) E. K. Lee, L. Yin, Y. Lee, J. W. Lee, S. J. Lee, J. Lee, S. N. Cha, D. Whang, G. S. Hwang, K. Hippalgaonkar, A. Majumdar, C. Yu, B. L. Choi, J. M. Kim, K. Kim, *Nano Lett.* **2012**, *12*, 2918; e) T.-K. Hsiao, H.-K. Chang, S.-C. Liou, M.-W. Chu, S.-C. Lee, C.-W. Chang, *Nature Nanotechnol.* **2013**, *8*, 534.
[193] F. Zhou, J. Szczech, M. T. Pettes, A. L. Moore, S. Jin, L. Shi, *Nano Lett.* **2007**, *7*, 1649.
[194] a) T. J. Kempa, J. F. Cahoon, S.-K. Kim, R. W. Day, D. C. Bell, H.-G. Park, C. M. Lieber, *Proc. Natl. Acad. Sci. USA* **2012**, *109*, 1407; b) P. Krogstrup, H. I. Jorgensen, M. Heiss, O. Demichel, J. V. Holm, M. Aagesen, J. Nygard, A. Fontcuberta i Morral, *Nature Photon.* **2013**, *7*, 306.
[195] B. M. Kayes, H. A. Atwater, N. S. Lewis, *J. Appl. Phys.* **2005**, *97*, 114302.
[196] K. P. Musselman, A. Marin, L. Schmidt-Mende, J. L. MacManus-Driscoll, *Adv. Funct. Mater.* **2012**, *22*, 2202.
[197] A. Boukai, P. Haney, A. Katzenmeyer, G. M. Gallatin, A. A. Talin, P. Yang, *Chem. Phys. Lett.* **2011**, *501*, 153.
[198] H. P. Yoon, Y. A. Yuwen, C. E. Kendrick, G. D. Barber, N. J. Podraza, J. M. Redwing, T. E. Mallouk, C. R. Wronski, T. S. Mayer, *Appl. Phys. Lett.* **2010**, *96*, 213503.
[199] a) M. Law, L. E. Greene, J. C. Johnson, R. Saykally, P. Yang, *Nature Mater.* **2005**, *4*, 455; b) C. H. Peters, A. R. Guichard, A. C. Hryciw, M. L. Brongersma, M. D. McGehee, *J. Appl. Phys.* **2009**, *105*, 124509; c) B. Weintraub, Y. Wei, Z. L. Wang, *Angew. Chem. Int. Ed.* **2009**, *48*, 8981.
[200] A. L. Briseno, T. W. Holcombe, A. I. Boukai, E. C. Garnett, S. W. Shelton, J. J. Frechet, P. Yang, *Nano Lett.* **2010**, *10*, 334.
[201] Y. Zhan, X. Li, Y. Li, *IEEE J. Sel. Topics Quantum Electron.* **2013**, *PP*, 1.
[202] J. D. Christesen, X. Zhang, C. W. Pinion, T. A. Celano, C. J. Flynn, J. F. Cahoon, *Nano Lett.* **2012**, *12*, 6024.
[203] B. Tian, X. Zheng, T. J. Kempa, Y. Fang, N. Yu, G. Yu, J. Huang, C. M. Lieber, *Nature* **2007**, *449*, 885.
[204] M. A. Green, K. Emery, Y. Hishikawa, W. Warta, E. D. Dunlop, *Prog. Photovolt: Res. Appl.* **2012**, *20*, 606.
[205] C. Colombo, M. Heiβ, M. Grätzel, A. Fontcuberta i Morral, *Appl. Phys. Lett.* **2009**, *94*, 173108.
[206] J. V. Holm, H. I. Jørgensen, P. Krogstrup, J. Nygård, H. Liu, M. Aagesen, *Nature Commun.* **2013**, *4*, 1498.
[207] Y. Dong, B. Tian, T. J. Kempa, C. M. Lieber, *Nano Lett.* **2009**, *9*, 2183.
[208] a) J. Q. Xi, M. F. Schubert, J. K. Kim, E. F. Schubert, M. Chen, S.-Y. Lin, W. Liu, J. A. Smart, *Nature Photon.* **2007**, *1*, 176; b) Y. F. Huang, S. Chattopadhyay, Y. J. Jen, C. Y. Peng, T. A. Liu, Y. K. Hsu, C. L. Pan, H. C. Lo, C. H. Hsu, Y. H. Chang, C. S. Lee, K. H. Chen, L. C. Chen, *Nature Nantechnol.* **2007**, *2*, 770.
[209] J. Wallentin, N. Anttu, D. Asoli, M. Huffman, I. Aberg, M. H. Magnusson, G. Siefer, P. Fuss-Kailuweit, F. Dimroth, B. Witzigmann, H. Q. Xu, L. Samuelson, K. Deppert, M. T. Borgstrom, *Science* **2013**, *339*, 1057.
[210] Z. Yu, A. Raman, S. Fan, *Proc. Natl. Acad. Sci. USA* **2010**, *107*, 17491.

[211] a) J. Kupec, R. L. Stoop, B. Witzigmann, *Opt. Express* **2010**, *18*, 27589; b) C. Lin, M. L. Povinelli, *Opt. Express* **2009**, *17*, 19371.
[212] a) M. D. Kelzenberg, S. W. Boettcher, J. A. Petykiewicz, D. B. Turner-Evans, M. C. Putnam, E. L. Warren, J. M. Spurgeon, R. M. Briggs, N. S. Lewis, H. A. Atwater, *Nature Mater.* **2010**, *9*, 239; b) E. Garnett, P. Yang, *Nano Lett.* **2010**, *10*, 1082; c) Y. Lu, A. Lal, *Nano Lett.* **2010**, *10*, 4651.
[213] A. W. Snyder, J. D. Love, *Optical Waveguide Theory*, Chapman and Hall, New York **1983**.
[214] K. Seo, M. Wober, P. Steinvurzel, E. Schonbrun, Y. Dan, T. Ellenbogen, K. B. Crozier, *Nano Lett.* **2011**, *11*, 1851.
[215] a) G. Brönstrup, N. Jahr, C. Leiterer, A. Csáki, W. Fritzsche, S. Christiansen, *ACS Nano* **2010**, *4*, 7113; b) L. Cao, P. Fan, A. P. Vasudev, J. S. White, Z. Yu, W. Cai, J. A. Schuller, S. Fan, M. L. Brongersma, *Nano Lett.* **2010**, *10*, 439.
[216] Z. Fan, H. Razavi, J.-w. Do, A. Moriwaki, O. Ergen, Y.-L. Chueh, P. W. Leu, J. C. Ho, T. Takahashi, L. A. Reichertz, S. Neale, K. Yu, M. Wu, J. W. Ager, A. Javey, *Nature Mater.* **2009**, *8*, 648.
[217] a) N. S. Lewis, D. G. Nocera, *Proc. Natl. Acad. Sci. USA* **2006**, *103*, 15729; b) Y. Tachibana, L. Vayssieres, J. R. Durrant, *Nature Photon.* **2012**, *6*, 511.
[218] R. E. Blankenship, D. M. Tiede, J. Barber, G. W. Brudvig, G. Fleming, M. Ghirardi, M. R. Gunner, W. Junge, D. M. Kramer, A. Melis, T. A. Moore, C. C. Moser, D. G. Nocera, A. J. Nozik, D. R. Ort, W. W. Parson, R. C. Prince, R. T. Sayre, *Science* **2011**, *332*, 805.
[219] a) C. Liu, N. P. Dasgupta, P. Yang, *Chem. Mater.* **2013**, *DOI: 10.1021/cm4023198*; b) S. Xu, Y. Qin, C. Xu, Y. G. Wei, R. S. Yang, Z. L. Wang, *Nature Nantechnol.* **2010**, *5*, 366.
[220] M. Gratzel, *Nature* **2001**, *414*, 338.
[221] J. Turner, *Nature Mater.* **2008**, *7*, 770.
[222] M. G. Walter, E. L. Warren, J. R. McKone, S. W. Boettcher, Q. Mi, E. A. Santori, N. S. Lewis, *Chem. Rev.* **2010**, *110*, 6446.
[223] a) S. Y. Reece, J. A. Hamel, K. Sung, T. D. Jarvi, A. J. Esswein, J. J. H. Pijpers, D. G. Nocera, *Science* **2011**, *334*, 645; b) D. G. Nocera, *Acc. Chem. Res.* **2012**, *45*, 767.
[224] F. Le Formal, N. Tetreault, M. Cornuz, T. Moehl, M. Gratzel, K. Sivula, *Chem. Sci.* **2011**, *2*, 737.
[225] A. J. Bard, A. B. Bocarsly, F. R. F. Fan, E. G. Walton, M. S. Wrighton, *J. Am. Chem. Soc.* **1980**, *102*, 3671.
[226] a) J. R. Bolton, S. J. Strickler, J. S. Connolly, *Nature* **1985**, *316*, 495; b) S. Hu, C. Xiang, S. Haussener, A. D. Berger, N. S. Lewis, *Energy Environ. Sci.* **2013**, *6*, 2984.
[227] a) A. J. Nozik, *Appl. Phys. Lett.* **1976**, *29*, 150; b) H. B. Gray, *Nature Chem.* **2009**, *1*, 7; c) A. Kudo, *MRS Bull.* **2011**, *36*, 32.
[228] I. S. Cho, Z. Chen, A. J. Forman, D. R. Kim, P. M. Rao, T. F. Jaramillo, X. Zheng, *Nano Lett.* **2011**, *11*, 4978.
[229] N. P. Dasgupta, C. Liu, S. Andrews, F. B. Prinz, P. Yang, *J. Am. Chem. Soc.* **2013**, *135*, 12932.
[230] a) J. R. McKone, E. L. Warren, M. J. Bierman, S. W. Boettcher, B. S. Brunschwig, N. S. Lewis, H. B. Gray, *Energy Environ. Sci.* **2011**, *4*, 3573; b) E. L. Warren, J. R. McKone, H. A. Atwater, H. B. Gray, N. S. Lewis, *Energy Environ. Sci.* **2012**.
[231] J. M. Foley, M. J. Price, J. I. Feldblyum, S. Maldonado, *Energy Environ. Sci.* **2012**, *5*, 5203.

[232] S. Hu, C.-Y. Chi, K. T. Fountaine, M. Yao, H. A. Atwater, P. D. Dapkus, N. S. Lewis, C. Zhou, *Energy Environ. Sci.* **2013**, *6*, 1879.
[233] G. Liu, L. Wang, H. G. Yang, H.-M. Cheng, G. Q. Lu, *J. Mater. Chem.* **2010**, *20*, 831.
[234] a) I. S. Cho, C. H. Lee, Y. Feng, M. Logar, P. M. Rao, L. Cai, D. R. Kim, R. Sinclair, X. Zheng, *Nature Commun.* **2013**, *4*, 1723; b) Y. J. Hwang, C. Hahn, B. Liu, P. Yang, *ACS Nano* **2012**, *6*, 5060; c) M. Xu, P. Da, H. Wu, D. Zhao, G. Zheng, *Nano Lett.* **2012**, *12*, 1503; d) G. Wang, H. Wang, Y. Ling, Y. Tang, X. Yang, R. C. Fitzmorris, C. Wang, J. Z. Zhang, Y. Li, *Nano Lett.* **2011**, *11*, 3026; e) S. Hoang, S. P. Berglund, N. T. Hahn, A. J. Bard, C. B. Mullins, *J. Am. Chem. Soc.* **2012**, *134*, 3659.
[235] a) Y. Ling, G. Wang, D. A. Wheeler, J. Z. Zhang, Y. Li, *Nano Lett.* **2011**, *11*, 2119; b) L. Li, Y. Yu, F. Meng, Y. Tan, R. J. Hamers, S. Jin, *Nano Lett.* **2012**, *12*, 724.
[236] a) H. M. Chen, C. K. Chen, Y.-C. Chang, C.-W. Tsai, R.-S. Liu, S.-F. Hu, W.-S. Chang, K.-H. Chen, *Angew. Chem. Int. Ed.* **2010**, *49*, 5966; b) H. M. Chen, C. K. Chen, R.-S. Liu, C.-C. Wu, W.-S. Chang, K.-H. Chen, T.-S. Chan, J.-F. Lee, D. P. Tsai, *Adv. Energy Mater.* **2011**, *1*, 742.
[237] a) J. Su, X. Feng, J. D. Sloppy, L. Guo, C. A. Grimes, *Nano Lett.* **2010**, *11*, 203; b) P. M. Rao, I. S. Cho, X. Zheng, *Proc. Combust. Inst.* **2013**, *34*, 2187.
[238] C. Liu, J. Sun, J. Tang, P. Yang, *Nano Lett.* **2012**, *12*, 5407.
[239] a) D. Wang, A. Pierre, M. G. Kibria, K. Cui, X. Han, K. H. Bevan, H. Guo, S. Paradis, A.-R. Hakima, Z. Mi, *Nano Lett.* **2011**, *11*, 2353; b) B. AlOtaibi, M. Harati, S. Fan, S. Zhao, H. P. T. Nguyen, M. G. Kibria, Z. Mi, *Nanotechnology* **2013**, *24*, 175401.
[240] a) K.-Q. Peng, X. Wang, X.-L. Wu, S.-T. Lee, *Nano Lett.* **2009**, *9*, 3704; b) S. W. Boettcher, J. M. Spurgeon, M. C. Putnam, E. L. Warren, D. B. Turner-Evans, M. D. Kelzenberg, J. R. Maiolo, H. A. Atwater, N. S. Lewis, *Science* **2010**, *327*, 185; c) S. W. Boettcher, E. L. Warren, M. C. Putnam, E. A. Santori, D. Turner-Evans, M. D. Kelzenberg, M. G. Walter, J. R. McKone, B. S. Brunschwig, H. A. Atwater, N. S. Lewis, *J. Am. Chem. Soc.* **2011**, *133*, 1216; d) G. Yuan, H. Zhao, X. Liu, Z. S. Hasanali, Y. Zou, A. Levine, D. Wang, *Angew. Chem. Int. Ed.* **2009**, *48*, 9680; e) R. Liu, G. Yuan, C. L. Joe, T. E. Lightburn, K. L. Tan, D. Wang, *Angew. Chem. Int. Ed.* **2012**, *51*, 6537; f) R. Liu, C. Stephani, J. J. Han, K. L. Tan, D. Wang, *Angew. Chem. Int. Ed.* **2013**, *52*, 4225; g) Y. Hou, B. L. Abrams, P. C. K. Vesborg, M. E. Björketun, K. Herbst, L. Bech, A. M. Setti, C. D. Damsgaard, T. Pedersen, O. Hansen, J. Rossmeisl, S. Dahl, J. K. Nørskov, I. Chorkendorff, *Nature Mater.* **2011**, *10*, 434.
[241] a) Y. J. Hwang, A. Boukai, P. Yang, *Nano Lett.* **2008**, *9*, 410; b) M. T. Mayer, Y. Lin, G. Yuan, D. Wang, *Acc. Chem. Res.* **2013**.
[242] M. T. Mayer, C. Du, D. Wang, *J. Am. Chem. Soc.* **2012**, *134*, 12406.
[243] a) S. Y. Noh, K. Sun, C. Choi, M. Niu, M. Yang, K. Xu, S. Jin, D. Wang, *Nano Energy* **2013**, *2*, 351; b) J. Shi, Y. Hara, C. Sun, M. A. Anderson, X. Wang, *Nano Lett.* **2011**, *11*, 3413.
[244] R. H. Coridan, M. Shaner, C. Wiggenhorn, B. S. Brunschwig, N. S. Lewis, *J. Phys. Chem. C.* **2013**, *117*, 6949.
[245] Y. J. Hwang, C. H. Wu, C. Hahn, H. E. Jeong, P. Yang, *Nano Lett.* **2012**, *12*, 1678.
[246] Y. Lin, S. Zhou, X. Liu, S. Sheehan, D. Wang, *J. Am. Chem. Soc.* **2009**, *131*, 2772.
[247] R. Liu, Y. Lin, L.-Y. Chou, S. W. Sheehan, W. He, F. Zhang, H. J. M. Hou, D. Wang, *Angew. Chem. Int. Ed.* **2011**, *50*, 499.
[248] Y. Lin, S. Zhou, S. W. Sheehan, D. Wang, *J. Am. Chem. Soc.* **2011**, *133*, 2398.

[249] N. P. Dasgupta, S. Xu, H. J. Jung, A. Iancu, R. Fasching, R. Sinclair, F. B. Prinz, *Adv. Funct. Mater.* **2012**, *22*, 3650.

[250] J. Su, L. Guo, N. Bao, C. A. Grimes, *Nano Lett.* **2011**, *11*, 1928.

[251] K. Hagedorn, C. Forgacs, S. Collins, S. Maldonado, *J. Phys. Chem. C.* **2010**, *114*, 12010.

[252] a) G. Yuan, K. Aruda, S. Zhou, A. Levine, J. Xie, D. Wang, *Angew. Chem. Int. Ed.* **2011**, *50*, 2334; b) B. Klahr, S. Gimenez, F. Fabregat-Santiago, T. Hamann, J. Bisquert, *J. Am. Chem. Soc.* **2012**, *134*, 4294.

[253] C. Xiang, A. C. Meng, N. S. Lewis, *Proc. Natl. Acad. Sci. USA* **2012**, *109*, 15622.

[254] P. Yang, J.-M. Tarascon, *Nature Mater.* **2012**, *11*, 560.

[255] H. Dotan, K. Sivula, M. Gratzel, A. Rothschild, S. C. Warren, *Energy Environ. Sci.* **2011**, *4*, 958.

[256] C. Liu, Y. J. Hwang, H. E. Jeong, P. Yang, *Nano Lett.* **2011**, *11*, 3755.

[257] C. Liu, J. Tang, H. M. Chen, B. Liu, P. Yang, *Nano Lett.* **2013**, *13*, 2989.

[258] C. K. Chan, H. L. Peng, G. Liu, K. McIlwrath, X. F. Zhang, R. A. Huggins, Y. Cui, *Nature Nantechnol.* **2008**, *3*, 31.

[259] A. S. Arico, P. Bruce, B. Scrosati, J.-M. Tarascon, W. van Schalkwijk, *Nature Mater.* **2005**, *4*, 366.

[260] L.-F. Cui, R. Ruffo, C. K. Chan, H. Peng, Y. Cui, *Nano Lett.* **2008**, *9*, 491.

[261] Y. G. Li, B. Tan, Y. Y. Wu, *Nano Lett.* **2008**, *8*, 265.

[262] M. V. Reddy, G. V. Subba Rao, B. V. R. Chowdari, *Chem. Rev.* **2013**, *113*, 5364.

[263] A. R. Armstrong, G. Armstrong, J. Canales, R. García, P. G. Bruce, *Adv. Mater.* **2005**, *17*, 862.

[264] G. Armstrong, A. R. Armstrong, P. G. Bruce, P. Reale, B. Scrosati, *Adv. Mater.* **2006**, *18*, 2597.

[265] J. R. Li, Z. L. Tang, Z. T. Zhang, *Electrochem. Commun.* **2005**, *7*, 894.

[266] P. Poizot, S. Laruelle, S. Grugeon, L. Dupont, J. M. Tarascon, *Nature* **2000**, *407*, 496.

[267] P. L. Taberna, S. Mitra, P. Poizot, P. Simon, J. M. Tarascon, *Nature Mater.* **2006**, *5*, 567.

[268] K. T. Nam, D.-W. Kim, P. J. Yoo, C.-Y. Chiang, N. Meethong, P. T. Hammond, Y.-M. Chiang, A. M. Belcher, *Science* **2006**, *312*, 885.

[269] K. M. Shaju, F. Jiao, A. Debart, P. G. Bruce, *Phys. Chem. Chem. Phys.* **2007**, *9*, 1837.

[270] M.-S. Park, G.-X. Wang, Y.-M. Kang, D. Wexler, S.-X. Dou, H.-K. Liu, *Angew. Chem.* **2007**, *119*, 764.

[271] D.-W. Kim, I.-S. Hwang, S. J. Kwon, H.-Y. Kang, K.-S. Park, Y.-J. Choi, K.-J. Choi, J.-G. Park, *Nano Lett.* **2007**, *7*, 3041.

[272] H. Kim, J. Cho, *J. Mater. Chem.* **2008**, *18*, 771.

[273] J. P. Liu, Y. Y. Li, X. T. Huang, R. M. Ding, Y. Y. Hu, J. Jiang, L. Liao, *J. Mater. Chem.* **2009**, *19*, 1859.

[274] J. Y. Huang, L. Zhong, C. M. Wang, J. P. Sullivan, W. Xu, L. Q. Zhang, S. X. Mao, N. S. Hudak, X. H. Liu, A. Subramanian, H. Y. Fan, L. A. Qi, A. Kushima, J. Li, *Science* **2010**, *330*, 1515.

[275] X. H. Liu, L. Q. Zhang, L. Zhong, Y. Liu, H. Zheng, J. W. Wang, J. H. Cho, S. A. Dayeh, S. T. Picraux, J. P. Sullivan, S. X. Mao, Z. Z. Ye, J. Y. Huang, *Nano Lett.* **2011**, *11*, 2251.

[276] S. W. Lee, M. T. McDowell, J. W. Choi, Y. Cui, *Nano Lett.* **2011**, *11*, 3034.

[277] K. Q. Peng, J. S. Jie, W. J. Zhang, S. T. Lee, *Appl. Phys. Lett.* **2008**, *93*.

[278] X. H. Liu, H. Zheng, L. Zhong, S. Huan, K. Karki, L. Q. Zhang, Y. Liu, A. Kushima, W. T. Liang, J. W. Wang, J. H. Cho, E. Epstein, S. A. Dayeh, S. T. Picraux, T. Zhu, J. Li, J. P. Sullivan, J. Cumings, C. S. Wang, S. X. Mao, Z. Z. Ye, S. L. Zhang, J. Y. Huang, *Nano Lett.* **2011**, *11*, 3312.
[279] L. F. Cui, Y. Yang, C. M. Hsu, Y. Cui, *Nano Lett.* **2009**, *9*, 3370.
[280] Y. Yao, N. Liu, M. T. McDowell, M. Pasta, Y. Cui, *Energy Environ. Sci.* **2012**, *5*, 7927.
[281] Y. Yang, M. T. McDowell, A. Jackson, J. J. Cha, S. S. Hong, Y. Cui, *Nano Lett.* **2010**, *10*, 1486.
[282] C. K. Chan, X. F. Zhang, Y. Cui, *Nano Lett.* **2008**, *8*, 307.
[283] S. Y. Lim, C. S. Yoon, J. P. Cho, *Chem. Mater.* **2008**, *20*, 4560.
[284] Y. J. Lee, H. Yi, W.-J. Kim, K. Kang, D. S. Yun, M. S. Strano, G. Ceder, A. M. Belcher, *Science* **2009**, *324*, 1051.
[285] J.-Y. Luo, H.-M. Xiong, Y.-Y. Xia, *J. Phys. Chem. C.* **2008**, *112*, 12051.
[286] D. K. Kim, P. Muralidharan, H.-W. Lee, R. Ruffo, Y. Yang, C. K. Chan, H. Peng, R. A. Huggins, Y. Cui, *Nano Lett.* **2008**, *8*, 3948.
[287] E. Hosono, T. Kudo, I. Honma, H. Matsuda, H. S. Zhou, *Nano Lett.* **2009**, *9*, 1045.
[288] H. W. Lee, P. Muralidharan, R. Ruffo, C. M. Mari, Y. Cui, D. K. Kim, *Nano Lett.* **2010**, *10*, 3852.
[289] Y. Wang, G. Z. Cao, *Adv. Mater.* **2008**, *20*, 2251.
[290] K. Takahashi, S. J. Limmer, Y. Wang, G. Cao, *J. Phys. Chem. B* **2004**, *108*, 9795.
[291] C. K. Chan, H. Peng, R. D. Twesten, K. Jarausch, X. F. Zhang, Y. Cui, *Nano Lett.* **2007**, *7*, 490.
[292] L. Q. Mai, L. Xu, C. H. Han, X. Xu, Y. Z. Luo, S. Y. Zhao, Y. L. Zhao, *Nano Lett.* **2010**, *10*, 4750.
[293] a) E. W. Wong, P. E. Sheehan, C. M. Lieber, *Science* **1997**, *277*, 1971; b) M. Tabib-Azar, M. Nassirou, R. Wang, S. Sharma, T. I. Kamins, M. S. Islam, R. S. Williams, *Appl. Phys. Lett.* **2005**, *87*; c) B. Wu, A. Heidelberg, J. J. Boland, *Nature Mater.* **2005**, *4*, 525; d) A. S. Paulo, J. Bokor, R. T. Howe, R. He, P. Yang, D. Gao, C. Carraro, R. Maboudian, *Appl. Phys. Lett.* **2005**, *87*, 053111; e) J. Song, X. Wang, E. Riedo, Z. L. Wang, *Nano Lett.* **2005**, *5*, 1954.
[294] Y. Zhu, F. Xu, Q. Q. Qin, W. Y. Fung, W. Lu, *Nano Lett.* **2009**, *9*, 3934.
[295] a) S. Cuenot, C. Fretigny, S. Demoustier-Champagne, B. Nysten, *Phys. Rev. B* **2004**, *69*; b) G. Stan, C. V. Ciobanu, P. M. Parthangal, R. F. Cook, *Nano Lett.* **2007**, *7*, 3691.
[296] Z. L. Wang, *Adv. Mater.* **2000**, *12*, 1295.
[297] a) C. Y. Nam, P. Jaroenapibal, D. Tham, D. E. Luzzi, S. Evoy, J. E. Fischer, *Nano Lett.* **2006**, *6*, 153; b) R. Agrawal, B. Peng, E. E. Gdoutos, H. D. Espinosa, *Nano Lett.* **2008**, *8*, 3668.
[298] a) R. Dingreville, J. M. Qu, M. Cherkaoui, *J. Mech. Phys. Solids* **2005**, *53*, 1827; b) H. S. Park, W. Cai, H. D. Espinosa, H. C. Huang, *MRS Bull.* **2009**, *34*, 178.
[299] J. He, C. M. Lilley, *Nano Lett.* **2008**, *8*, 1798.
[300] M. T. McDowell, A. M. Leach, K. Gall, *Modell. Simul. Mater. Sci. Eng.* **2008**, *16*.
[301] A. Heidelberg, L. T. Ngo, B. Wu, M. A. Phillips, S. Sharma, T. I. Kamins, J. E. Sader, J. J. Boland, *Nano Lett.* **2006**, *6*, 1101.
[302] S. Hoffmann, I. Utke, B. Moser, J. Michler, S. H. Christiansen, V. Schmidt, S. Senz, P. Werner, U. Gosele, C. Ballif, *Nano Lett.* **2006**, *6*, 622.
[303] R. Agrawal, B. Peng, H. D. Espinosa, *Nano Lett.* **2009**, *9*, 4177.

[304] C. L. Hsin, W. J. Mai, Y. D. Gu, Y. F. Gao, C. T. Huang, Y. Z. Liu, L. J. Chen, Z. L. Wang, *Adv. Mater.* **2008**, *20*, 3919.
[305] G. F. Wang, X. Q. Feng, *Appl. Phys. Lett.* **2009**, *94*.
[306] L. W. Ji, S. J. Young, T. H. Fang, C. H. Liu, *Appl. Phys. Lett.* **2007**, *90*.
[307] G. Feng, W. D. Nix, Y. Yoon, C. J. Lee, *J. Appl. Phys.* **2006**, *99*.
[308] S. J. A. Koh, H. P. Lee, C. Lu, Q. H. Cheng, *Phys. Rev. B* **2005**, *72*.
[309] A. M. Leach, M. McDowell, K. Gall, *Adv. Funct. Mater.* **2007**, *17*, 43.
[310] D. W. Carr, S. Evoy, L. Sekaric, H. G. Craighead, J. M. Parpia, *Appl. Phys. Lett.* **1999**, *75*, 920.
[311] a) A. Husain, J. Hone, H. W. C. Postma, X. M. H. Huang, T. Drake, M. Barbic, A. Scherer, M. L. Roukes, *Appl. Phys. Lett.* **2003**, *83*, 1240; b) X. L. Feng, R. He, P. Yang, M. L. Roukes, *Nano Lett.* **2007**, *7*, 1953.
[312] K. Yum, Z. Y. Wang, A. P. Suryavanshi, M. F. Yu, *J. Appl. Phys.* **2004**, *96*, 3933.
[313] R. R. He, X. L. Feng, M. L. Roukes, P. D. Yang, *Nano Lett.* **2008**, *8*, 1756.
[314] R. He, P. Yang, *Nature Nanotechnol.* **2006**, *1*, 42.
[315] E. Gil-Santos, D. Ramos, J. Martinez, M. Fernandez-Regulez, R. Garcia, A. San Paulo, M. Calleja, J. Tamayo, *Nature Nanotechnol.* **2010**, *5*, 641.
[316] M. W. Li, R. B. Bhiladvala, T. J. Morrow, J. A. Sioss, K. K. Lew, J. M. Redwing, C. D. Keating, T. S. Mayer, *Nature Nantechnol.* **2008**, *3*, 88.
[317] Z. L. Wang, J. H. Song, *Science* **2006**, *312*, 242.
[318] X. Wang, J. Song, J. Liu, Z. L. Wang, *Science* **2007**, *316*, 102.
[319] a) R. Yang, Y. Qin, L. Dai, Z. L. Wang, *Nature Nanotechnol.* **2009**, *4*, 34; b) G. Zhu, R. Yang, S. Wang, Z. L. Wang, *Nano Lett.* **2010**, *10*, 3151.
[320] Z. L. Wang, G. Zhu, Y. Yang, S. H. Wang, C. F. Pan, *Mater. Today* **2012**, *15*, 532.
[321] Y. Hu, Y. Zhang, C. Xu, L. Lin, R. L. Snyder, Z. L. Wang, *Nano Lett.* **2011**, *11*, 2572.
[322] G. Zhu, A. C. Wang, Y. Liu, Y. Zhou, Z. L. Wang, *Nano Lett.* **2012**, *12*, 3086.
[323] WangWang, J. Zhou, Song, J. Liu, N. Xu, Z. L. Wang, *Nano Lett.* **2006**, *6*, 2768.
[324] Y. Zhang, Y. Liu, Z. L. Wang, *Adv. Mater.* **2011**, *23*, 3004.
[325] J. Zhou, Y. Gu, P. Fei, W. Mai, Y. Gao, R. Yang, G. Bao, Z. L. Wang, *Nano Lett.* **2008**, *8*, 3035.
[326] Z. L. Wang, *MRS Bull.* **2012**, *37*, 814.
[327] W. Wu, X. Wen, Z. L. Wang, *Science* **2013**, *340*, 952.
[328] Y. F. Hu, Y. L. Chang, P. Fei, R. L. Snyder, Z. L. Wang, *ACS Nano* **2010**, *4*, 1234.
[329] Q. Yang, X. Guo, W. H. Wang, Y. Zhang, S. Xu, D. H. Lien, Z. L. Wang, *ACS Nano* **2010**, *4*, 6285.
[330] Q. Yang, W. H. Wang, S. Xu, Z. L. Wang, *Nano Lett.* **2011**, *11*, 4012.
[331] C. F. Pan, L. Dong, G. Zhu, S. M. Niu, R. M. Yu, Q. Yang, Y. Liu, Z. L. Wang, *Nature Photon.* **2013**, *7*, 752.
[332] a) W. Kim, J. K. Ng, M. E. Kunitake, B. R. Conklin, P. D. Yang, *J. Am. Chem. Soc.* **2007**, *129*, 7228; b) T. Berthing, S. Bonde, C. B. Sørensen, P. Utko, J. Nygård, K. L. Martinez, *Small* **2011**, *7*, 640.
[333] a) B. Z. Tian, T. Cohen-Karni, Q. Qing, X. J. Duan, P. Xie, C. M. Lieber, *Science* **2010**, *329*, 830; b) J. T. Robinson, M. Jorgolli, A. K. Shalek, M. H. Yoon, R. S. Gertner, H. Park, *Nature*

Nantechnol. **2012**, *7*, 180; c) C. Xie, Z. Lin, L. Hanson, Y. Cui, B. Cui, *Nature Nanotechnol.* **2012**, *7*, 185.

[334] a) A. K. Shalek, J. T. Robinson, E. S. Karp, J. S. Lee, D. R. Ahn, M. H. Yoon, A. Sutton, M. Jorgolli, R. S. Gertner, T. S. Gujral, G. MacBeath, E. G. Yang, H. Park, *Proc. Natl. Acad. Sci. U.S.A.* **2010**, *107*, 1870; b) R. X. Yan, J. H. Park, Y. Choi, C. J. Heo, S. M. Yang, L. P. Lee, P. D. Yang, *Nature Nantechnol.* **2012**, *7*, 191.

[335] F. Patolsky, B. P. Timko, G. H. Yu, Y. Fang, A. B. Greytak, G. F. Zheng, C. M. Lieber, *Science* **2006**, *313*, 1100.

[336] a) T. Cohen-Karni, B. P. Timko, L. E. Weiss, C. M. Lieber, *Proc. Natl. Acad. Sci. U.S.A.* **2009**, *106*, 7309; b) T. Cohen-Karni, D. Casanova, J. F. Cahoon, Q. Qing, D. C. Bell, C. M. Lieber, *Nano Lett.* **2012**, *12*, 2639.

[337] a) Z. Jiang, Q. Qing, P. Xie, R. X. Gao, C. M. Lieber, *Nano Lett.* **2012**, *12*, 1711; b) X. J. Duan, R. X. Gao, P. Xie, T. Cohen-Karni, Q. Qing, H. S. Choe, B. Z. Tian, X. C. Jiang, C. M. Lieber, *Nature Nantechnol.* **2012**, *7*, 174; c) R. X. Gao, S. Strehle, B. Z. Tian, T. Cohen-Karni, P. Xie, X. J. Duan, Q. Qing, C. M. Lieber, *Nano Lett.* **2012**, *12*, 3329.

[338] B. P. Timko, T. Cohen-Karni, G. H. Yu, Q. Qing, B. Z. Tian, C. M. Lieber, *Nano Lett.* **2009**, *9*, 914.

[339] Q. Qing, S. K. Pal, B. Z. Tian, X. J. Duan, B. P. Timko, T. Cohen-Karni, V. N. Murthy, C. M. Lieber, *Proc. Natl. Acad. Sci. U.S.A.* **2010**, *107*, 1882.

[340] B. Z. Tian, J. Liu, T. Dvir, L. H. Jin, J. H. Tsui, Q. Qing, Z. G. Suo, R. Langer, D. S. Kohane, C. M. Lieber, *Nature Mater.* **2012**, *11*, 986.

[341] a) W. Hällström, T. Mårtensson, C. Prinz, P. Gustavsson, L. Montelius, L. Samuelson, M. Kanje, *Nano Lett.* **2007**, *7*, 2960; b) K. Jiang, D. Fan, Y. Belabassi, G. Akkaraju, J.-L. Montchamp, J. L. Coffer, *ACS Appl. Mater. Interfaces* **2008**, *1*, 266; c) S. J. Qi, C. Q. Yi, S. L. Ji, C. C. Fong, M. S. Yang, *ACS Appl. Mater. Interfaces* **2009**, *1*, 30; d) T. Berthing, S. Bonde, K. R. Rostgaard, M. H. Madsen, C. B. Sorensen, J. Nygard, K. L. Martinez, *Nanotechnology* **2012**, *23*; e) W. Zhao, K. Zhang, W. Xie, L. Hanson, Z. Lin, Y. Cui, B. Cui, *Biophys. J.* **2013**, *104*, 675a; f) C. Xie, L. Hanson, W. Xie, Z. Lin, B. Cui, Y. Cui, *Nano Lett.* **2010**, *10*, 4020.

[342] A. K. Shalek, J. T. Gaublomme, L. L. Wang, N. Yosef, N. Chevrier, M. S. Andersen, J. T. Robinson, N. Pochet, D. Neuberg, R. S. Gertner, I. Amit, J. R. Brown, N. Hacohen, A. Regev, C. J. Wu, H. Park, *Nano Lett.* **2012**, *12*, 6498.

[343] N. Chevrier, P. Mertins, Maxim N. Artyomov, Alex K. Shalek, M. Iannacone, Mark F. Ciaccio, I. Gat-Viks, E. Tonti, Marciela M. DeGrace, Karl R. Clauser, M. Garber, Thomas M. Eisenhaure, N. Yosef, J. Robinson, A. Sutton, Mette S. Andersen, David E. Root, U. von Andrian, Richard B. Jones, H. Park, Steven A. Carr, A. Regev, I. Amit, N. Hacohen, *Cell* **2011**, *147*, 853.

[344] N. Yosef, A. K. Shalek, J. T. Gaublomme, H. Jin, Y. Lee, A. Awasthi, C. Wu, K. Karwacz, S. Xiao, M. Jorgolli, D. Gennert, R. Satija, A. Shakya, D. Y. Lu, J. J. Trombetta, M. R. Pillai, P. J. Ratcliffe, M. L. Coleman, M. Bix, D. Tantin, H. Park, V. K. Kuchroo, A. Regev, *Nature* **2013**, *496*, 461.

[345] L. Hanson, Z. C. Lin, C. Xie, Y. Cui, B. Cui, *Nano Lett.* **2012**, *12*, 5815.

[346] S. K. Lee, G. S. Kim, Y. Wu, D. J. Kim, Y. Lu, M. Kwak, L. Han, J. H. Hyung, J. K. Seol, C. Sander, A. Gonzalez, J. Li, R. Fan, *Nano Lett.* **2012**, *12*, 2697.

[347] G. S. Park, H. Kwon, D. W. Kwak, S. Y. Park, M. Kim, J. H. Lee, H. Han, S. Heo, X. S. Li, J. H. Lee, Y. H. Kim, J. G. Lee, W. Yang, H. Y. Cho, S. K. Kim, K. Kim, *Nano Lett.* **2012**, *12*, 1638.

[348] Y. R. Na, S. Y. Kim, J. T. Gaublomme, A. K. Shalek, M. Jorgolli, H. Park, E. G. Yang, *Nano Lett.* **2013**, *13*, 153.
[349] *Nature* **2010**, *466*, 904.
[350] M. C. Roco, C. A. Mirkin, M. C. Hersam, *Nanotechnology Research Directions for Societal Needs in 2020: Retrospective and Outlook*, Springer, **2011**.